PARTICLE CONFINEMENT AND DIFFUSION IN TORSATRONS

R.E. Potok, L.M. Lidsky, and P.A. Politzer

August 1980

MIT Plasma Fusion Center Report PFC/RR-80-15

PARTICLE ORBITS AND DIFFUSION IN TORSATRONS

by

Robert Edward Potok

B.S., Physics, Carnegie-Mellon University

1975

Submitted in Partial Fulfillment of

the Requirements for the

Degree of

Doctor of Science

at the

Massachusetts Institute of Technology

May 1980

Signature _____

Department of Nuclear Engineering
May 9, 1980

Certified by _____

Thesis Supervisor

Accepted by _____

Chairman, Committee on Graduate Students

Due to the poor quality of the original document, there is some spotting or background shading in this document.

Particle Orbits and Diffusion in Torsatrons

by

Robert Edward Potok

Submitted to the Department of Nuclear Engineering on May 9, 1980, in partial fulfillment of the requirements for the Degree of Doctor of Science in Nuclear Engineering.

Abstract

The orbit characteristics of thermal and high energy particles in torsatrons are investigated with the aid of a computer code utilizing guiding-center equations accurate to second order in μ. Multi-dimensional cubic spline interpolation is used to calculate $\underline{B}$, $\nabla\underline{B}$, and $\underline{E}$ in a highly efficient manner. Background plasma profiles of voltage, electron temperature, and density are mapped onto the flux profile within the separatrix, and these plasma properties are used to calculate drag, $\underline{E} \times \underline{B}$, and velocity diffusion forces.

An analysis of the vacuum orbits of 3.5 MeV α-particles in torsatron vacuum fields shows that the particles may be grouped into two general classes, well circulating particles and blocked particles. Particles with $V_{\parallel} \gtrsim V_{\perp}$ have sufficient parallel energy so that they are never reflected by the helical or toroidal modulations in the magnetic field. Their orbits are characterized by extremely periodic motion on well defined drift surfaces. Blocked particles, on the other hand, are reflected by the modulations in B, and they can make frequent transitions among quasi-circulating, tokamak-like banana, and helically trapped orbits. Because of their non-periodic motion, their orbits do not conserve the second adiabatic invariant J, and the randomness of the phase of the bounce motion within a ripple results in varying particle drift positions after successive poloidal orbits. These particle orbits are contained in three-dimensional drift "regions".

The alpha-particle containment properties for reactor size torsatrons of various aspect ratios are computed by analyzing single particle orbits. A coarse grid in a four-dimensional phase space (three spatial directions and a pitch angle direction) is created, and the confinement properties of a test α-particle distribution are mapped onto this grid. Then, each grid location is weighted with a source strength corresponding to the fusion reaction rate for the local values of n_{DT} and T_i, and the field α-particle distribution function and confinement properties are found. Results show an overall α-particle percentage power in torsatrons of 99% for $R_o/a = 12$, 90% for $R_o/a = 6$, and 65% for $R_o/a = 3$. From a plasma heating point of view, such containment for moderate aspect ratio devices (order of 90% - 99%) is quite acceptable.

The ion thermal conductivity (χ_i) in torsatron configurations is measured by analyzing the interaction of a test particle distribution with a background plasma. For each measurement, 360 test ions are launched on a given flux surface. These test ions have a pitch angle and energy distribution appropriate to an isotropic Maxwellian with temperature equal to that of the background ions, and are uniformly spaced poloidally. The test distribution interacts with the background distribution through pitch angle scattering, energy scattering, and energy drag. The kinetic energy distribution function $U_i(X,t) = \int d^3 V\, f_i(X,V,t)\, \frac{1}{2} m_i V^2$ is created, and χ_i is determined by:

$$\chi_i = \frac{1/t \int dX \, \frac{(X-X_o)^2}{2} \, U_i(X,t)}{\int dX \, U_i(X,t)}$$

Numerical calculations of χ_i show the presence of a plateau regime extending over two orders of magnitude in collision frequency. The value of the ion thermal conductivity is found to be approximately equal to the neoclassical plateau value for an equivalent torus without helical modulation. The theoretically predicted adverse $1/\nu_{ii}$ scaling of χ_i due to ripple trapping is not seen (ν_{ii} = ion-ion collision frequency). This discrepancy is attributed to the difference between the theoretical and observed motion of particles trapped in the local magnetic ripples.

Power losses due to bremsstrahlung, ions scattering into unconfined orbits, and ion diffusion are calculated, and compared with the power being deposited into the plasma by thermalizing α-particles. Results indicate that a moderate aspect ratio torsatron with B_{z_o} = 5 tesla, $\langle a_{plasma} \rangle$ = 2.1 meters, a_{coils} = 4 meters, can meet or exceed ignition criteria with $T_i \cong 10 - 20$ keV.

Thesis Supervisor: Lawrence M. Lidsky

Title: Professor of Nuclear Engineering

Acknowledgements

Foremost I would like to express my sincere gratitude to Professors Lawrence M. Lidsky and Peter A. Politzer for their helpful support, corrections, and evaluations throughout the course of this thesis project. The support of the faculty members of the Nuclear Engineering Department of the Massachusetts Institute of Technology is also gratefully acknowledged. In particular, Professors Jeff Freidberg and Kim Molvig provided useful insights and suggestions for this work. I also thank these faculty and Professors David Rose and Ronald Davidson for being on my thesis defense committee and reviewing my work.

I express appreciation to the MIT fusion group for their comments, encouragement, and friendship. In particular, I thank John Aspinall for the use of his SOLVE code for vertical field coil placement, and for many interesting discussions on torsatron designs.

I thank Dr. David Anderson of the Lawrence Livermore Laboratory for suggesting and explaining the use of multi-dimensional spline interpolation. I also thank Dr. Allen Boozer of Princeton Plasma Physics Laboratory for helpful discussions concerning diffusive transport scalings in torsatron geometries.

I sincerely thank my parents and family for their support and optimism. Also, the interest and patience of my wife, Penelope Johnson, were deeply appreciated.
I also thank Penny, and Cathy Lydon, for typing up this thesis.

Computer requirements and my research salary were funded by the Department of Energy.

Table of Contents

Chapter I. INTRODUCTION

The family of plasma confinement devices that includes stellarators, torsatrons, and heliotrons is of considerable interest for controlled fusion applications. These are toroidal devices in which closed, nested magnetic surfaces are generated in the vacuum magnetic field by a helical configuration of the external windings. In this work two vital physics areas fundamental to torsatron plasmas have been examined. Both are related to the energy balance that would be maintained in a steady-state torsatron power reactor. The analyses reported here were performed for a torsatron magnetic field configuration because of the torsatron's particular compatibility with the engineering and plasma physics constraints of fusion power reactors.

The energy balance of the torsatrons studied was based on the DT fusion reaction:

$$D + T \rightarrow (He^4 + 3.52\ MeV) + (n + 14.06\ MeV)\ .$$

This reaction was chosen because of its uniquely large fusion cross section at moderate plasma temperatures (~ 15 keV). For steady-state plasma conditions, an instantaneous balance exists between the energy lost by the plasma through all mechanisms and the energy delivered to the plasma from external sources and fusion reactions. In the DT fusion reaction, the neutron leaves the plasma unimpeded, and only the 3.5 MeV He^4 particle can act as an internal energy

source for the plasma. If these energetic α-particles fail to balance the plasma's energy losses, the plasma might still be driven into a steady state by an external power supply, but it would be difficult to convert thermonuclear heat into salable electric power economically if the large power losses from the plasma had to be balanced by reinjection. It is therefore of fundamental interest to measure the energy loss rates of the torsatron plasma, and to find to what extent these losses are balanced by energy deposited by the α-particles.

In this thesis, the power deposition profiles of α-particle distributions were measured through numerical simulation of particle orbits. Tracking an α-particle in a torsatron from its fusion birth to thermalization (typically ~ 5000 poloidal orbits in helical toroidal fields) requires an exceedingly fast and accurate particle-following routine. In this thesis, the tracking code utilized guiding-center equations accurate to second order in μ, the adiabatically conserved magnetic moment of the particle. An efficient method for finding $\underline{B}$, $\nabla \underline{B}$, and $\underline{E}$ within the torsatron was also required. The magnetic field was calculated from a set of specified external conductors. This method was used, instead of recourse to a model field, in order to ensure that no significant oversimplifying assumptions regarding field configuration were made. Field quantities were calculated on a three-dimensional mesh, and multi-dimensional cubic spline interpolation was used to calculate

$\underline{B}$, $\underline{\nabla B}$, and $\underline{E}$ at arbitrary points within the spline grids. This interpolation method was used because it represents $\underline{B}$, $\underline{\nabla B}$, and $\underline{E}$ as smooth and continuous functions (a requirement for accurate tracking). The tracking code could perform ~ 10^6 evaluations of $\underline{B}$ and $\underline{\nabla B}$ per CRAY CPU minute, over 100 times faster than codes that evaluate $\underline{B}$ and $\underline{\nabla B}$ directly from the set of external conductors.

Numerous α-particles were tracked in each of the torsatrons studied, and the orbit characteristics of particles at various pitch angles and spatial positions were found. An α-particle distribution and energy deposition profile were found by combining the data of a set of α-particle orbits which filled a coarse grid in a 4-D phase space (three spatial dimensions and a pitch angle direction). This led to an accurate calculation of the percentage confinement in the plasma of the α-particle energy.

The diffusive energy loss rates in a torsatron plasma were determined from measurements of the ion thermal conductivity (χ_i). For each measurement, a test particle distribution (with a pitch angle and energy distribution appropriate to an isotropic Maxwellian with temperature equal to that of the background ions) was launched on a given flux surface. χ_i was determined by measuring the rate of diffusive spreading of the test particle distribution. The energy loss rates due to diffusing ions and bremsstrahlung were calculated, and compared with the power deposited in the plasma by thermalizing α-particles.

The observed scaling of the diffusive power loss was also compared with that predicted by neoclassical transport theory. A fundamental feature of the torsatron (and the entire stellarator family) is the presence of a strong helical modulation, or ripple, of the field strength on the flux surfaces. Neoclassical transport theory has associated with this ripple large transport coefficients, due to the particles which are trapped in the helical magnetic wells. The $1/\nu_{ii}$ dependence of these theoretical coefficients (with ν_{ii} = ion-ion collision frequency) imposes serious constraints on the plasma regimes in which a torsatron can economically operate. Another goal of this thesis, therefore, was to check the validity of ripple transport theory in the torsatron magnetic geometry. This checking was done on two levels: 1) comparing the theoretical and observed scaling of the transport coefficients, and 2) comparing the theoretical and observed behaviors of particles trapped in rippled magnetic fields.

The main body of this thesis work is given in Chapters II, III, and IV. Chapter II describes the characteristics of single particle orbits within a torsatron; Chapter III describes the α-particle distributions and energy deposition profiles; and Chapter IV describes the ion thermal conductivity scalings. In each chapter, the models used in the analyses are first developed; then the details of the analyses themselves are given; and, finally, the results and conclusions are presented. Chapter V contains

an abbreviated summary of the major results, and the appendices provide information on the numerical and mathematical techniques used in this thesis. Of particular interest are the descriptive examples of multi-dimensional cubic spline interpolation given in Appendix C, which I present because of the lack of such documentation in the current literature.

CHAPTER II. CHARGED PARTICLE ORBITS -- GUIDING-CENTER FORMALISM AND ORBIT CHARACTERISTICS

This chapter describes single particle motion in static magnetic fields. It is divided into three parts; the first two contain the derivation of the guiding-center equations and describe how these equations (along with drag and velocity diffusion and electric forces) were included in the orbit tracking code TAPIR. The third part describes single particle confinement and conserved particle quantities for:

1) helically axisymmetric systems

2) torsatron systems.

A. Development of Guiding-Center Equations

When writing a computer code that will track a particle's orbit, a decision must be made whether to track the particle itself or its guiding-center. Advantages of particle tracking are that the phase of the particle orbit is available, and the equation of motion is generally easier to code, compared with guiding-center tracking. The dominant advantage of a guiding-center code is that it allows a longer time step to be used (compared to particle tracking), since the high frequency cyclotron motion of the particle is not followed. In this thesis, the phase information associated with the particle orbits was not needed, and the large amount of computation required dictated that a guiding-center tracker be used. In a preliminary study, a fourth-order Runge-Kutta particle tracker was written to

check the drift surface plots produced by the guiding-center code TAPIR. It was found that a step size of $\omega_o \Delta t < .05$ was needed in order to track a particle accurately through a single poloidal drift orbit, with ω_o = cyclotron frequency. The guiding-center code TAPIR used a step size of $\omega_o \Delta t \tilde{=} 3$ to 10, depending on the guiding-center's pitch angle, and tracked guiding-centers accurately through several thousand poloidal orbits.

Guiding-center equations used in TAPIR

Starting from the equation of motion, I derive a set of equations accurate to second order in μ for curl free regions in $\underline{B}$. These equations are shown to conserve energy to second order, and also to satisfy the drift kinetic equation:

$$\underline{V} \cdot \underline{\nabla} f = 0 \qquad \text{[II-A-1]}$$

Following this derivation, a description of the implementation of these guiding-center equations in TAPIR is included, along with the results of the verification tests on tracking accuracy. The nonrelativistic equation of motion is:

$$\frac{m}{e} \ddot{\underline{r}} = \dot{\underline{r}} \times \underline{B}(\underline{r}) \qquad \text{[II-A-2]}$$

As shown by Northrop,[1] $\frac{m}{e} \equiv \varepsilon$ can be considered as a smallness parameter, just as $\frac{m v_o}{e B_o L_B}$ (the ratio of the radius of gyration to L_B, the characteristic distance over which the magnetic field changes) is a smallness parameter in an adiabatic approximation of a dimensionless equation of motion.

Northrop shows that, in zero order, the guiding-center e.o.m. is:

$$\underline{V}_{\parallel}^2 = \frac{2}{m}(E - \langle\mu\rangle B) + o(\varepsilon) \qquad \text{[II-A-3]}$$

$$\underline{V}_{\perp} = \frac{1}{eB}\hat{b} \times \left[\langle\mu\rangle \underline{\nabla} B + mV_{\parallel}^2 \hat{b} \cdot \nabla \hat{b}\right] + o(\varepsilon^2) \qquad \text{[II-A-4]}$$

$$\frac{dV_{\parallel}}{dt} = \frac{-\langle\mu\rangle}{m} \hat{b} \cdot \underline{\nabla} B + o(\varepsilon) \qquad \text{[II-A-5]}$$

Notation

$V_{\parallel}$, $V_{\perp}$ = guiding-center velocities

$v_{\parallel}$, $v_{\perp}$ = particle velocities

$w_{\perp}$ = Larmor velocity of particle, that is

$$v_{\perp} = w_{\perp} + V_{\perp} \ .$$

Coordinate system used is a right-handed Cartesian system $(\hat{e}_1, \hat{e}_2, \hat{b})$.

By keeping first order terms in the guiding-center equation of motion, I will show that

$o(\varepsilon)$ term of $V_{\parallel}^2$ is zero when $\nabla \times B = 0$

$o(\varepsilon)$ term of $\frac{dV_{\parallel}}{dt}$ is zero when $\nabla \times B = 0$.

From p. 69 of Northrop,

$$\frac{2\mu}{m} = \frac{\underline{v}_{\perp}^2}{B_{GC}} - \epsilon \frac{\underline{v}_{\parallel}}{B_{GC}^2}\left[\underline{v}_{\perp} \cdot (\hat{b} \times \underline{v}_{\perp}) \cdot \underline{\nabla} \hat{b}\right]$$

$$+ \quad \frac{\epsilon \, 2 \, v_{\parallel}^{2}}{B_{Gc}^{3}} \left(\hat{b} \times \underline{v}_{\perp} \right) \cdot \underline{\nabla} B_{Gc} + O(\epsilon^{2})$$

[II-A-6]

I will now average μ over a cyclotron period.

$$\frac{2 \langle \mu \rangle}{m} = \frac{\langle v_{\perp}^{2} \rangle}{B_{Gc}} \qquad \text{term 1}$$

$$- \frac{\epsilon V_{\parallel}}{B_{Gc}^{2}} \langle \underline{v}_{\perp} \cdot \left(\hat{b} \times \underline{v}_{\perp} \right) \cdot \underline{\nabla} \hat{b} \rangle \qquad \text{term 2}$$

$$+ \frac{\epsilon \, 2 V_{\parallel}^{2}}{B_{Gc}^{3}} \langle \left(\hat{b} \times \underline{v}_{\perp} \right) \rangle \cdot \underline{\nabla} B \qquad \text{term 3}$$

$$+ \quad O(\epsilon^{2}) \qquad \text{[II-A-7]}$$

since

$$\langle B_{Gc} \rangle = B_{Gc} + O(\epsilon^{2}) \qquad \text{[II-A-8]}$$

$$\langle v_{\parallel} \rangle = V_{\parallel} + O(\epsilon^{2}) \qquad \text{[II-A-9]}$$

term 1

$$\underline{W}_{\perp} = \hat{e}_{1} W_{\perp} \sin(\Omega t) + \hat{e}_{2} W_{\perp} \cos(\Omega t) \qquad \text{[II-A-10]}$$

$$\langle v_{\perp}^{2} \rangle = \langle W_{\perp}^{2} \rangle + \cancel{\langle V_{\perp}^{2} \rangle}^{\,O(\epsilon^{2})} + O(\epsilon^{2}) \qquad \text{[II-A-11]}$$

term 2 $\langle \underline{N}_\perp \cdot (\hat{b} \times \underline{N}_\perp) \cdot \underline{\nabla} \hat{b} \rangle =$

$$\frac{1}{2} \left[\hat{e}_1 \cdot (\hat{b} \times \hat{e}_1) \cdot \underline{\nabla} \hat{b} + \hat{e}_2 \cdot (\hat{b} \times \hat{e}_2) \cdot \underline{\nabla} \hat{b} \right] + O(\epsilon^2)$$

[II-A-12]

Proof:

$$\langle \underline{N}_\perp \cdot (\hat{b} \times \underline{N}_\perp) \cdot \underline{\nabla} \hat{b} \rangle + O(\epsilon)$$

$$= \langle \underline{w}_\perp \cdot (\hat{b} \times \underline{w}_\perp) \cdot \underline{\nabla} \hat{b} \rangle$$, since $V_\perp$ is of order ϵ

[II-A-13]

but $(\hat{b} \times \underline{w}_\perp)$

$$= w_\perp \left[(\hat{b} \times \hat{e}_1) \sin(\Omega t) + (\hat{b} \times \hat{e}_2) \cos(\Omega t) \right]$$

$$= w_\perp \left[\hat{e}_2 \sin(\Omega t) - \hat{e}_1 \cos(\Omega t) \right]$$

[II-A-14]

$$\therefore \langle \underline{w}_\perp \cdot (\hat{b} \times \underline{w}_\perp) \cdot \underline{\nabla} \hat{b} \rangle$$

$$= \langle w_\perp^2 \left\{ \hat{e}_1 \sin(\Omega t) \cdot ((\hat{b} \times \hat{e}_1) \sin(\Omega t) \cdot \underline{\nabla} \hat{b}) + \hat{e}_2 \cos(\Omega t) \cdot ((\hat{b} \times \hat{e}_2) \cos(\Omega t) \cdot \underline{\nabla} \hat{b}) \right\} \rangle$$

[II-A-15]

Since $\langle \sin(\Omega t) \cos(\Omega t) \rangle = 0$ and

$\langle \sin^2(\Omega t) \rangle = \langle \cos^2(\Omega t) \rangle = .5$, I get:

$$\langle \underline{\nu}_\perp \cdot ((\hat{b} \times \underline{\nu}_\perp) \cdot \underline{\nabla} \hat{b}) \rangle$$

$$= \frac{1}{2}\left[\hat{e}_1 \cdot ((\hat{b} \times \hat{e}_1) \cdot \underline{\nabla} b) + \hat{e}_2 \cdot ((\hat{b} \times \hat{e}_2) \cdot \underline{\nabla} \hat{b})\right]$$

$$= \frac{1}{2}\left[\hat{e}_1 \cdot (\hat{e}_2 \cdot \underline{\nabla})\hat{b} - \hat{e}_2 \cdot (\hat{e}_1 \cdot \underline{\nabla})\hat{b}\right] \qquad \text{[II-A-16]}$$

Noting that:

1) $$\hat{e}_1 \cdot (\hat{e}_2 \cdot \underline{\nabla})\hat{b} = \hat{e}_1 \cdot \frac{\partial \hat{b}}{\partial \underline{e}_2} \qquad \text{[II-A-17]}$$

2) $$-\hat{e}_2 \cdot (\hat{e}_1 \cdot \underline{\nabla})\hat{b} = -\hat{e}_2 \cdot \frac{\partial \hat{b}}{\partial \underline{e}_1} \qquad \text{[II-A-18]}$$

and 3) $$(\underline{\nabla} \times \hat{b})_{\parallel} = \hat{e}_2 \cdot \frac{\partial \hat{b}}{\partial \underline{e}_1} - \hat{e}_1 \cdot \frac{\partial \hat{b}}{\partial \underline{e}_2} \qquad \text{[II-A-19]}$$

equation [II-A-16] can be expressed as:

$$\langle \underline{\nu}_\perp \cdot ((\hat{b} \times \underline{\nu}_\perp) \cdot \underline{\nabla} \hat{b}) \rangle = -\frac{1}{2}(\underline{\nabla} \times \hat{b})_{\parallel} \qquad \text{[II-A-20]}$$

Now, note that:

$$\underline{\nabla} \times \underline{B} = 0 = \underline{\nabla} \times (\hat{b} B)$$

$$= B(\underline{\nabla} \times \hat{b}) + (\underline{\nabla} B \times \hat{b}) \qquad \text{[II-A-21]}$$

$$\underline{\nabla} \times \hat{b} = -\frac{\underline{\nabla} B \times \hat{b}}{B} \qquad \text{[II-A-22]}$$

Thus, since ($\underline{\nabla} B \times \hat{b}$) is perpendicular to $\hat{b}$,

$$(\underline{\nabla} \times \hat{b})_{\parallel} = 0 = \hat{b} \cdot (\nabla \times \hat{b})$$

[II-A-23]

So, finally, it can be seen that

$$\text{term 2} = \text{zero} + o(\epsilon^2)$$

[II-A-24]

$$\text{term 3} = \epsilon \frac{2 V_{\parallel}^2}{B^3} < (\hat{b} \times \underline{v}_{\perp}) > \cdot \underline{\nabla} B$$

[II-A-25]

$$< \hat{b} \times \underline{v}_{\perp} > \tilde{=} < \hat{b} \times \underline{w}_{\perp} >$$

[II-A-26]

(Since term 3 is already of order ϵ, only the zeroth order part of $\underline{v}_{\perp}$ need be kept.)

$$< \hat{b} \times \underline{w}_{\perp} > = w_{\perp} < (\hat{b} \times \hat{e}_1) \sin(\Omega t) + (\hat{b} \times \hat{e}_2) \cos(\Omega t) > = 0$$

[II-A-27]

Using these results in equation II-A-7 , we get:

$$\frac{2 < \mu >}{m} = \frac{< w_{\perp}^2 >}{B_{GC}} + O(\epsilon^2)$$

[II-A-28]

Now, let us write the energy equation:

$$E = \frac{1}{2} m v_{\parallel}^2 + \frac{1}{2} m v_{\perp}^2$$

$$= \frac{1}{2} m V_{\parallel}^2 + \frac{1}{2} m < w_{\perp}^2 > + O(\epsilon^2)$$

$$= \frac{1}{2} m V_{\parallel}^2 + < \mu > B_{GC} + O(\epsilon^2)$$

[II-A-29]

Solve for V^2:

$$V_{\parallel}^{\,2} = \frac{2}{m}\left(E - \langle \mu \rangle B_{Gc} \right) + o(\epsilon^2) \qquad \text{[II-A-30]}$$

$$\frac{d V_{\parallel}^{\,2}}{dt} = \left(\underline{V} \cdot \underline{\nabla} \right) V_{\parallel}^{\,2}$$

$$= \left(V_{\parallel} \hat{b} + \underline{V}_{\perp} \right) \cdot \underline{\nabla} V_{\parallel}^{\,2} \qquad \text{[II-A-31]}$$

$$\underline{\nabla} V_{\parallel}^{\,2} = \underline{\nabla} \left[\frac{2}{m} \left(E - \langle \mu \rangle B_{Gc} \right) \right] + o(\epsilon^2)$$

$$= 2 V_{\parallel} \underline{\nabla} V_{\parallel} \qquad \text{[II-A-32]}$$

Therefore

$$\underline{\nabla} V_{\parallel} = \frac{1}{2 V_{\parallel}} \underline{\nabla} \left(\frac{2 \langle \mu \rangle B_{Gc}}{m} \right) + o(\epsilon^2) \qquad \text{[II-A-33]}$$

$$\frac{d V_{\parallel}}{dt} = \left(V_{\parallel} \hat{b} + \underline{V}_{\perp} \right) \cdot \underline{\nabla} V_{\parallel} \qquad \text{[II-A-34]}$$

I will now show that $\underline{V}_{\perp} \cdot \underline{\nabla} V_{\parallel}$ is of $o(\epsilon^2)$.

Rewriting equation II-A-4, and factoring out an ϵ term:

$$\underline{V}_{\perp} = \frac{\epsilon}{B} \hat{b} \times \left[\underbrace{\frac{\langle \mu \rangle}{m} \underline{\nabla} B}_{\text{term 1}} + \underbrace{V_{\parallel}^{\,2} \hat{b} \cdot \underline{\nabla} \hat{b}}_{\text{term 2}} \right] + o(\epsilon^2) \qquad \text{[II-A-35]}$$

Considering term 1:

$\hat{b} \times \underline{\nabla} B$ is $\perp$ to $\underline{\nabla} B$, while $\underline{\nabla} V_{\parallel}$ is $\parallel$ to $\underline{\nabla} B$, so $(\hat{b} \times \text{term 1}) \cdot \underline{\nabla} V_{\parallel} = 0$

Considering term 2:

$$\hat{b} \times (\hat{b} \cdot \underline{\nabla} \hat{b}) = \frac{1}{B} \left(\hat{b} \times \underline{\nabla} B + \cancel{(\underline{\nabla} \times \underline{B})_{\perp}}^{\,0} \right) \qquad \text{[II-A-36]}$$

since: 1) $\hat{b} \cdot \underline{\nabla} \hat{b} = -\hat{b} \times (\underline{\nabla} \times \hat{b})$

2) $\underline{\nabla} \times \underline{B} = B\, \underline{\nabla} \times \hat{b} - \hat{b} \times (\underline{\nabla} B)$

3) $\hat{b} \times ((\hat{b} \times \underline{\nabla} B) \times \hat{b}) = \hat{b} \times (\underline{\nabla} B)$

Thus $\hat{b}$ x term 2 is also perpendicular to $\underline{\nabla} B$, and so $(\hat{b} \text{ x term 2}) \cdot \underline{\nabla} V_{\parallel} = 0$ [II-A-37]

Using these results in equation II-A-35, I get:

$$\frac{d V_{\parallel}}{dt} = -\frac{\langle \mu \rangle}{m} \hat{b} \cdot \underline{\nabla} B_{GC} + O(\epsilon^2) \qquad \text{[II-A-38]}$$

As pointed out by Allen Boozer,[2] for the guiding-center equations to be physcial, the drift kinetic equation $\underline{V} \cdot \underline{\nabla} f = 0$ must conserve particles ($\underline{\nabla} \cdot \int \underline{V} f \, d^3 V = 0$), with

$$d^3 V = \sum_{\sigma} \frac{2\pi B}{m^2 |V_{\parallel}|} dE \, d\mu \qquad \text{[II-A-39]}$$

where $\sigma = V_{\parallel} / |V_{\parallel}| = \pm 1$.

For an arbitrary distribution f, particle conservation implies

$$\underline{\nabla} \cdot \left(\frac{B}{V_{\parallel}} \underline{V} \right) = 0 \qquad \text{[II-A-40]}$$

and thus

$$\underline{V}_{\parallel} = \frac{\sigma |V_{\parallel}|}{B} \left[\underline{B} + \left(\underline{\nabla} \times \left(\rho_{\parallel} \underline{B} \right) \right)_{\parallel} \right]$$

with

$$\rho_{\parallel} = m v_{\parallel} / e B \qquad \text{[II-A-41]}$$

For this to be consistent with the second order accurate derivation, $(\underline{\nabla} \times (\rho_{\parallel} \underline{B}))_{\parallel} = 0$. For curl free fields, this is indeed the case, since $\underline{\nabla} \times (\rho_{\parallel} \underline{B}) = \underline{\nabla} \rho_{\parallel} \times \underline{B}$, and $(\underline{\nabla} \rho_{\parallel} \times \underline{B}) \perp \underline{B}$.

The proof that second order accurate guiding-center equations also conserve energy to second order is equally straightforward:

$$\frac{d V_{\parallel}}{dt} = - \frac{\langle \mu \rangle}{m} \hat{b} \cdot \underline{\nabla} B + O(\epsilon^2)$$

$$= - \frac{\langle \mu \rangle}{m} \left[\frac{V_{\parallel} \hat{b} \cdot \underline{\nabla} B}{V_{\parallel}} + \frac{\underline{V}_{\perp} \cdot \underline{\nabla} B}{V_{\parallel}} \right] + O(\epsilon^2)$$

$$(\text{since } \underline{V}_{\perp} \cdot \underline{\nabla} B = 0)$$

$$= - \frac{\langle \mu \rangle}{m} \frac{\underline{V} \cdot \underline{\nabla} B}{V_{\parallel}} + O(\epsilon^2) \qquad \text{[II-A-42]}$$

$$\frac{m}{2} \frac{d V_{\parallel}^2}{dt} + O(\epsilon^2) = - \langle \mu \rangle \underline{V} \cdot \underline{\nabla} B = - \langle \mu \rangle \frac{dB}{dt} \qquad \text{[II-A-43]}$$

(since, for static fields, $\partial B / \partial t = 0$)

$$\frac{d}{dt}\left(\frac{1}{2} m V_{\parallel}^{2} + \langle \mu \rangle B \right) = o(\epsilon^{2}) = \frac{dE}{dt}$$

[II-A-44]

Q.E.D.

B. Code Implementation of the Guiding-Center Equations

The orbit integration program used basically the same predictor-corrector scheme that was used to track the vacuum field lines (see Appendix D). The magnetic field $\underline{B}(\underline{r})$ was again evaluated by multi-dimensional cubic spline interpolation. The use of cubic spline interpolation was strongly motivated by code requirements of speed and accuracy. In tracking an α-particle from its birth to thermalization, approximately 10^{6} evaluations of $\underline{B}(\underline{r})$ and $\nabla \underline{B}(\underline{r})$ are needed. It would be prohibitively expensive (in terms of CPU) to evaluate $\underline{B}$ this number of times from a specified set of external current segments. Also, approximating $\underline{B}(\underline{r})$ with a model field might entail making an oversimplifying assumption about the nature of $\underline{B}(\underline{r})$. Both of these problems are avoided if $\underline{B}(\underline{r})$ is first evaluated at a fixed number of grid locations from a set of current segments, and then evaluated during particle tracking by grid interpolation. A common problem associated with interpolation schemes based on Taylor expansions of the evaluated function is that the finite difference approximations

introduces a numerical divergence in the functions. It was found that this problem did not occur with cubic spline interpolation, and that orbits tracked with spline evaluation of $\underline{B}(\underline{r})$ matched orbits tracked with $\underline{B}(\underline{r})$ evaluated directly from the current segments.

A set of two-dimensional spline grids, equally spaced toroidally along a module, was created, and $\underline{B}(\underline{r})$ evaluated by two-dimensional spline interpolation. This approach was chosen, as opposed to the creation of one large three-dimensional grid, because two-dimensional spline interpolation is four times as fast numerically as three-dimensional interpolation, and the two-dimensional interpolation could be done in a simple Cartesian geometry. The two-dimensional interpolation scheme did require that $\underline{B}(\underline{r})$ be evaluated only at the ϕ values of the grid locations, and the tracking algorithm was developed accordingly.

The guiding-center following code is very similar to the field line following code (see Appendix D), the main differences being that now:

1) the velocity vector is the instantaneous guiding-center velocity, rather than a unit vector in the $\hat{b}$ direction;

2) plasma electric fields add an $\underline{E} \times \underline{B} / B^2$ velocity to the perpendicular guiding-center velocity;

3) the corrector step is iterated from 2 to 4 times, in order to obtain sufficient accuracy for extended tracking (alpha particles may make thousands of poloidal orbits while slowing down);

4) particle reflection is included in the tracking algorithm.

I present now a detailed description of the pushing algorithm , first without the possibility of particle reflection.

At time t = 0, the following particle quantities are known: μ, $V_{\parallel}(0)$, $\underline{r}(0)$. The magnetic and electric fields are calculated at $\underline{r}(0)$, and $\underline{V}_{\perp}(0)$ is calculated from the guiding-center equations. The guiding-center is launched along its initial velocity direction, keeping toroidal and radial velocity constant (see appendix D). The time Δt^{pred} for the guiding-center to intersect the next ϕ-plane is found, as is the intersection point $\underline{r}(\Delta t^{pred})$. The magnetic and electric fields are found at this point, and $V_{\parallel}^2$ (Δt^{pred}) is calculated from the energy conservation equation:

$$\frac{d}{dt}\left(\frac{m}{2} < v_{\perp}^2 > + \frac{m}{2} v_{\parallel}^2 + e\phi \right) = 0 \qquad \text{[II-B-1]}$$

It should be noted here that, in calculating the magnetic moment, the perpendicular velocity must be that observed in the frame of reference moving at the guiding-center velocity -- $(\underline{V}_{GC} - \underline{V}_{\underline{E}\times\underline{B}})$. In the presence of an electric field:[1]

$$< v_{\perp}^2 >_{laboratory} = \frac{2\mu B}{m} + V_{\underline{E}\times\underline{B}}^2 \qquad \text{[II-B-2]}$$

Thus:

$$V_{\parallel}^2(\Delta t^{pred}) = \frac{2}{m}\left[E_{total} - \mu B(\Delta t^{pred}) - e\phi(\Delta t^{pred}) \right] - V_{\underline{E}\times\underline{B}}^2(\Delta t^{pred}) \qquad \text{[II-B-3]}$$

with

$$E_{total} = \frac{m}{2} V_{\parallel}^2(o) + \mu B(o) + e\phi(o) + \frac{m}{2} V^2_{\underline{E}\times\underline{B}}(o) \qquad [II\text{-}B\text{-}4]$$

$$V_{\parallel}(o t^{pred}) = \sqrt{V_{\parallel}^2(o t^{pred})}\ \sigma(t=o) \qquad [II\text{-}B\text{-}5]$$

$$\text{with} \quad \sigma = V_{\parallel} / |V_{\parallel}| \qquad [II\text{-}B\text{-}6]$$

Knowing $V_{\parallel}(\Delta t^{pred})$, $\underline{V}_{\perp}(\Delta t^{pred})$ is calculated. The guiding-center velocity at Δt^{pred} is then averaged with the original guiding-center velocity at $t = 0$, and this new velocity vector is used to push the particle from $\underline{r}(t = 0)$ onto the next ϕ-plane. The new intersection point is the corrector point $\underline{r}(\Delta t^{corr})$. As before, energy conservation is used to find $V_{\parallel}(\Delta t^{corr})$. The simple predictor corrector push is now complete.

It was found that this simple predictor-corrector push was not accurate enough to track alpha particles through many poloidal orbits. Long tracks of particles in vacuum fields showed the effect of a numerical drift which tended to push the particle drift surface in toward the magnetic axis (see Figure II-B-1). This numerical drift was eliminated by iterating the corrector step of the pushing algorithm. This involved treating the corrector point as an updated value of the predictor point, and then repeating the process of finding the (new) corrector

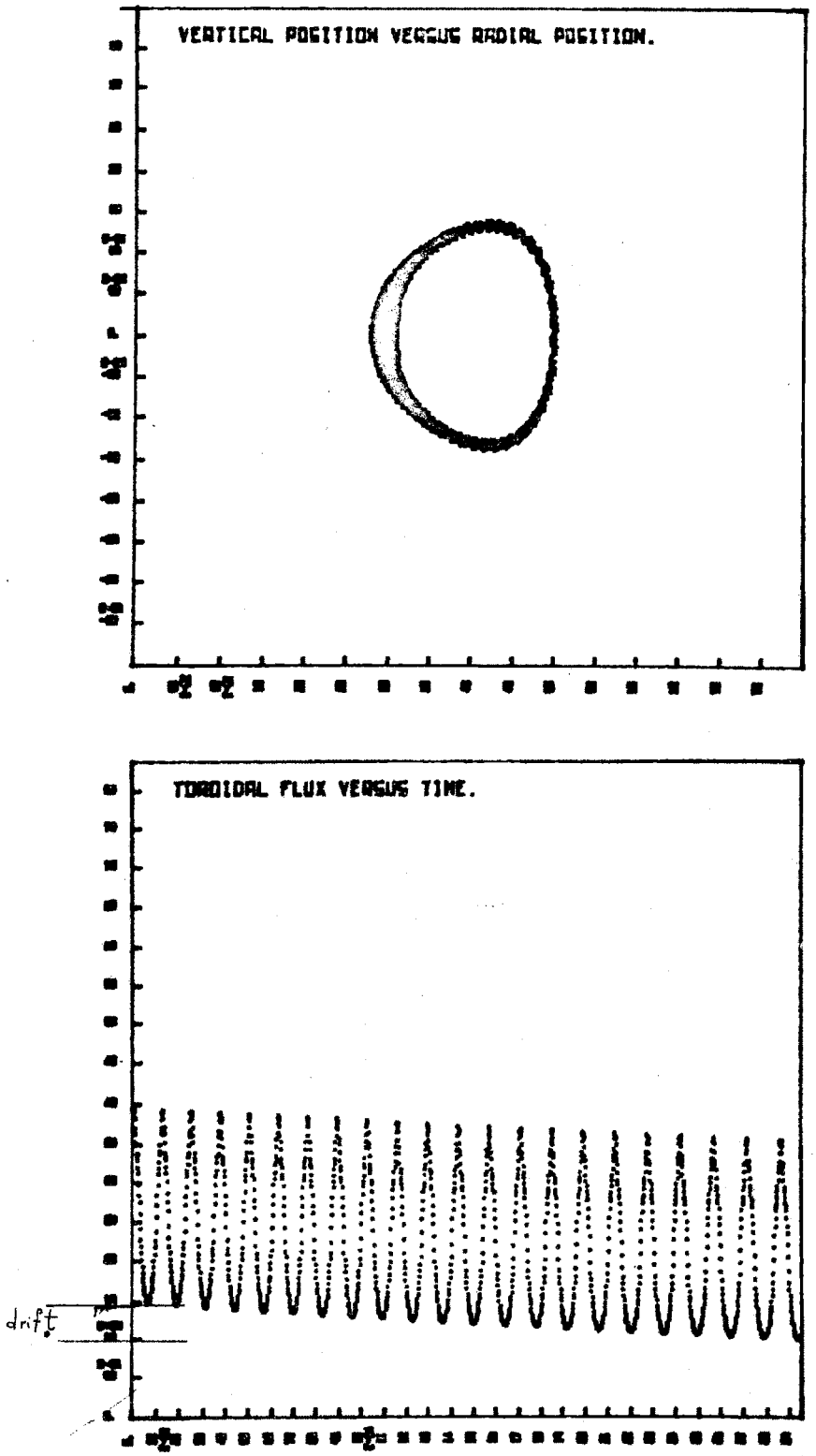

Figure II-8-1. The numerical drift associated with the simple predictor-corrector tracking algorithm.

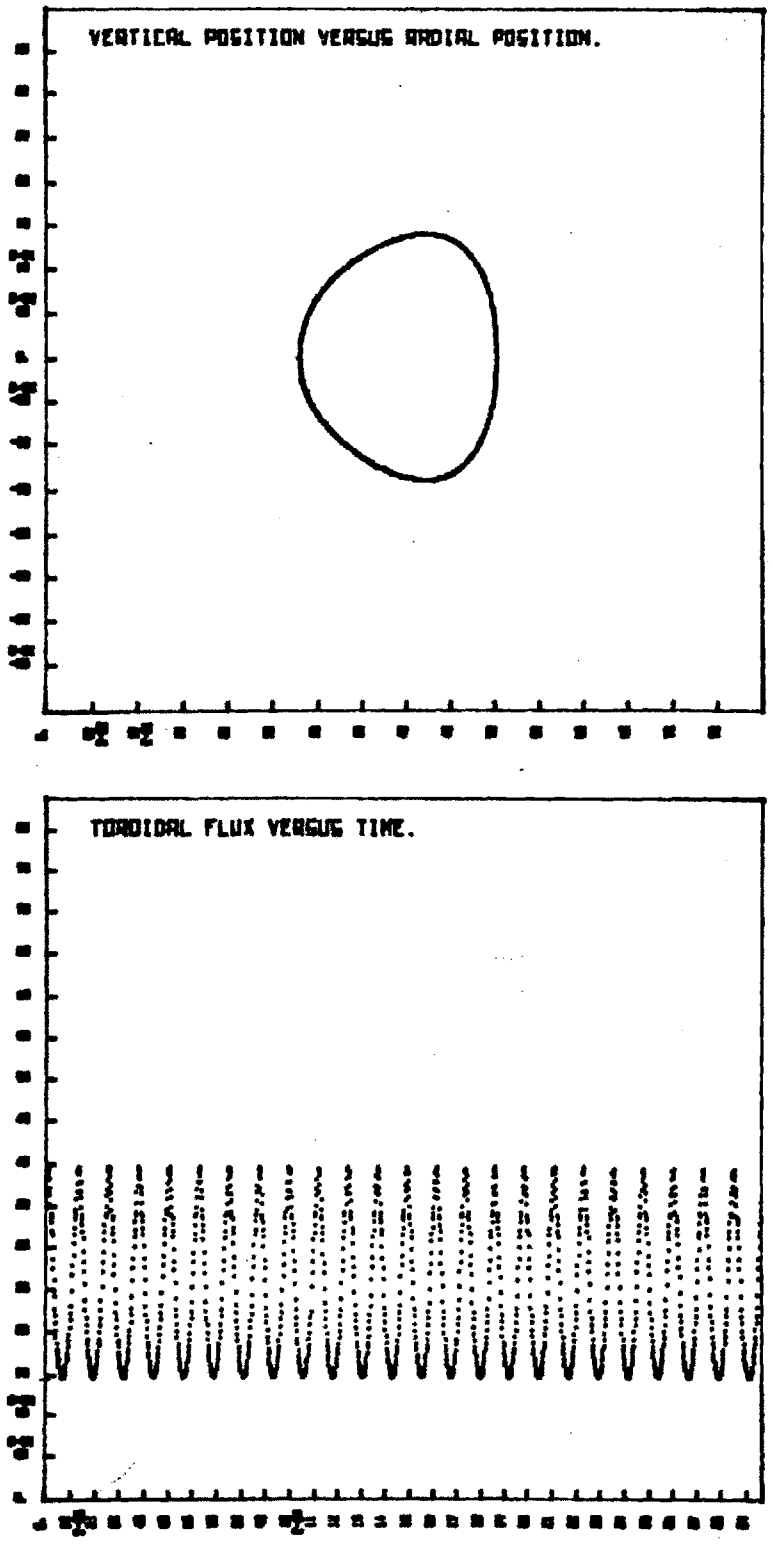

Figure II-B-2. No numerical drift was observed with an iterated predictor-corrector tracking algorithm.

point. This corrector iteration can, in general, be repeated as many times as desired. The track will converge on some value as the number of iteration steps is increased. Whether this value is close to the true solution to the differential equations being integrated is an open question. In this thesis, the strong closure of the vacuum-field orbits was taken as confirmation that the guiding-center equations were accurately integrated (see Figure II-B-2). The numerical drift was associated with an inaccuracy in calculating the curvature of the magnetic field. Accordingly, the error was more noticable for particles orbiting near the separatrix, where the field curvature is much greater than near the axis (by about two orders of magnitude). In general, more accurate tracking can be obtained either through a smaller step size or a higher order tracking algorithm. In the TAPIR code the step size was fixed by the spacing of the spline grids, so an iterated pushing algorithm was implemented. The following scheme was found to track all orbits within the spline grids accurately:

$\psi_t(r) / \psi_t$ (separatrix)	number of corrector iterations
0% - 50%	2
50% - 75%	3
75% - 100%	4
outside separatrix	4

Table II-B-1

Confirmation of accuracy in the tracking of alpha particles during their thermalization is given in Figures III-B-1, 2,

3. The effects of drag and scattering are present, but there is no systematic numerical drift towards the magnetic axis.

As previously mentioned, this tracking algorithm conserves the particle's energy. While designing the tracking procedures, another algorithm was tried, one in which the particle's energy was a free variable, and the time push of $V_{\|}$ was done by a numerical integration of $dV_{\|}/dt$. It was found that the simple predictor-corrector method produced a drift in the particle's energy of about .037 percent E_o per poloidal orbit, due to the inaccuracy of the $V_{\|}$ integration (see Figure II-B-3). In an attempt to reduce this fluctuation, a multiple iteration predictor-corrector scheme was tested (see Figure II-B-4). This method did reduce the energy drift by a factor of 50, but I finally decided to avoid the drift entirely by incorporating energy conservation into the pushing algorithm directly. This is acceptable since, as previously shown, the guiding-center equations conserve energy to at least second order. The energy drift is due to a numerical inaccuracy of the $V_{\|}$ time integration; it is not intrinsically a part of the guiding-center motion.

So far I have described the pushing algorithm for non-reflecting particles. A reflection will appear in the algorithm as a negative value for the predicted or corrected value for $V_{\|}^2$. When this occurs, the pushing algorithm abandons its attempt to push the particle onto the adjacent

Simple predictor-corrector tracking.

E_o = 3.5 MeV. dE / dt = - 10.1 keV/msec

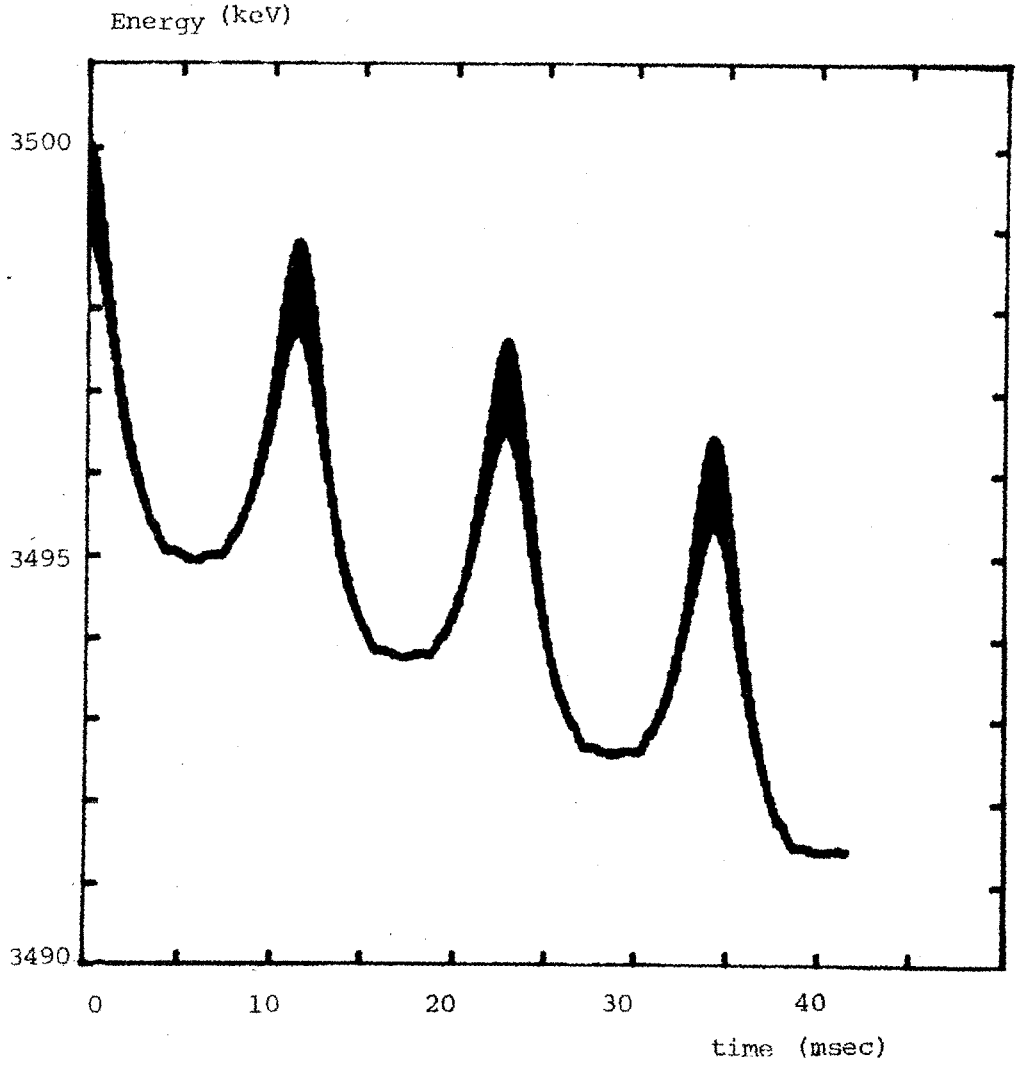

Figure II-B-3.

Double iteration predictor-corrector tracking.

E_o = 3.5 MeV. dE / dt = - 0.22 keV/msec

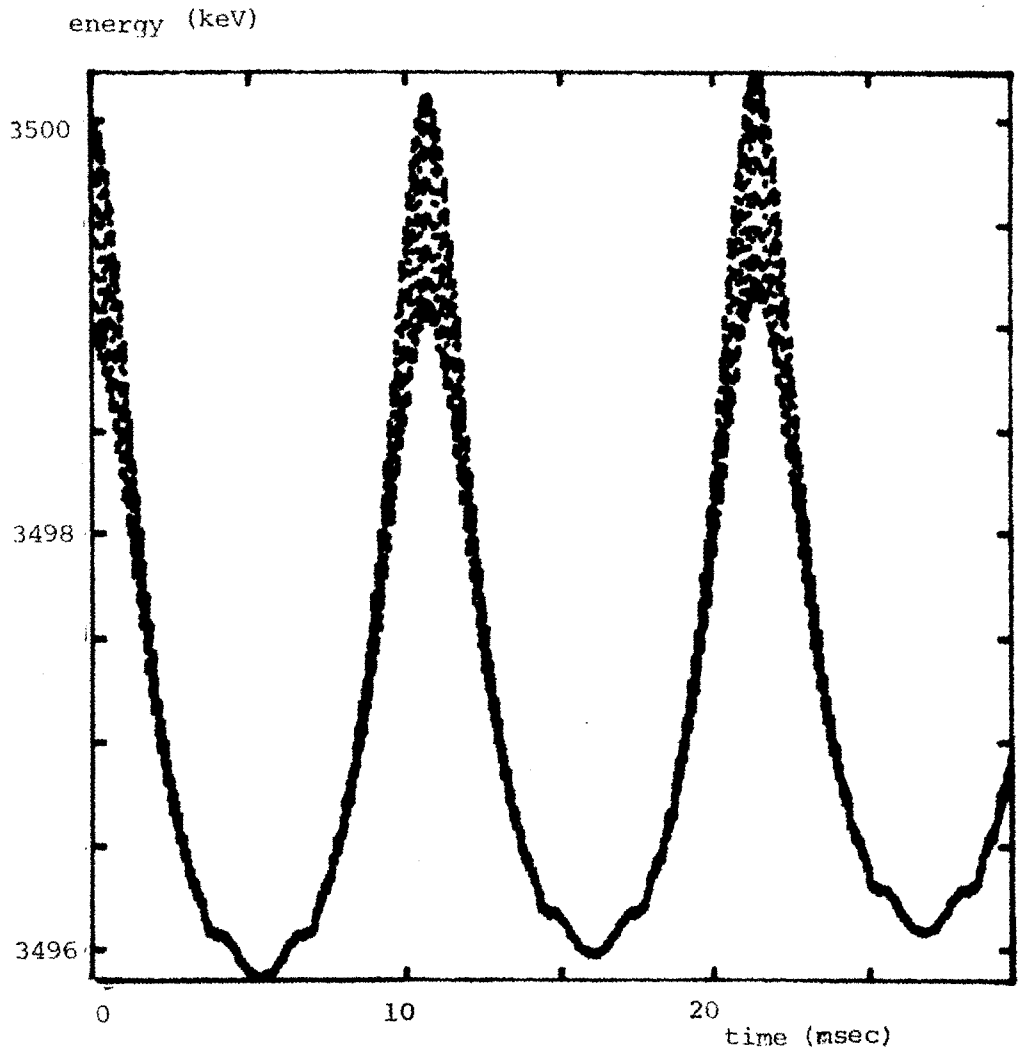

Figure II-B-4.

ϕ-plane grid. Instead, it calculates the point on the original ϕ-plane at which the particle will arrive after its reflection. I will now describe the procedure used to calculate this point.

With the field quantities and guiding-center velocity at the original point $\underline{r}(t=0)$ known, the guiding-center acceleration can be found by:[1]

$$\frac{dV_{\parallel}}{dt} = -\frac{\langle\mu\rangle}{m}\,\hat{b}\cdot\nabla B + \underline{V}_{\underline{E}\times\underline{B}}\cdot\frac{d\hat{b}}{dt} \qquad \text{[II-B-7]}$$

The $\underline{V}_{\underline{E}\times\underline{B}}$ term is much smaller than the $\langle\mu\rangle$ term for α-particles where $\underline{E} < 1$ MV/meter, hence the $\underline{V}_{\underline{E}\times\underline{B}}$ term was neglected for this bounce calculation. (Note that for the time steps in which the particle is not reflected, the $\underline{V}_{\underline{E}\times\underline{B}}$ term is represented in the energy equation [II-B-3].)

Defining the acceleration vector as:

$$\underline{A}_{GC}(0) = \hat{b}\,\frac{dV_{\parallel}}{dt}\bigg|_{t=0} \qquad \text{[II-B-8]}$$

the time Δt for a particle to reflect and return to the original ϕ-plane is:

$$\Delta t = -\frac{2\,\underline{V}_{GC}\cdot\hat{\phi}}{\underline{A}_{GC}\cdot\hat{\phi}} \qquad \text{[II-B-9]}$$

where $\hat{\phi}$ is the unit vector in the toroidal direction. The intersection point is:

$$\underline{r}(\Delta t) = \underline{r}(0) + \underline{V}_{GC}(0)\,\Delta t + \tfrac{1}{2}\underline{A}_{GC}(0)\,\Delta t^{2} \qquad \text{[II-B-10]}$$

$V_{\|}^2(\Delta t)$ is found through the energy conservation equation, and:

$$\sigma(\Delta t) = -\sigma(0) \qquad \text{[II-B-11]}$$

The mirroring push is now complete.

There is a very small region in velocity space where this mirroring algorithm will not work. This occurs where a particle has almost no parallel energy, and is at the bottom of a magnetic well. In this case, the possibility exists that the particle will mirror twice between two ϕ-planes.

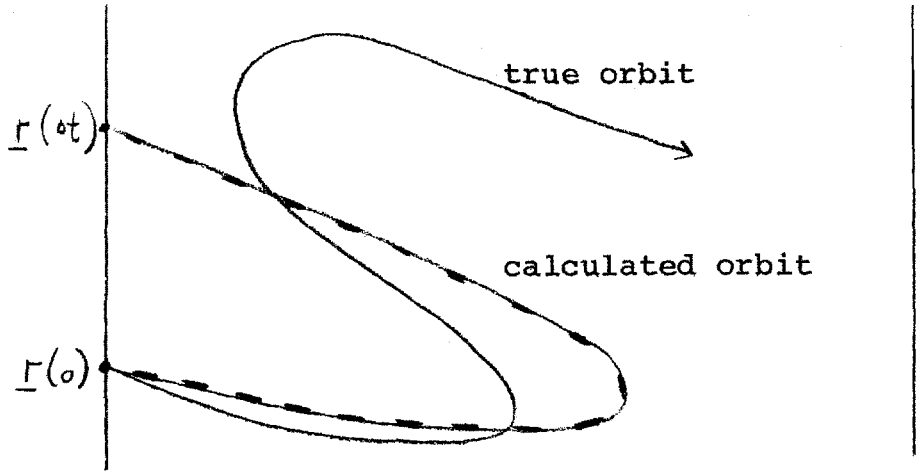

This deviation between the calculated and true orbits appears as a negative value for $V_{\|}^2(\Delta t)$. It occurs only when the bounce orbit lies almost exactly on a MOD B contour, so that $\hat{b} \cdot \nabla B$ (and hence $dV_{\|}/dt$ of the guiding-center) is almost zero and is fluctuating in sign. When a negative value appears for $V_{\|}^2(\Delta t)$ in the mirroring push, $mV_{\|}^2(\Delta t)$ was arbitrarily set at 1 eV. This had the effect of "jiggling" the particle's total energy from 0 to .005 percent. The

area on the velocity sphere where energy jiggling could occur is small, about 10^{-5} of the total surface. In addition, the particle's orbit must lie close to a MOD B contour for energy jiggling to be required. In general, this would occur in the ϕ-plane where the modulating B field is at a minimum. With 32 ϕ-planes per module, one would thus expect energy jiggling to be required about once every $32/10^{-5}$ iterations during all the tracking runs. With the average α-particle requiring about 10^5 iterations, about $1/32 \tilde{=} 3.1$ percent of the particles should require an energy jiggle. In reality, 5.3 percent of the alpha particles tracked required energy jiggling (with 30 percent of these requiring two or more jiggles), and 60 percent of the jiggling occurred with the alpha particles almost fully thermalized, when $\tau_{i\alpha}^{scat} < \tau_{poloidal\ orbit}$; and the particles were making large excursions on the velocity sphere.

I will now compare the effect of energy jiggling to the effect of neglecting ion-alpha energy scattering during the alpha particle's thermalization. As is discussed in Chapter IV, this energy scattering is:

$$\frac{\langle (\Delta v_{\parallel})^2 \rangle}{\Delta t} = \frac{n_i Z_\alpha^2 Z_i^2 e^4 \ln \Lambda}{2\pi \epsilon_0^2 m_\alpha^2} \frac{1}{\nu_\alpha} G\left(\frac{\nu_\alpha}{\nu_{th\,i}}\right) \qquad \text{[II-B-12]}$$

where $G(X) \tilde{=} \frac{1}{2X^2}$ for $X >> 1$.

Defining the energy scattering correlation time as:

$$\tau_\alpha^{E\ scat} = \nu_\alpha^2 \frac{\Delta t}{\langle (\Delta V_\parallel)^2 \rangle} \qquad \text{[II-B-13]}$$

I find that, for a background plasma with $n_i = 3 \cdot 10^{20}$/meter, $T_i = 8000$ eV, and $m_i = 2.5$ u, $\tau_\alpha^{E\ scat} = 1630$ sec for a 3.5 MeV α-particle. For 1 msec of tracking,

$$\frac{\Delta E}{E} = 2\frac{\Delta V}{V} = 2\sqrt{\frac{10^{-3}\ sec}{1630\ sec}} = .167 \qquad \text{[II-B-14]}$$

Thus we see that the effect of an energy jiggle, $(\Delta E/E)_{max} \tilde{=} .005$ percent, is much less than the effect of neglecting ion-alpha energy scattering for a msec of particle tracking. (Ion-alpha energy scattering was neglected in the tracking code because it is so small compared to the electron alpha drag term, where $\Delta E/E > 2\%$ for 1 msec.) The implementation of energy jiggling in the tracking code could therefore not have affected the confinement results to a marked degree.

As a particle apprcaches a reflection point, the direction of V_{GC} changes rapidly, and it is no longer appropriate to assume it is constant during the time required to reach the next ϕ-plane. Therefore, when $|V_\parallel| < |V_\perp|$, the predictor point of the pushing algorithm is found by following the local B field line to the next ϕ-plane. This results in a more accurate average of the particle's motion between the two ϕ-planes.

This completes the description of the vacuum orbit particle tracker. Its design was dictated by the nature of

the numerical problems of the orbit integration. Direct computation of local fields by integrating line current segments would have been 200 times slower than the spline calculation. Given the requirement of computing B from a grid, only spline interpolation was found to give the accuracy needed for such extended tracking as 5000 poloidal orbits. Two-dimensional interpolation was chosen since it is four times faster than three-dimensional interpolation, and this decision made the time Δt between steps a varying quantity. This in turn precluded the use of a Runga-Kutta or past-history integration scheme, since these require fixed time steps. The multiple-iteration predictor-corrector algorithm was the tracking method implemented because it allows a varying time step.

Mapping of Plasma Parameters onto the Flux Surfaces

In studying the alpha particles' interaction with the background plasma, the plasma parameters of voltage, density, and electron temperature had to be known along the particles' orbits. This was done by mapping the plasma profiles onto the toroidal flux surface profiles. As discussed in Appendices C and D, $\psi_{toroidal}$ and $\nabla\psi_{toroidal}$ could be calculated anywhere within the separatrix. The plasma parameters were then calculated with the following equations:

$$n(\psi_t) = n_{axis}\left(1 - \frac{\psi_t}{\psi_{cR}}\right)^{p_n} \qquad \text{(density profile)} \quad [\text{II-B-15}]$$

$$\phi(\psi_t) = \phi_{axis}\left(1 - \frac{\psi_t}{\psi_{CR}}\right)^{p_\phi} \qquad \text{(voltage profile)} \quad \text{[II-B-16]}$$

$$T_e(\psi_t) = T_{e_{axis}}\left(1 - \frac{\psi_t}{\psi_{CR}}\right)^{p_{T_e}} \qquad \text{(temperature profile)} \quad \text{[II-B-17]}$$

$$\underline{E}(\underline{r}) = -\underline{\nabla}\,\phi(\psi_t) \qquad \text{(electric field profile)}$$

$$= -\phi_{axis}\, p_\phi \left(1 - \frac{\psi_t}{\psi_{CR}}\right)^{p_\phi - 1}\left(-\frac{\underline{\nabla}\,\psi_t}{\psi_{CR}}\right)$$

$$= \phi(\psi_t)\, p_\phi \frac{\underline{\nabla}\,\psi_t(\underline{r})}{\psi_{CR} - \psi_t} \qquad \text{[II-B-18]}$$

with $\psi_{CR} = \psi_{critical}$ = toroidal flux at separatrix, p_n, p_ϕ, and p_{T_e} are constants that determine the flatness of the parameter profiles. Once $n(\underline{r})$ and $T_e(\underline{r})$ are known, electron and ion drag and ion pitch angle diffusion forces are calculated. Electron drag on alpha particles has been derived by Chandrasekhar[3] and discussed by Spitzer.[4] In the tracking code, a good approximation of their results was used, which was given in Rose and Clark.[5] The approx-

imation is:

$$\frac{d U_\alpha}{d t} = \frac{q_e^2 q_\alpha^2 n_e m_e (\ln \Lambda) \left[1 - 2 U_\alpha / 3 k_B T_e \right]}{\left[1 + \frac{4}{3\sqrt{\pi}} \left(\frac{m_e U_\alpha}{m_\alpha k_B T_e} \right)^{3/2} \right] 2\pi \epsilon_o^2 m_\alpha \sqrt{2\pi m_e k_B T_e}} \qquad \text{[II-B-19]}$$

$$\text{with} \quad \Lambda = \frac{12\pi \left(\epsilon_o k_B T_e / e^2 \right)^{3/2}}{\sqrt{n_e}} \qquad \text{(MKS units)} \qquad \text{[II-B-20]}$$

As discussed in Chapter IV, the ion-alpha pitch angle diffusion coefficient may be written as:

$$\frac{\langle (\Delta v_\perp)^2 \rangle}{\Delta t} = \frac{n_i Z_i^2 Z_\alpha^2 e^4 \ln \Lambda}{2\pi \epsilon_o^2 m_\alpha^2 v_\alpha} \left[\Phi\left(\frac{v_\alpha}{v_{th_i}} \right) - G\left(\frac{v_\alpha}{v_{th_i}} \right) \right] \qquad \text{[II-B-21]}$$

where $\Phi(X) - G(X) \cong 1$ for $X >> 1$. The time to scatter one radian is:

$$\tau_{i\alpha}^{scat} = v_\alpha^2 \frac{\Delta t}{\langle (\Delta v_\perp)^2 \rangle}$$

$$= \frac{2\pi \epsilon_o^2 m_\alpha^2 v_\alpha^3}{n_i Z_i^2 Z_\alpha^2 e^4 \ln \Lambda} \qquad \text{[II-B-22]}$$

The ion-alpha drag term may be written as:

$$\frac{\langle \Delta v_\parallel \rangle}{\Delta t} = - \frac{n_i Z_i^2 Z_\alpha^2 e^4 \ln \Lambda}{2\pi \epsilon_o^2 m_\alpha^2} \left(1 + \frac{m_\alpha}{m_i} \right) G\left(\frac{v_\alpha}{v_{th_i}} \right) \qquad \text{[II-B-23]}$$

where $G(X) \cong \frac{1}{2X^2}$ for $X >> 1$.

The energy loss rate due to this drag is:

$$\frac{\Delta E}{\Delta t} = \frac{\Delta\left(\frac{1}{2} m v_{\parallel}^2\right)}{\Delta t} = \frac{m v_{\parallel} (\Delta v_{\parallel})}{\Delta t} \qquad \text{[II-B-24]}$$

The energy slowing down time is:

$$\tau_{i\alpha}^{E} = E \left| \frac{\Delta t}{\Delta E} \right| = \frac{\frac{1}{2} m_\alpha v_\alpha^2}{m_\alpha v_\alpha \left| \frac{\langle \Delta v_{\parallel} \rangle}{\Delta t} \right|}$$

$$= \frac{v_\alpha^3 \, 2\pi \epsilon_0^2 m_\alpha^2}{n_i Z_\alpha^2 Z_i^2 e^4 (\ln \Lambda)} \left(1 + \frac{m_\alpha}{m_i}\right)^{-1} \qquad \text{[II-B-25]}$$

$$\tau_{i\alpha}^{E} = \tau_{i\alpha}^{scat} \left(1 + \frac{m_\alpha}{m_i}\right)^{-1}$$

$$= .385 \, \tau_{i\alpha}^{scat} \quad \text{for} \quad m_i = 2.5 \, u \qquad \text{[II-B-26]}$$

I will now describe how drag and pitch-angle scattering forces were included in the tracking code. After the particle has been pushed from one ϕ-plane grid to another in time Δt, the energy given to the electrons and DT ions is calculated from the equations:

$$Q_e = -\Delta t \quad dU_\alpha/dt\big|_{\text{electron drag}} \qquad \text{[II-B-27]}$$

$$Q_i = \Delta t \quad U_\alpha/(.385 \, \tau_{i\alpha}^{scat}) \qquad \text{[II-B-28]}$$

Q_e and Q_i are then subtracted from the particle's kinetic energy, while keeping the velocity space direction

fixed. Then, this direction is changed slightly by the scattering algorithm. This algorithm works by scattering a point from the $V_{//} = V$ point on the velocity sphere, rotating the $V_{//} = V$ point to the particle's velocity space position, and then moving the scattered point with the same rotation transformation (see Figure II-B-5). Working in spherical coordinates, the coordinate relationship is:

$$Z = \cos \theta \qquad \text{[II-B-29]}$$

$$X = \sin \theta \cos \phi \qquad \text{[II-B-30]}$$

$$Y = \sin \theta \sin \phi \qquad \text{[II-B-31]}$$

The location of the point scattered from the $V_{//} = V$ point is:

$$\theta^{\text{scat pt}} = \pi/2 + \varepsilon_1 \qquad \text{[II-B-32]}$$

$$\phi^{\text{scat pt}} = \pi/2 + \varepsilon_2 \qquad \text{[II-B-33]}$$

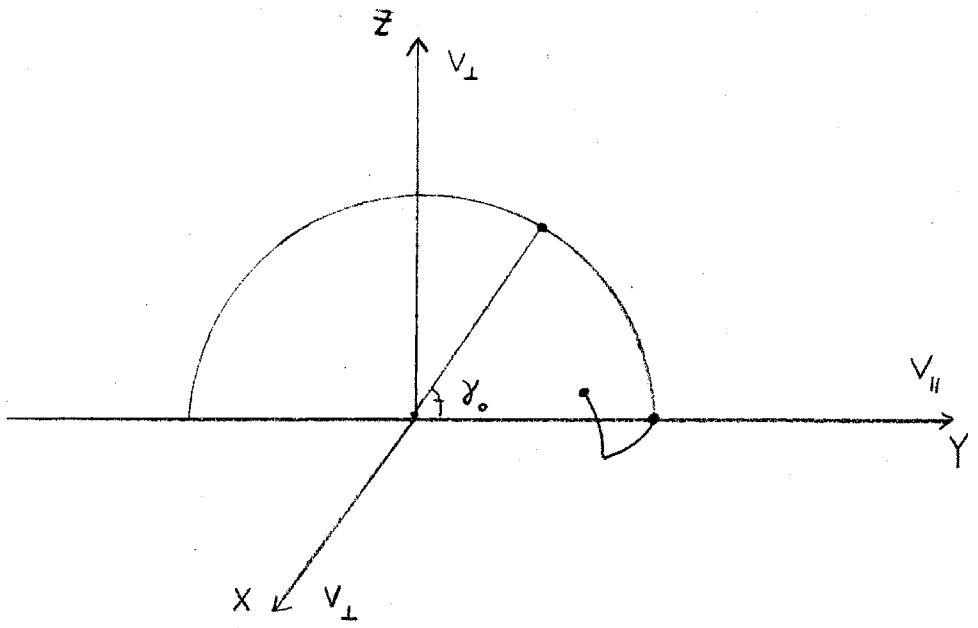

Figure II-B-5

where $\varepsilon_1 = |\varepsilon| \sin(\hat{\varepsilon})$ [II-B-34]

$\varepsilon_2 = |\varepsilon| \cos(\hat{\varepsilon})$ [II-B-35]

$\hat{\varepsilon}$ = random angle from 0 to 2π

$|\varepsilon| = \sqrt{\Delta t/\tau_{i\alpha}^{scat}}$ [II-B-36]

where $\tau_{i\alpha}^{scat}$ = 1 radian scattering time.

Making use of the following identities:

$\sin(\pi/2 + \chi) = \cos\chi$ [II-B-37]

$\cos(\pi/2 + \chi) = -\sin\chi,$ [II-B-38]

the rectangular coordinates of the scattered point are:

$Z^{scat\ pt} = -\sin\varepsilon_1$ [II-B-39]

$X^{scat\ pt} = -\cos\varepsilon_1 \sin\varepsilon_2$ [II-B-40]

$Y^{scat\ pt} = \cos\varepsilon_1 \cos\varepsilon_2$ [II-B-41]

The scattered point is rotated toward the particle's original position by the equation:

$$Y_{new}^{scat\ pt} = Y^{scat\ pt} \cos\gamma_o - Z^{scat\ pt} \sin\gamma_o \quad \text{[II-B-42]}$$

The new value of V is then found by the equation:

$$\cos\gamma_o^{new} = Y_{new}^{scat\ pt} = \cos\varepsilon_1 \cos\varepsilon_2 \cos\gamma_o + \sin\varepsilon_1 \sin\gamma_o \quad \text{[II-B-43]}$$

with $V_{\parallel}^{new} = V \cos\gamma_o^{new}$ [II-B-44]

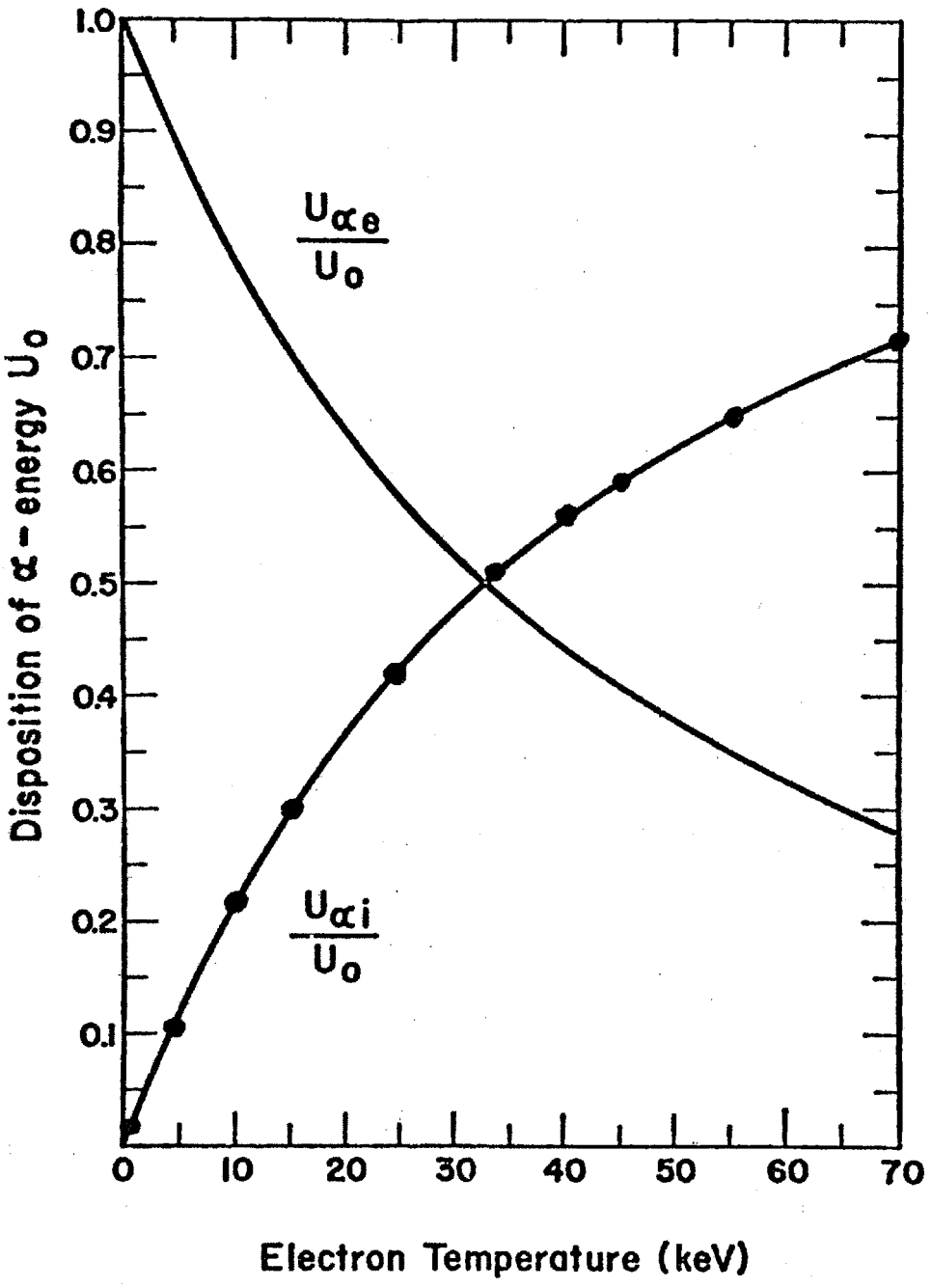

Figure II-B-6. Fraction of α-Particle Energy Given to Electrons ($U_{\alpha e}/U_o$) and to D-T Ions ($U_{\alpha i}/U_o$) vs Electron Temperature, if the α's are Fully Thermalized.

(plotted points are the tracking code results)

The particle's value for μ is then recomputed so as to be consistent with the particle's new values of kinetic energy and $V_{\parallel}^{new}$. This completes the drag and scattering portion of the tracking procedure.

In order to test the slowing down algorithm of the tracking code, several runs were made with varying values of T_e, and the energy deposition ratios to ions and electrons for fully thermalized alphas were obtained. These values are plotted in Figure II-B-6, along with the correct energy deposition curve. The tracking code accurately matches the correct curve.[6]

C. Single Particle Confinement in Helical Systems

This section begins by showing that helical momentum is an absolute invariant of particle motion in helical cylindrical systems, and that particles in such systems are therefore well confined radially. The section concludes with an analysis of the trapped and circulating regions in phase space of particles in helical toroidal systems.

The first step in calculating the canonical momentum in a helically symmetric system is to find the system's metric. The right-handed coordinate system (r, α, β) is defined by Figure II-C-1.

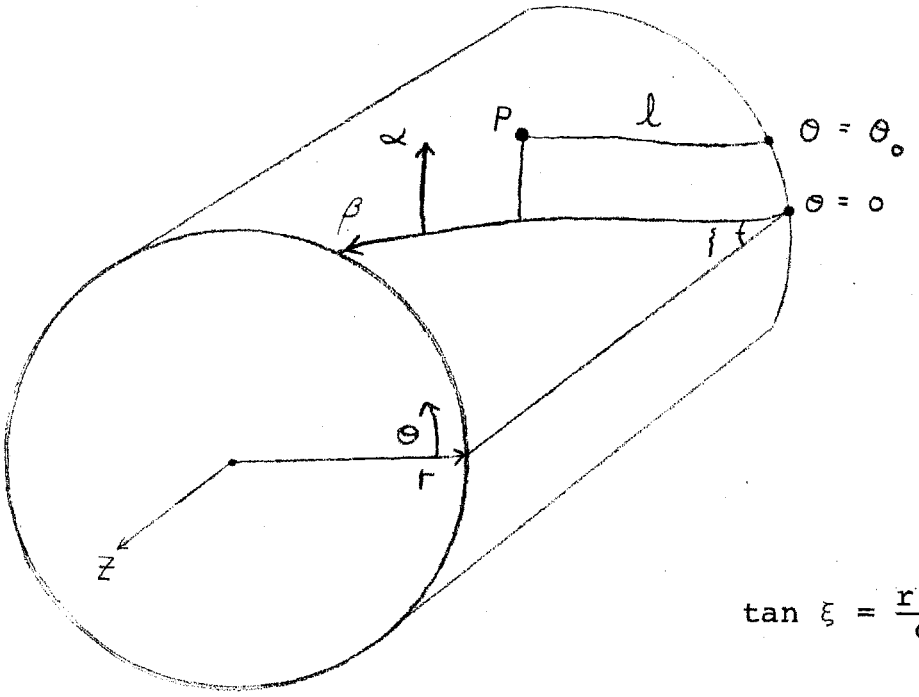

$$\tan \xi = \frac{r\, d\theta}{dZ} = \frac{2\pi r}{p} \qquad \text{[II-C-1]}$$

Figure II-C-1

$$P = P(r, \theta, Z) = P(r, \alpha, \beta)$$

In this reference frame, $\hat{\beta}$ is in the direction of helical symmetry (with $\Delta\beta = 2\pi \rightarrow \Delta Z$ = one pitch length), r is the distance from the helical axis, and $\hat{\alpha} = \hat{\beta} \times \hat{r}$ (α measured from 0 to 2π). A point's (α, β) location may be obtained from its (θ, Z) values through the following equations:

$$\ell = Z/\cos \xi \qquad \text{[II-C-2]}$$

$$\theta_o = \theta - \frac{\ell}{r} \sin \xi = \alpha \qquad \text{[II-C-3]}$$

$$\alpha = \theta - \frac{2\pi Z}{p} \qquad \text{[II-C-4]}$$

$$q \equiv 1 + \left(\frac{2\pi r}{p}\right)^2 \qquad \text{[II-C-5]}$$

$$\beta = \frac{2\pi}{pq} (\ell + r\, \theta_o \sin \xi)$$

$$= \frac{2\pi}{pq} (Z \cos \xi + r\, \theta \sin \xi) \qquad \text{[II-C-6]}$$

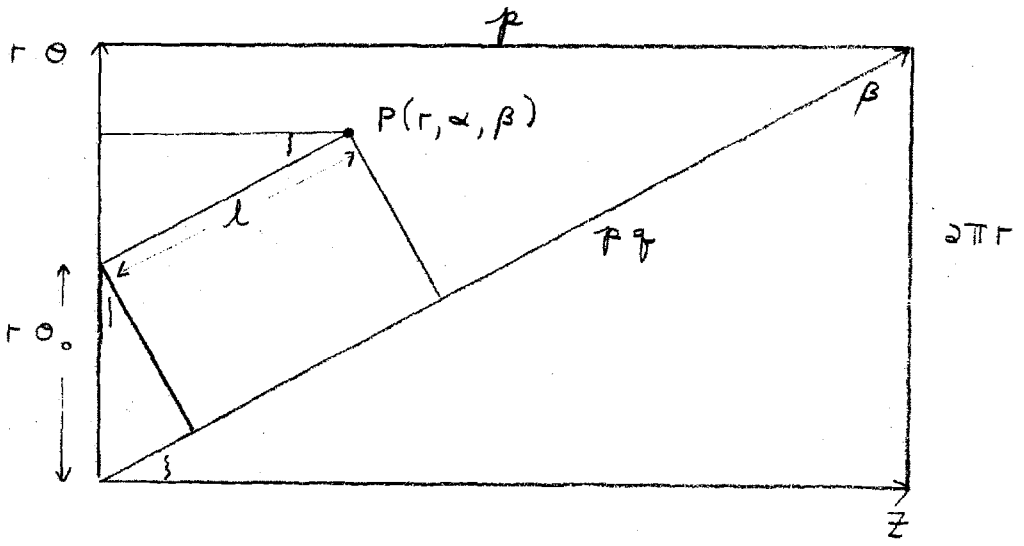

Figure II-C-2

The inverse transformations are:

$$z = \frac{p\beta}{2\pi} - \frac{r\alpha \tan\delta}{q^2} \qquad \text{[II-C-7]}$$

$$\theta = \alpha + \frac{2\pi z}{p} = \frac{\alpha}{q^2} + \beta \qquad \text{[II-C-8]}$$

The metric in cylindrical coordinates is:

$$(ds)^2 = (dr)^2 + r^2\,(d\theta)^2 + (dz)^2 \qquad \text{[II-C-9]}$$

Substituting the transformations to helical coordinates, the helical metric is:

$$(ds)^2 = (dr)^2 + \left(\frac{r}{q}\right)^2 (d\alpha)^2 + \left(\frac{pq}{2\pi}\right)^2 (d\beta)^2 \qquad \text{[II-C-10]}$$

This metric will now be used to derive the helical momentum (p_β) of a particle in a helically symmetric magnetic field. The non-relativistic Lagrangian for a charged particle is:

$$\mathcal{L} = T - V = \frac{1}{2} m \dot{\underline{X}}^2 + e \dot{\underline{X}} \cdot \underline{A}$$

$$= \frac{m}{2}\left[\dot{r}^2 + \left(\frac{r}{q} \dot{\alpha} \right)^2 + \left(\frac{R q}{2\pi} \dot{\beta} \right)^2 \right]$$

$$+ e\left[A_r \dot{r} + A_\alpha \frac{r}{q} \dot{\alpha} + A_\beta \frac{R q}{2\pi} \dot{\beta} \right]$$

[II-C-11]

The canonical momentum $\vec{p}$ conjugate to the position coordinate $\underline{X}$ is obtained by the definition:

$$\vec{p}\,(\underline{X}) = \frac{\partial \mathcal{L}}{\partial \dot{\underline{X}}}$$

[II-C-12]

Thus, the helical momentum may be written as:

$$\frac{\partial \mathcal{L}}{\partial \dot{\beta}} = p_\beta = m\left(\frac{R q}{2\pi} \right)^2 \dot{\beta} + e A_\beta \frac{R q}{2\pi}$$

[II-C-13]

Since $\frac{\partial \mathcal{L}}{\partial \beta} = 0$, the Euler-Lagrange equation of motion $\left[\frac{d}{dt}\left(\frac{\partial \mathcal{L}}{\partial \dot{X}_i} \right) - \frac{\partial \mathcal{L}}{\partial X_i} = 0 \right]$ implies that $\dot{p}_\beta = 0$, thus p_β is an absolute invariant of the motion.

A_β in equation II-C-13 may be expressed in terms of the helical flux function (note helical -- must not be confused with the toroidal flux function ψ_t used elsewhere):

$$\psi_\alpha = \oint_{\text{helical path}} \underline{A} \cdot d\underline{\ell} \qquad \text{[II-C-14]}$$

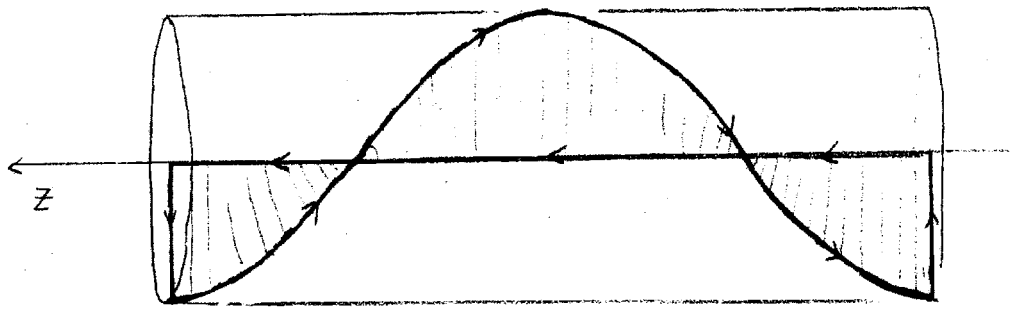

Figure II-C-3

(In a right-handed coordinate system, path of integration is as shown in Figure II-C-3, a positive ψ_α points in direction of positive α.)

By setting the gauge of A such that $A_f = 0$ on axis, equation II-C-14 may be written as:

$$\psi_\alpha(r_0, \alpha_0) = \int_0^{2\pi} A_\beta \frac{\rho}{2\pi} d\beta \Big|_{r=0} + \int_0^{r_0} A_r \, dr + \int_{2\pi}^{0} A_\beta \frac{\rho}{2\pi} d\beta \Big|_{r=r_0} + \int_{r_0}^{0} A_r \, dr$$

$$= - \int_0^{2\pi} A_\beta \frac{p q}{2\pi} \, d\beta \Big|_{r = r_0}$$

[II-C-15]

Along the outer helical path, A_β is a constant, since all quantities are symmetric with respect to β. Thus:

$$\psi_\alpha(r, \alpha) = -A_\beta(r, \alpha)\, p q \qquad \text{[II-C-16]}$$

Substituting this relation into equation II-C-13 gives:

$$p_\beta = m \frac{p q}{2\pi} \dot{\rho}^2 - \frac{e}{2\pi} \psi_\alpha(r, \alpha)$$

$$= m \left[\frac{p}{2\pi} v_z + v_\theta r \right] - \frac{e}{2\pi} \psi_\alpha(r, \alpha)$$

[II-C-17]

I will now show that charged particles near the helical axis are radially confined when the following condition is satisfied:

$$\rho_\ell = \frac{m V}{e B} \ll a_c \,, \qquad \text{[II-C-18]}$$

where a_c is the radius of the windings.

Assume a particle near the axis makes a small radial displacement. Conservation of p_β requires:

$$m \left[\Delta v_z + t_{\text{an}} \{ v_\theta \right] = \frac{e}{p} \Delta(\psi_\alpha)$$

[II-C-19]

Near the magnetic axis, the helical flux function may be approximated by:

$$\psi_\alpha(r, \alpha) = -\pi r^2 B_{Z_o} \qquad \text{[II-C-20]}$$

where $B_{Z_o} = \dfrac{\mu_o \ell I}{p}$

ℓ = number of windings

I = current per winding

The exact equation for $\psi_\alpha(r, \alpha)$ is given by equation II-C-25. Viewed longitudinally, a helical ribbon of radius r extending one pitch length in Z covers a circle of radius r. Near the magnetic axis, $B \cong B_{Z_o}\hat{z}$, hence the form of equation II-C-20. For a system with $\ell = 3$ and $2\pi a_c/p = .889$, it was found that this approximation had a 6.3% error at $r = .125\ a_c$ and a 13% error at $r = .25\ a_c$. Conservation of energy limits the maximum $\Delta[v_Z + \tan\xi\, v_\theta]$ to 2V, where V is the particle's speed (assuming $\tan\xi \leq 1$). When conservation of μ is considered also, the maximum change in $[v_Z + \tan\xi\, v_\theta]$ is more accurately $2V \tan\xi$, since $B = B_{o_Z}\hat{z}$ near the magnetic axis; hence the magnitude of V_Z and V are approximately constant. An expression for the maximum radial displacement may be written as:

$$\frac{e}{p}\left(\Delta\, \pi r^2 B_{z_o}\right)_{MAX} = m \tan\xi\ 2V$$

$$\frac{2\pi r}{p} \; e B_{z_0} (\Delta r)_{MAX} = m (2V) t_{on} \}$$

$$(\Delta r)_{MAX} = \frac{2 m V}{e B_{z_0}} \cong 2 \rho_l \qquad \text{(II-C-21)}$$

The particle is limited to a radial displacement of the order of a Larmor radius. This limit should be valid when $r \leq .25\ a_c$.

In order to verify this approximate result, a computer code was written which incorporated exact values for the helical field:[7]

$$B_r = B_{z_0} \sum_{m=1}^{\infty} C_m \; m l \left(\frac{2\pi a}{p}\right) K'_{ml} \left(m l \frac{2\pi a}{p}\right) \cdot I'_{ml} \left(m l \frac{2\pi r}{p}\right) \sin(m l \alpha)$$

$$B_\theta = B_{z_0} \sum_{m=1}^{\infty} C_m \; m l \left(\frac{a}{r}\right) K'_{ml} \left(m l \frac{2\pi a}{p}\right) \cdot I_{ml} \left(m l \frac{2\pi r}{p}\right) \cos(m l \alpha)$$

$$B_z = B_{z_0} \left[1 - \sum_{m=1}^{\infty} C_m \; m l \left(\frac{2\pi a}{p}\right) K'_{ml} \left(m l \frac{2\pi a}{p}\right) \cdot I_{ml} \left(m l \frac{2\pi r}{p}\right) \cos(m l \alpha) \right]$$

$$\psi_h = B_{z_0} \left[-\pi r^2 + 2\pi r a \sum_{m=1}^{\infty} C_m K'_{ml} \left(m l \frac{2\pi a}{p}\right) \cdot I'_{ml} \left(m l \frac{2\pi r}{p}\right) \cos(m l \alpha) \right] \qquad \text{[II-C-22-25]}$$

with ℓ windings occupying a total fraction of f_o of the $r = a$ surface, and:

$$C_m = \frac{2 \sin(m \pi f_o)}{m \pi f_o} \qquad \text{[II-C-26]}$$

Three equations limit the regions in phase space a particle may enter:

1) $$E = \frac{1}{2} m \left(v_z^2 + v_\theta^2 + v_r^2 \right) \qquad \text{[II-C-27]}$$

2) $$\mu = \frac{1}{2} m v_\perp^2 / B \qquad \text{[II-C-28]}$$

3) $$p_h = m \left(v_\theta r + v_z p / 2\pi \right) - \frac{e \psi_h}{2\pi} \qquad \text{[II-C-29]}$$

The computer program would start a particle at an initial spatial location and pitch angle, and then search both radially and poloidally for possible values of (v_Z, v_θ, v_r) that would satisfy all three equations. An exhaustive search of pitch angle and configuration space (for $r < a_c$) was made with the following fixed parameters:

a_c	4 meters
ℓ	3
f_o	30%
B_{Z_o}	6.67 tesla
p	28.27 meters
particle type	3.5 MeV α-particle

The results of the scan showed that the extent of radial excursions was insensitive to r and α, and moderately dependent on the particle's pitch angle. Well circulating

α-particles ($V_{\parallel} \geq V_{\perp}$) had maximum radial excursions of .5 to 2.0 cm, while particles with $V_{\perp} >> V_{\parallel}$ had maximum radial excursions of 1.0 to 3.5 cm. These exact results are well within the limits given by the approximation in equation II-C-21.

Helical, Toroidal Systems

The motion of guiding-centers in helical toroidal fields is complex. Unlike tokamaks or linear torsatrons, there is no direction of symmetry in the magnetic field and this lack of an ignorable coordinate hinders the analytic categorization of particle orbits. Nevertheless, several observations can be made on the types of particle orbits by examining the orbits of some test particles. In order to simplify the analysis, these particles were launched in a torsatron without a background plasma density and voltage profile. In a scan through pitch-angle space, a set of 3.5 MeV α-particles was launched in the torsatron B machine ($r_o/a_c = 6$) at the minor axis ($R = R_o = 24$ meters). The orbit tracks are shown in Figure II-C-4.

Well circulating particles exhibit periodic motion on well defined flux surfaces. For a particle launched on the minor axis, the $\underline{B} \times \underline{\nabla}B$ drift is initially in the downward direction. Once the particle leaves the weakly sheared fields of the axis region, it will follow the local curvature of the magnetic field, drifting to either the inside or outside of the torus. For the torsatrons of

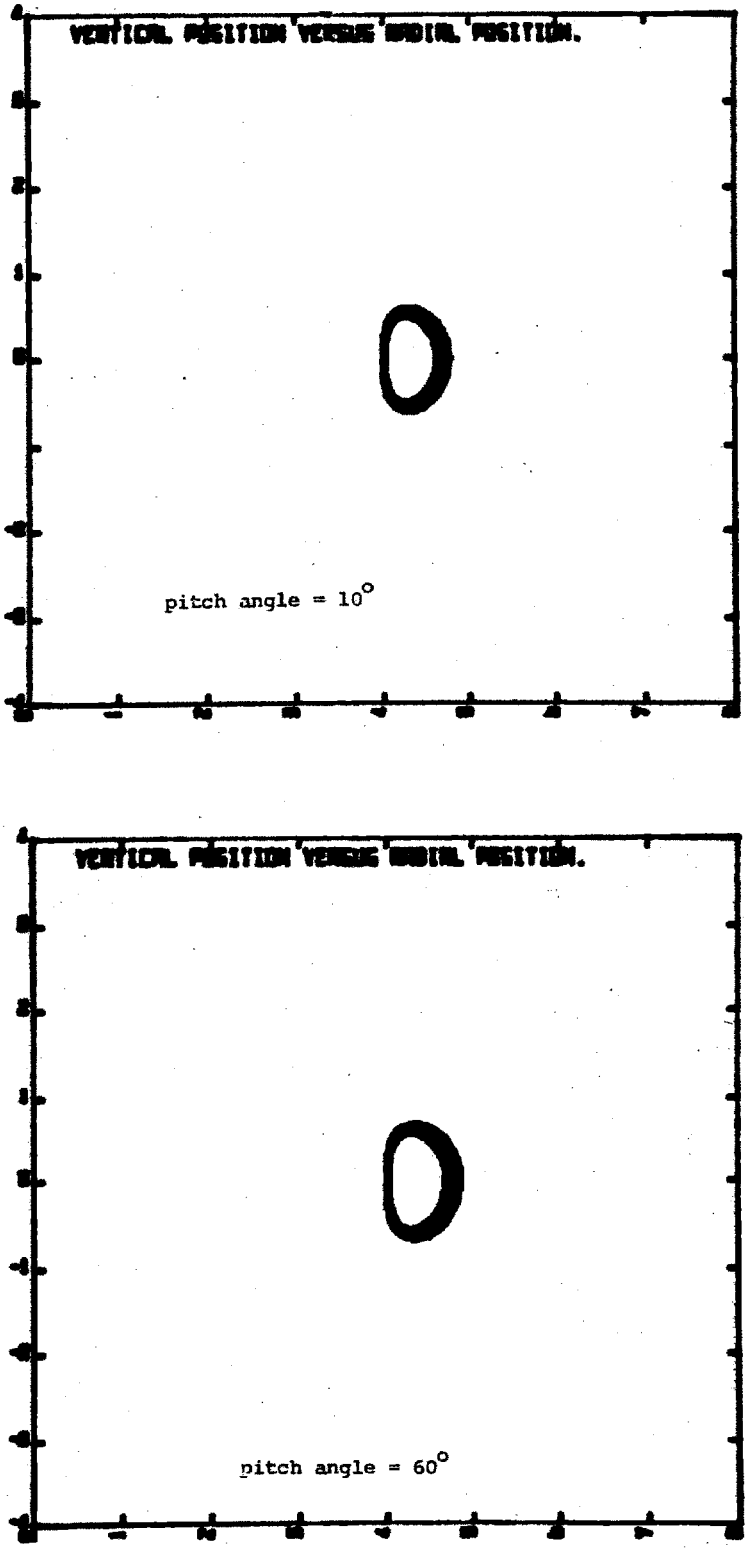

Figure II-C-4. Guiding-center orbit for different pitch angles.

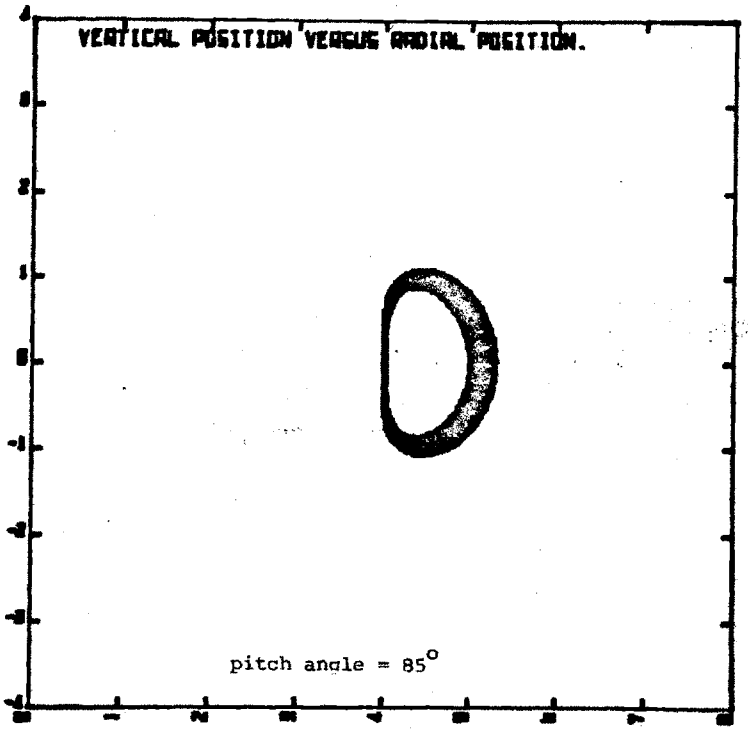
VERTICAL POSITION VERSUS RADIAL POSITION.
pitch angle = 85°

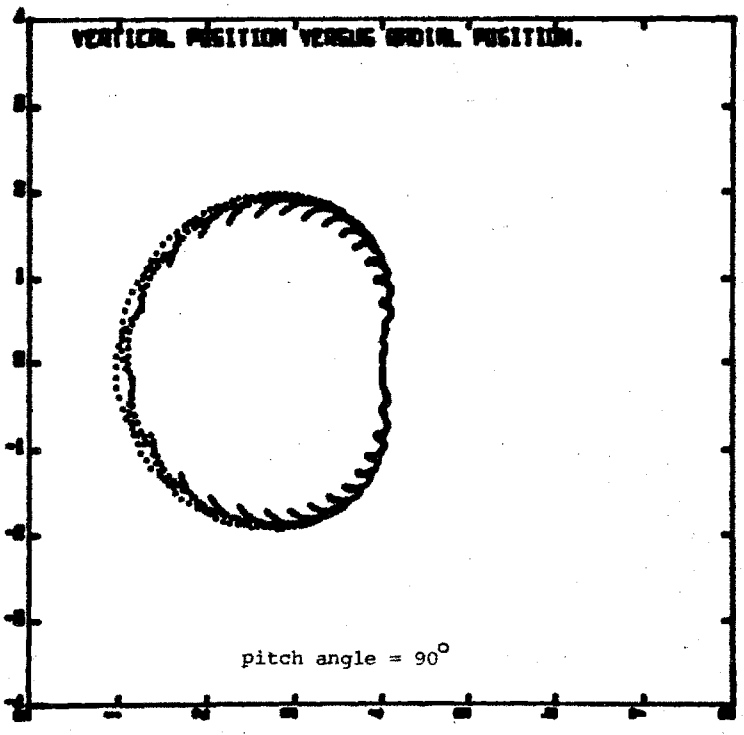
VERTICAL POSITION VERSUS RADIAL POSITION.
pitch angle = 90°

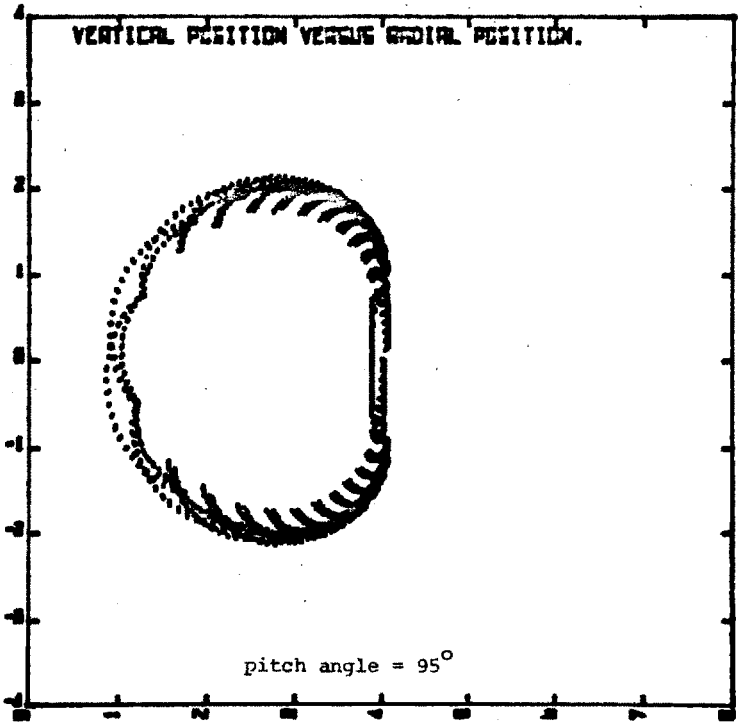
VERTICAL POSITION VERSUS RADIAL POSITION.
pitch angle = 95°

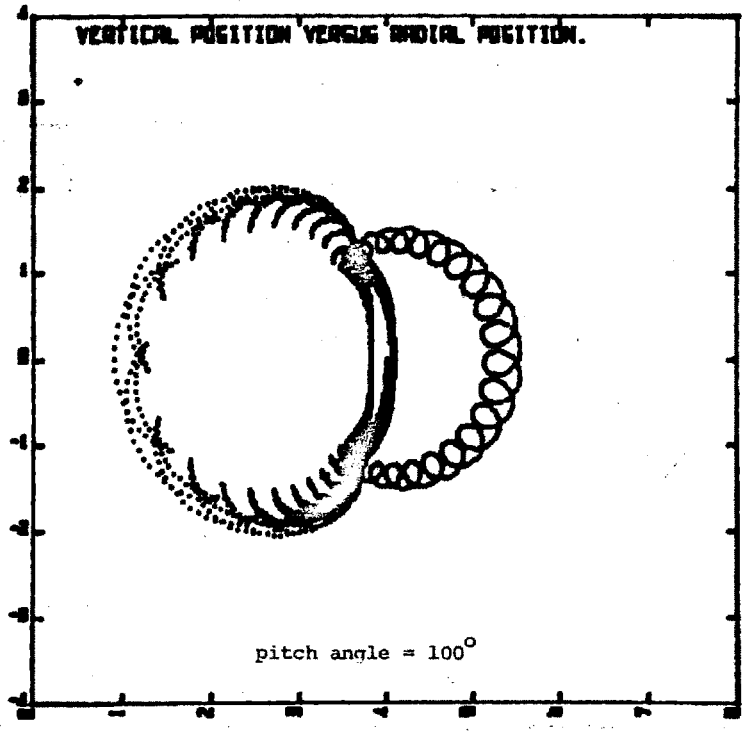
VERTICAL POSITION VERSUS RADIAL POSITION.
pitch angle = 100°

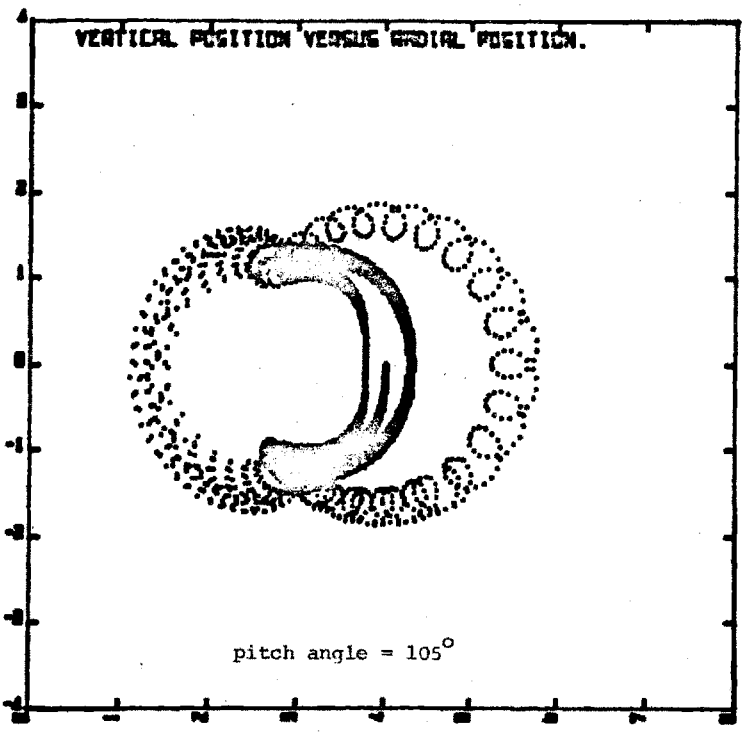
VERTICAL POSITION VERSUS RADIAL POSITION.
pitch angle = 105°

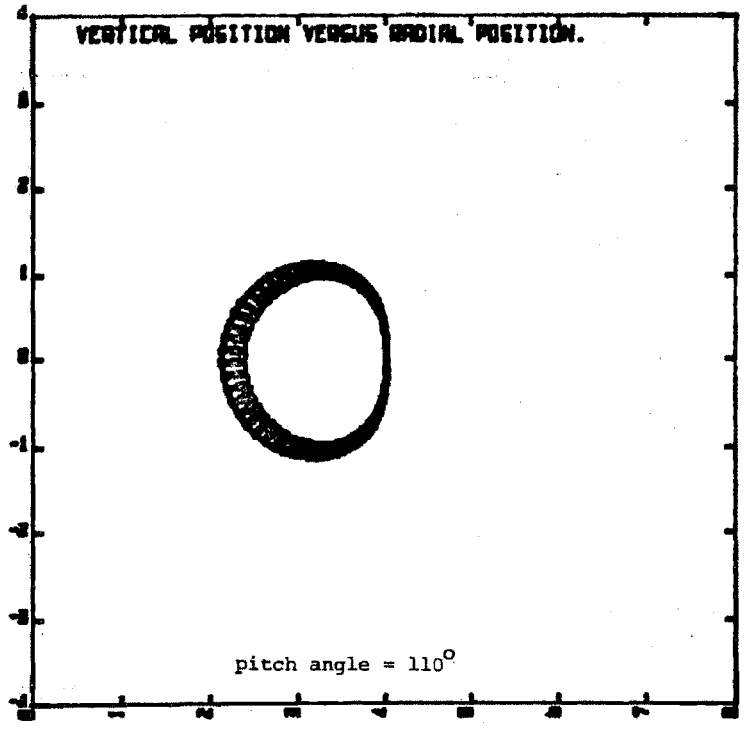
VERTICAL POSITION VERSUS RADIAL POSITION.
pitch angle = 110°

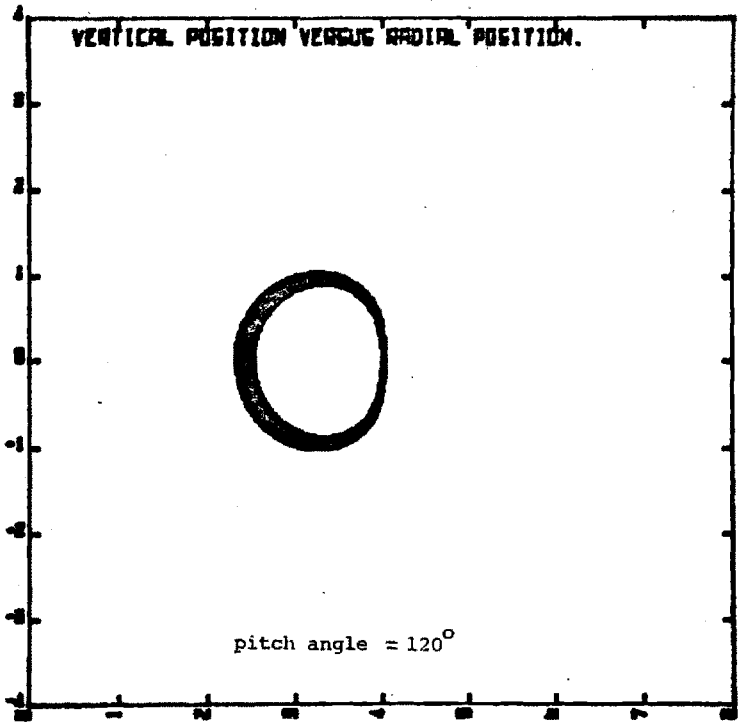
VERTICAL POSITION VERSUS RADIAL POSITION.
pitch angle = 120°

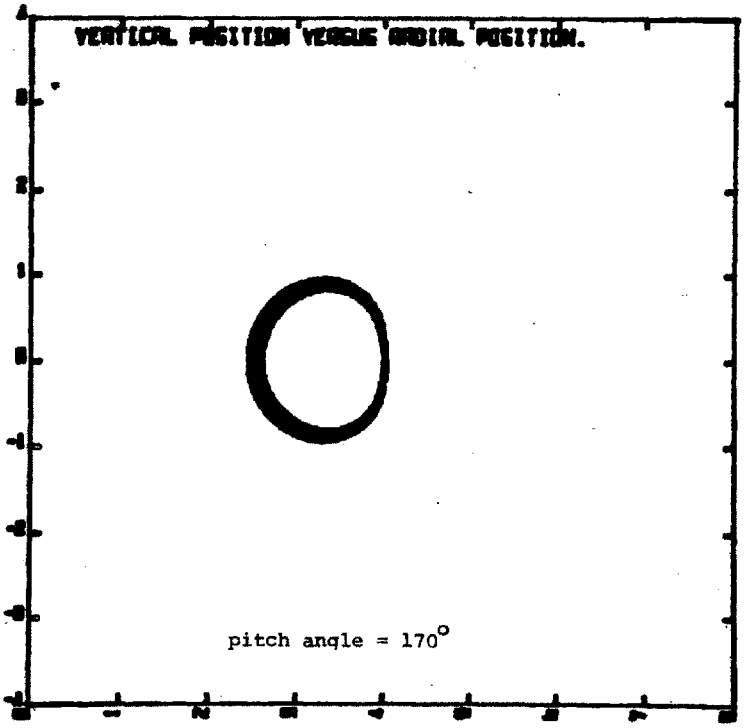
VERTICAL POSITION VERSUS RADIAL POSITION.
pitch angle = 170°

this study (having a right-handed helicity), the co-streaming particles will make counterclockwise poloidal orbits, while counter-streaming particles will make clockwise poloidal orbits. It was found that drift surface positions are fairly independent of the initial pitch angles of well circulating particles, and that the drift surfaces enlarge when circulating particles are launched near bounce regions. This effect is attributed to the barely-circulating particles having less $V_{\parallel}$ than the well circulating particles. Thus the poloidal orbit time, scaling as $1/V_{\parallel}$, is longer for barely circulating particles, and the curvature drifts thus have a longer time to accumulate their effect. It is these drifts which cause the flux-surface excursions of the particles, and greater flux-surface excursions result in larger drift surfaces.

The motion of the trapped particles is more complex and non-periodic than the well circulating particles, and is dependent on the pitch angle position of the particles and the structure (rotational transform and shear) of the vacuum magnetic field. Generally, particles with insufficient $V_{\parallel}$ to circulate freely become trapped in the helical ripples on the inside of the torsatron, where the magnetic field is relatively large.[8] Most of these trapped particles precess along the helical grooves in MOD B, following the pitch of the torsatron's helical conductors. As a helical groove passes the outer side of the torsatron,

the decreased magnetic field there no longer reflects the particle, and the particle begins to circulate toroidally. Eventually the rotational transform of the field lines moves the particle back to the inside of the torsatron, where it again becomes trapped, generally in a different helical ripple. The longitudinal motion of these particles is therefore non-periodic, and a simple longitudinal invariant for this motion does not exist.[9] In addition, Figure II-C-4 shows that the motion of the blocked particles depends on the phase of the bounce motion near the transition points. When a particle is reflected by a helical ripple, it can either become temporarily trapped in the ripple, or retrace the path it made before reflection and leave the reflection region. In the latter case, the orbit resembles the classical tokamak banana orbit. Whether a particle will become ripple-trapped or be reflected from the ripple is determined by the structure of the magnetic field and the curvature drift of the particle. Generally, it was observed that deeply-trapped particles (those launched with $V_{\parallel} \cong 0$) tended to remain trapped in helical wells, with short spans of quasi-circulating motion as the particles moved from one ripple to another (see Figure II-C-10). Particles launched nearer circulating regions in velocity space tended to exhibit both ripple trapping and tokamak banana motion (see Figure II-C-9). These different types of motion are caused by the different positions of forbidden space for deeply trapped and barely trapped

particles. The helical ripples on the outside edge of a torsatron can reflect deeply trapped particles, and often the helical groove in MOD B is the only path available to these particles. Barely trapped particles, on the other hand, can pass through the weak ripples on the outside edge and are only reflected by the stronger ripples on the inside edge of the torus. After reflecting, a barely trapped particle can, except for the grad B drift motion, retrace its path along the field lines and leave the reflection region. The orbit resembles a tokamak banana orbit (see Figure II-C-8).

One attribute of the trapped particle motion is that the phase of the bounce motion within the helical ripple varies from one trapping to the next. The exact location a particle will successively enter a ripple varies by a distance comparable to the drift displacement during one module transit. This "phase" determines the position at which the particle will leave the ripple. The "randomness" of the phase causes a particle to vary its drift positions from one poloidal orbit to the next, and the drift "surfaces" of these particles are actually three-dimensional drift "regions" (see Figure II-C-9).

As discussed in part B of this chapter, the addition of an electric field adds an $\underline{E} \times \underline{B}$ drift to the guiding-center motion. In order to observe the effect of this drift, a voltage profile of the form:

$$V(\psi_t) = V_{axis}\left(1 - \frac{\psi_t}{\psi_{sep}}\right)^{.4}$$

was arbitrarily chosen, and a scan through V_{axis} space was made on a deeply-trapped and well circulating orbit of a 3.5 MeV alpha particle. The results are shown in Figures II-C-5 and II-C-6. The orbit of the well circulating particle was insensitive to the voltage profile, even for an axis voltage of 1 MV. This is consistent with the earlier observation that the drift surface position of well circulating particles is very insensitive to particle energy. As the particle orbited from the axis region to the lower voltage region near the inside edge of the torsatron, it gained about 100 kV of parallel energy, but this did not affect the drift surface position by a noticable amount. On the other hand, voltage changes on the order of 10 kV influenced the orbits of deeply-trapped particles. As a particle moves from a high voltage region to a lower voltage one, the gain in kinetic energy results in an increase in $V_{\parallel}$ through the energy conservation equation (see equation II-B-3). The increased parallel velocity tends to decrease the effect of the grad B drifts on the particle, resulting in a decreased flux excursion of the particle, and a correspondingly smaller drift surface. The opposite effect is seen on positively charged particles when a negative axis voltage is implemented. In this case the particle's parallel energy decreases as it climbs the potential hill between the axis and separatrix regions. The lack of

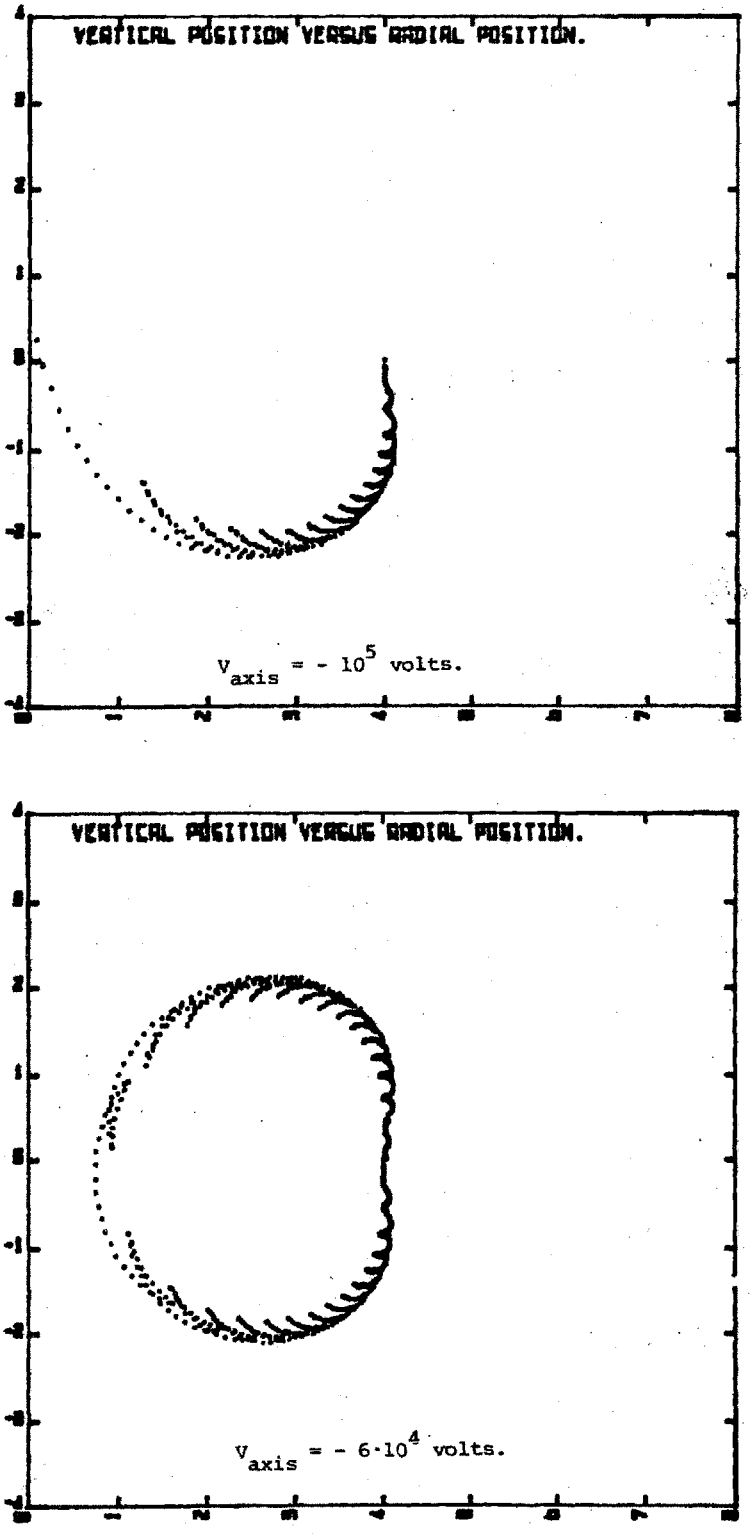

Figure II-C-5. Deeply trapped orbit for different voltage regimes.

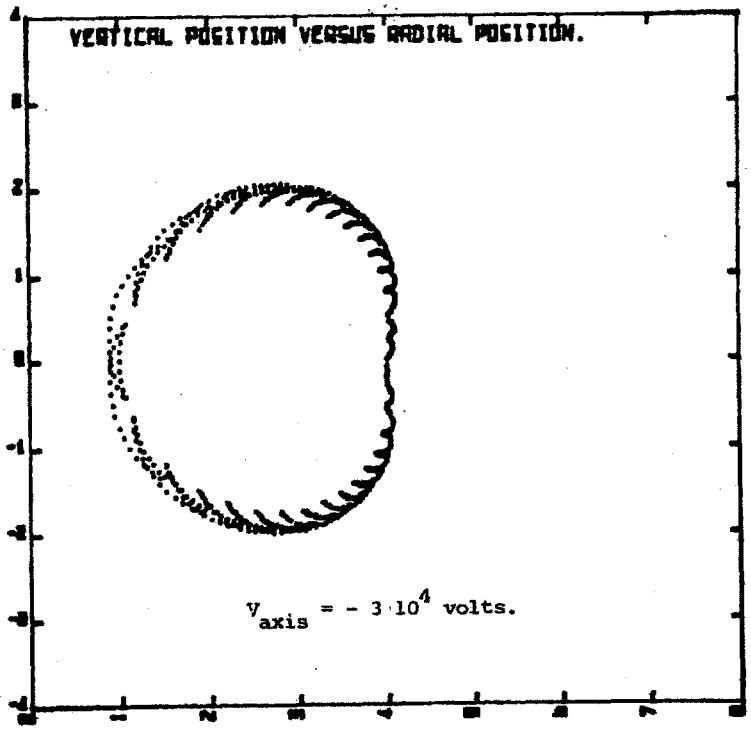
VERTICAL POSITION VERSUS RADIAL POSITION.
$V_{axis} = -3\,10^4$ volts.

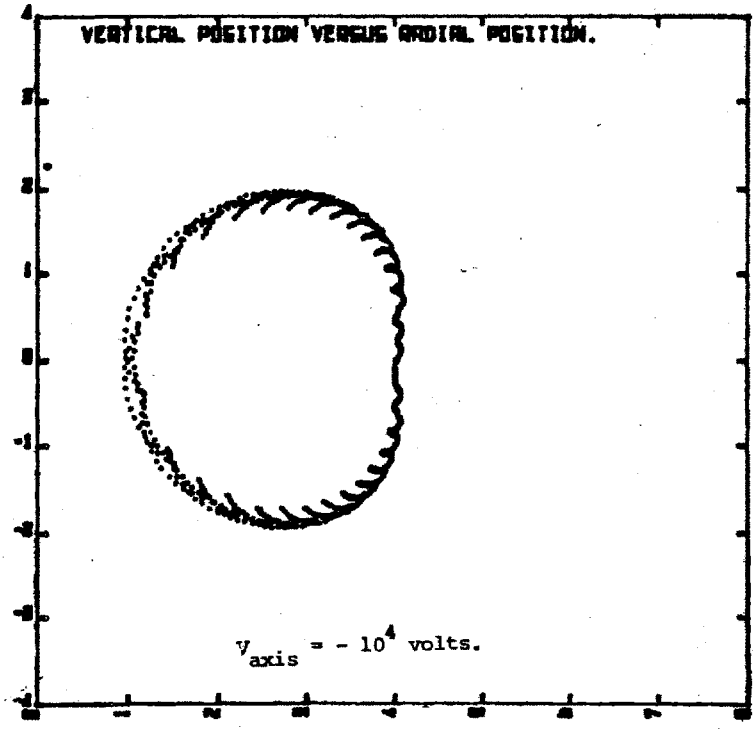
VERTICAL POSITION VERSUS RADIAL POSITION.
$V_{axis} = -10^4$ volts.

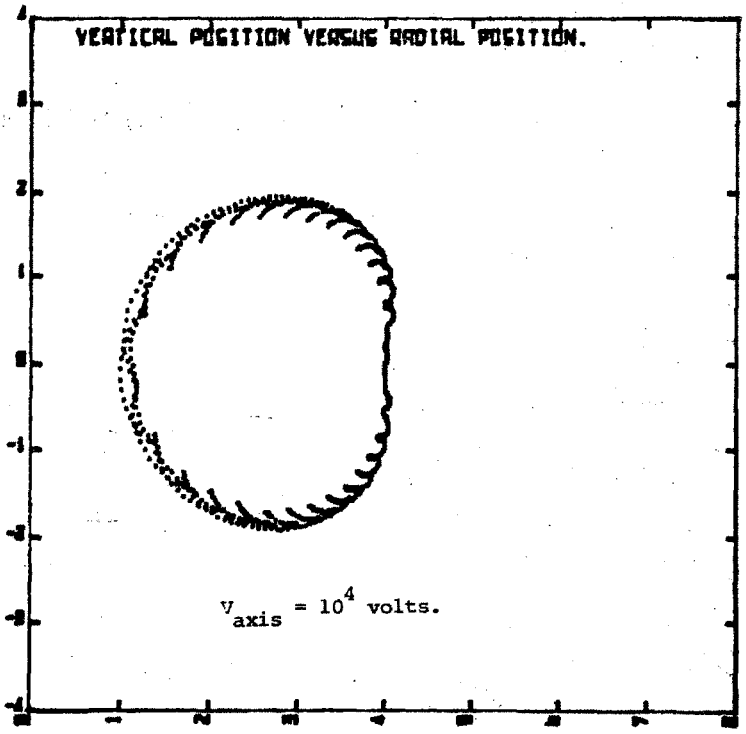
VERTICAL POSITION VERSUS RADIAL POSITION.
$V_{axis} = 10^4$ volts.

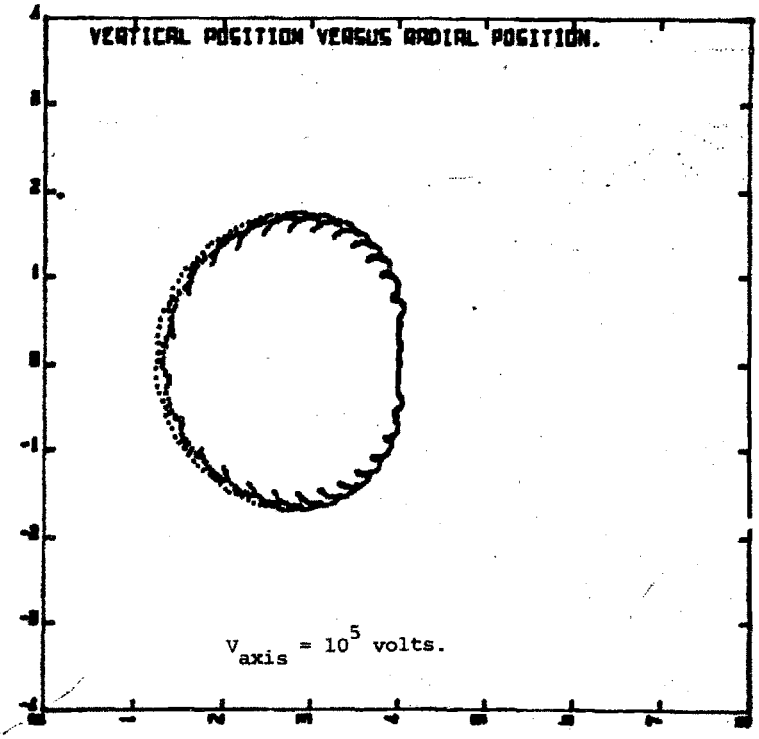
VERTICAL POSITION VERSUS RADIAL POSITION.
$V_{axis} = 10^5$ volts.

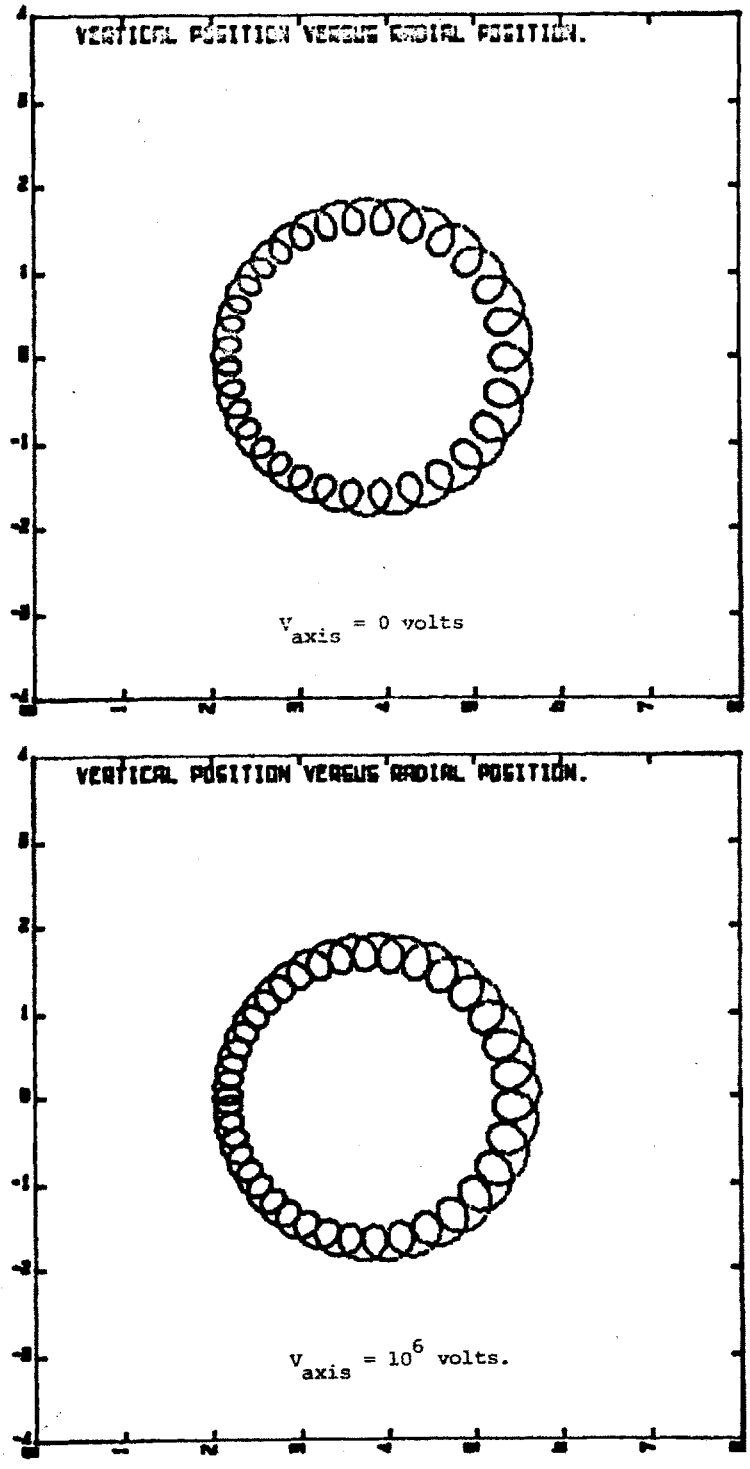

Figure II-C-8 Well circulating orbit for different voltage regimes.

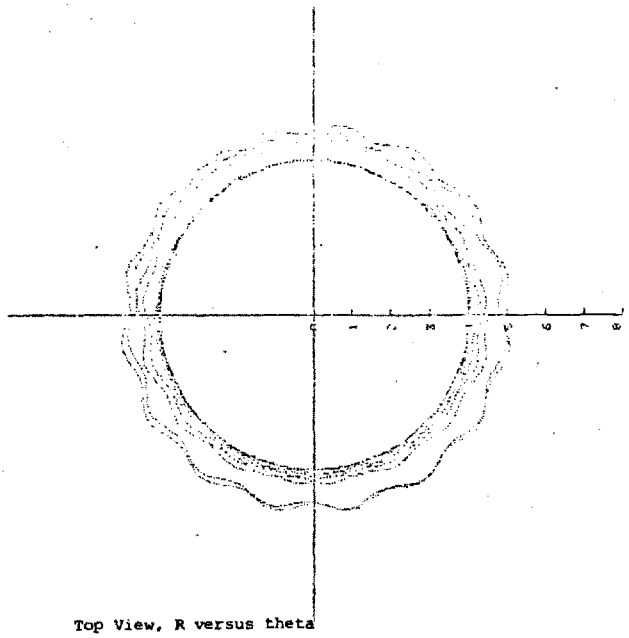

Top View, R versus theta

origin of graph is major radius minus minor radius position.

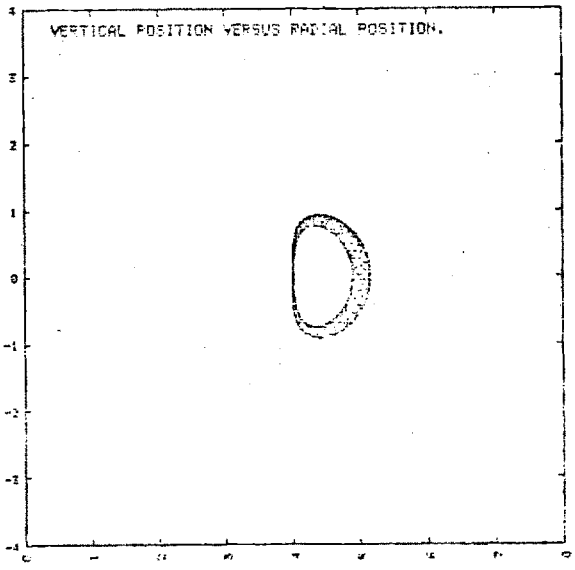

Detailed scans for well-circulating particle

Figures II-C-7

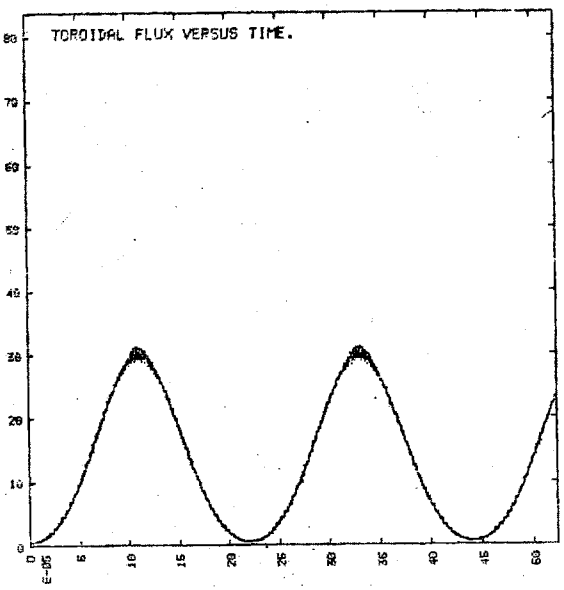
TOROIDAL FLUX VERSUS TIME.

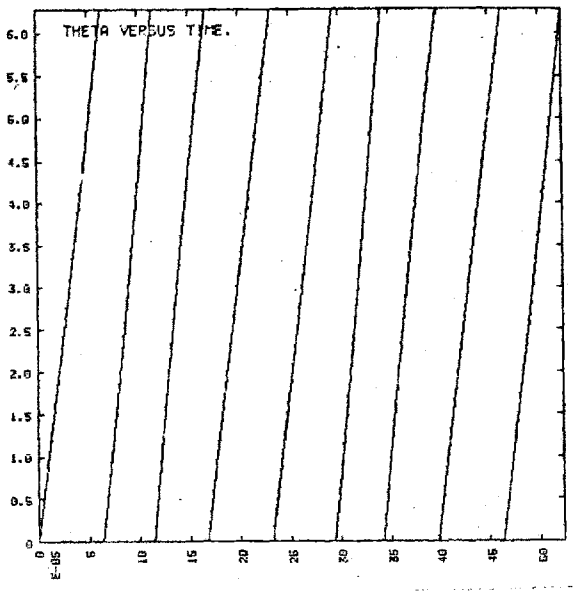
THETA VERSUS TIME.

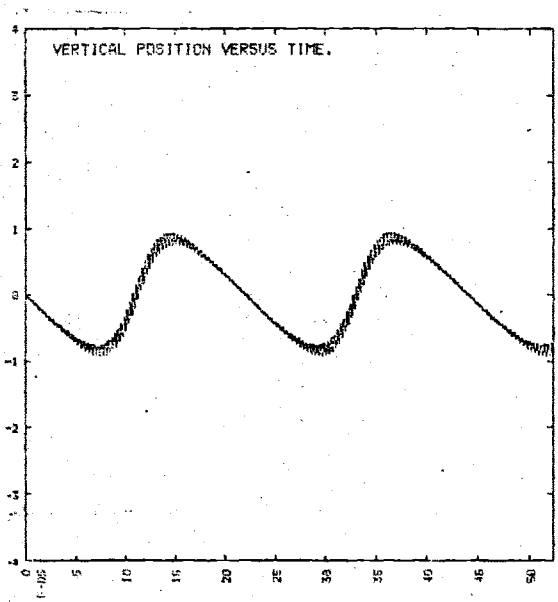
VERTICAL POSITION VERSUS TIME.

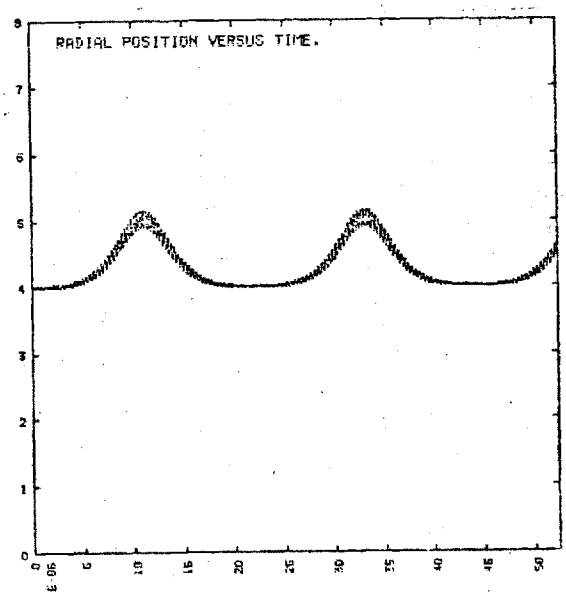
RADIAL POSITION VERSUS TIME.

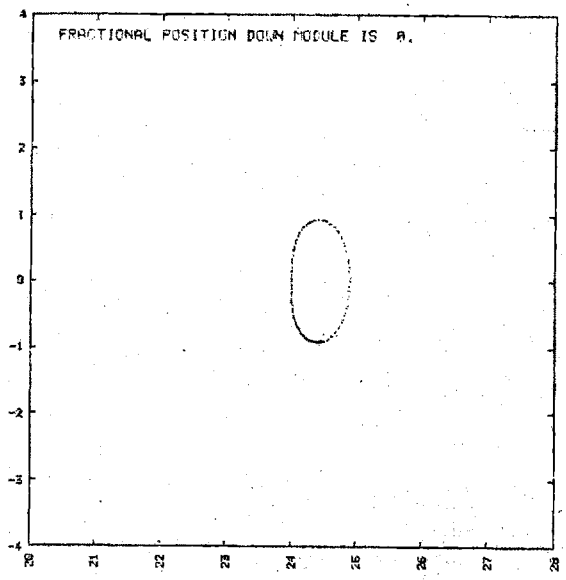
FRACTIONAL POSITION DOWN MODULE IS 0.

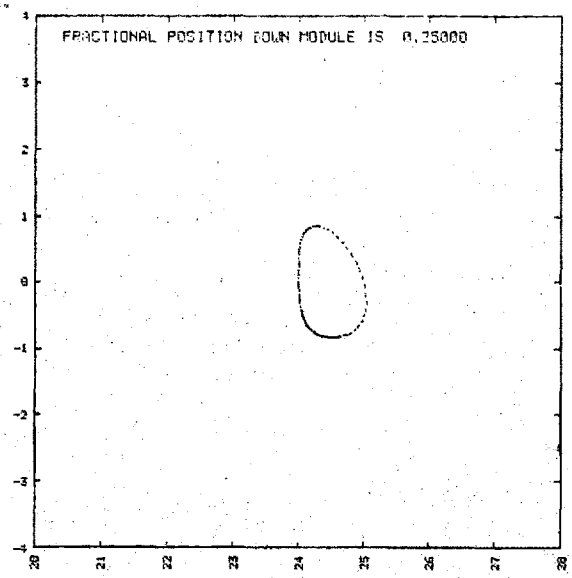
FRACTIONAL POSITION DOWN MODULE IS 0.25000

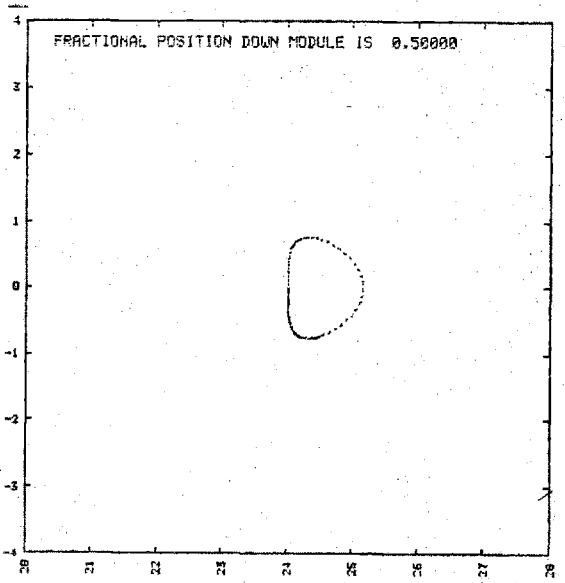
FRACTIONAL POSITION DOWN MODULE IS 0.50000

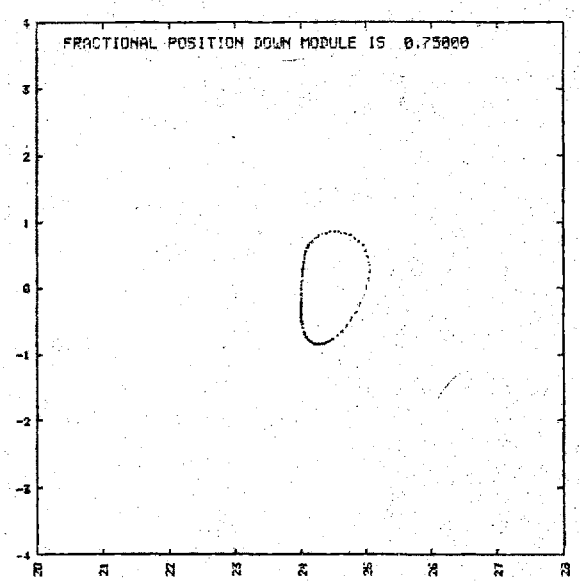
FRACTIONAL POSITION DOWN MODULE IS 0.75000

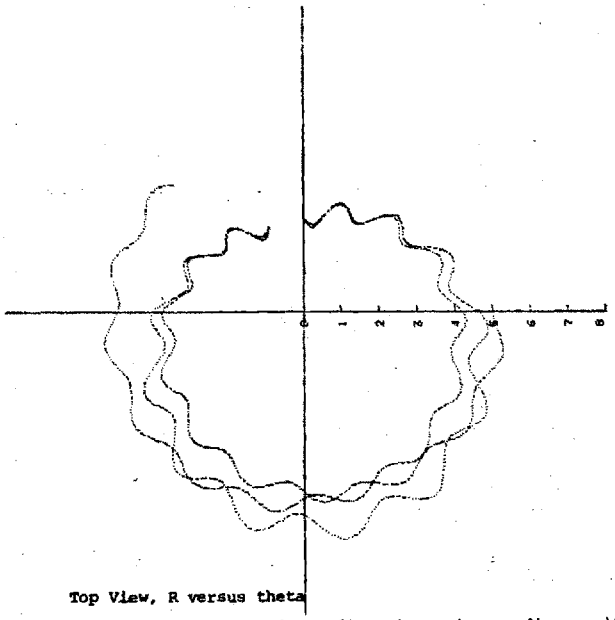

Top View, R versus theta
origin of graph is major radius minus minor radius position.

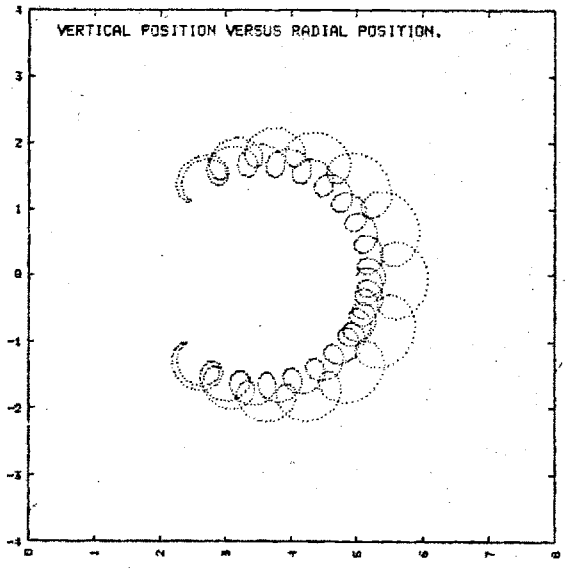

Detailed scans for barely-trapped particle

Figures II-C-5

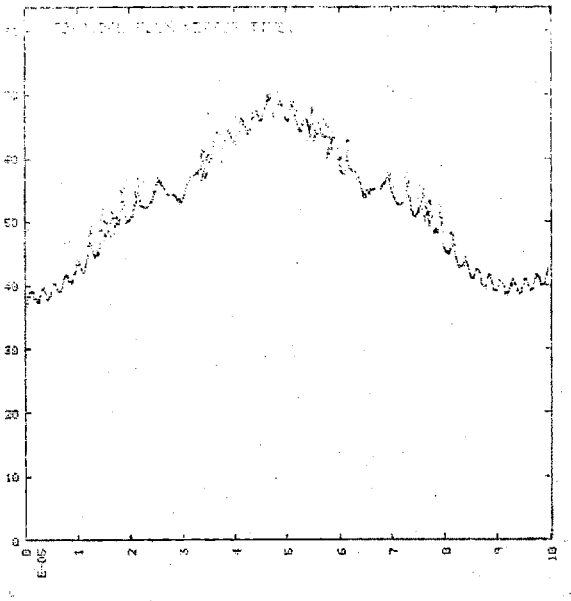

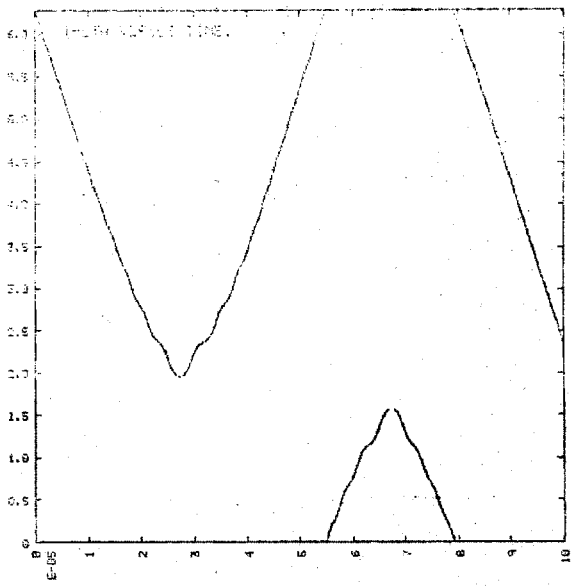

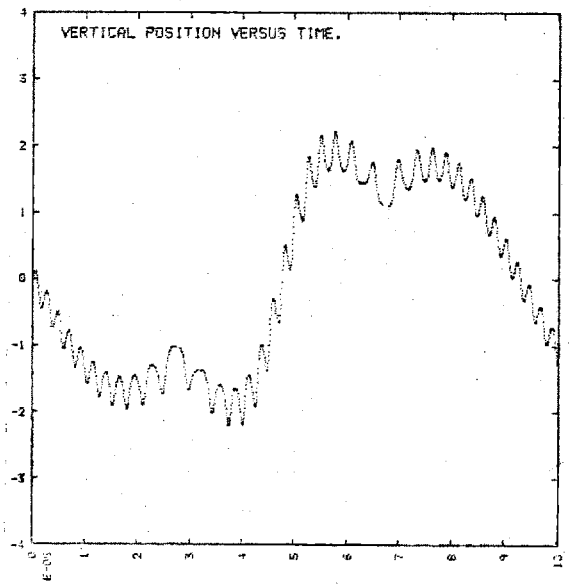
VERTICAL POSITION VERSUS TIME.

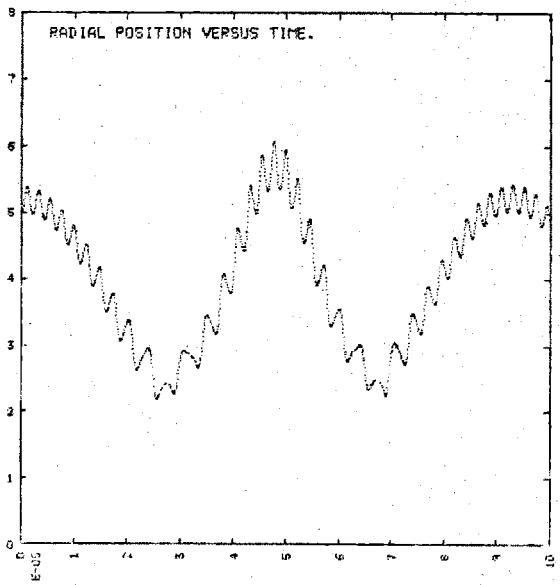
RADIAL POSITION VERSUS TIME.

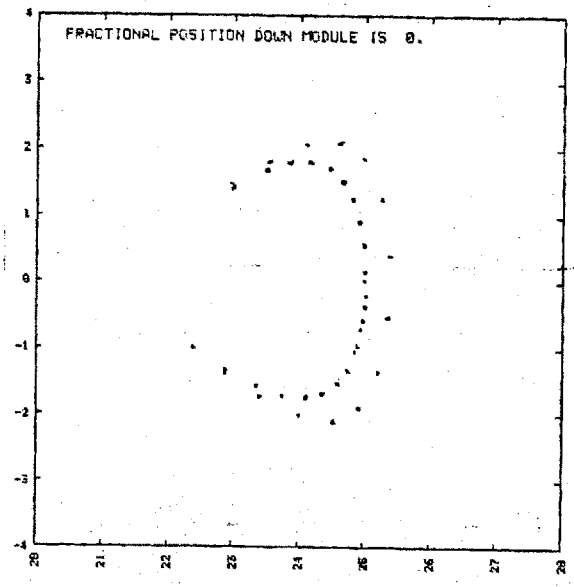
FRACTIONAL POSITION DOWN MODULE IS 0.

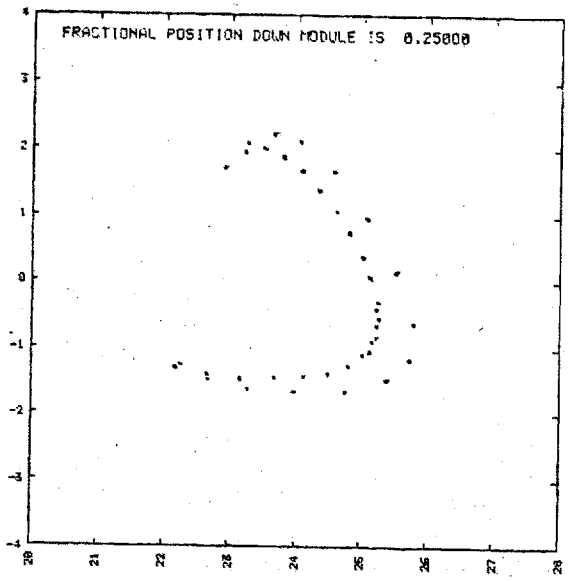
FRACTIONAL POSITION DOWN MODULE IS 0.25000

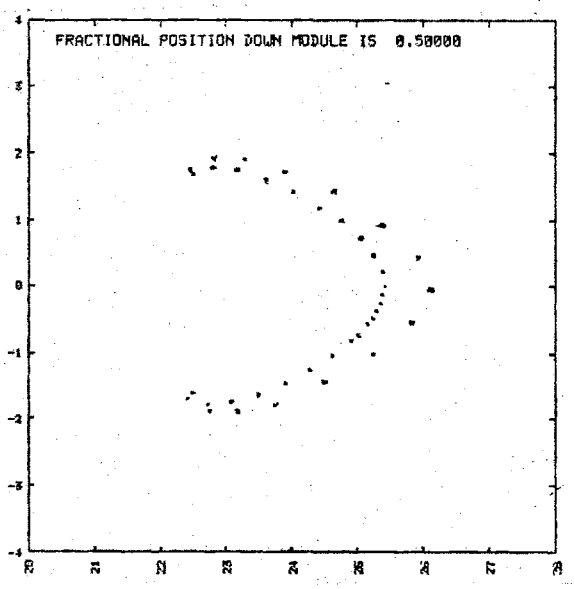
FRACTIONAL POSITION DOWN MODULE IS 0.50000

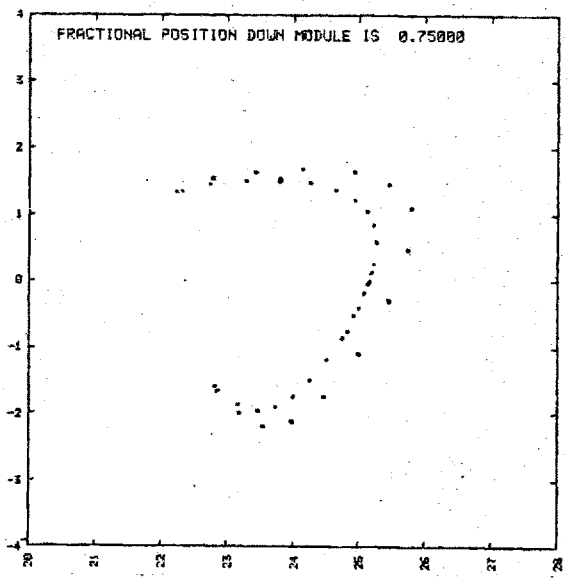
FRACTIONAL POSITION DOWN MODULE IS 0.75000

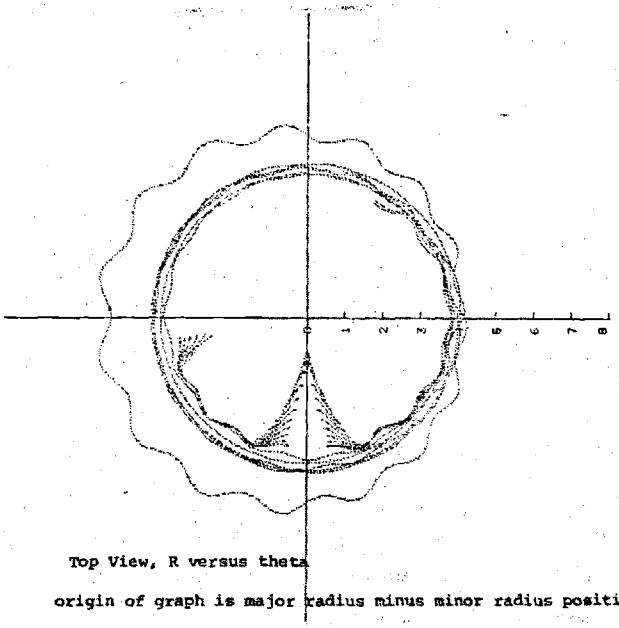

Top View, R versus theta

origin of graph is major radius minus minor radius position.

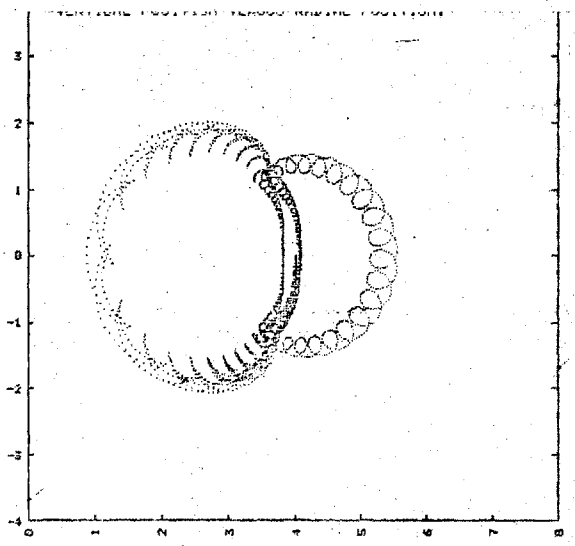

Detailed scans for moderately-trapped particle

Figures II-C-9

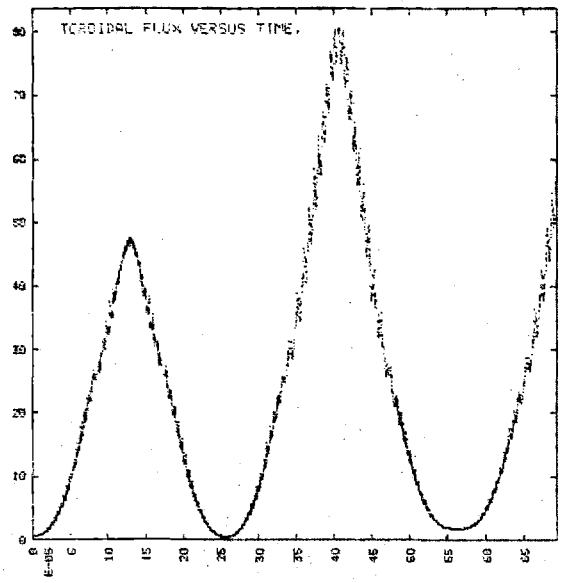
TOROIDAL FLUX VERSUS TIME.

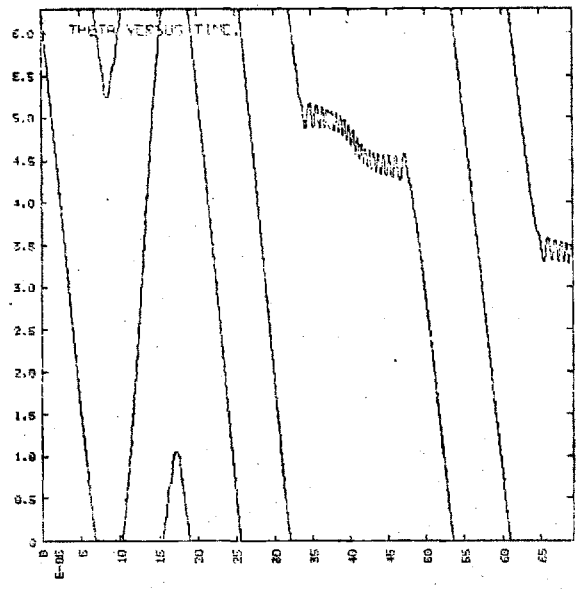
THETA VERSUS TIME.

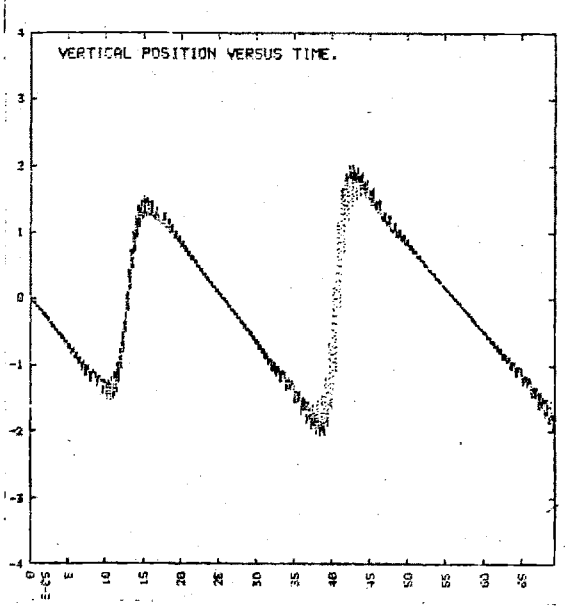
VERTICAL POSITION VERSUS TIME.

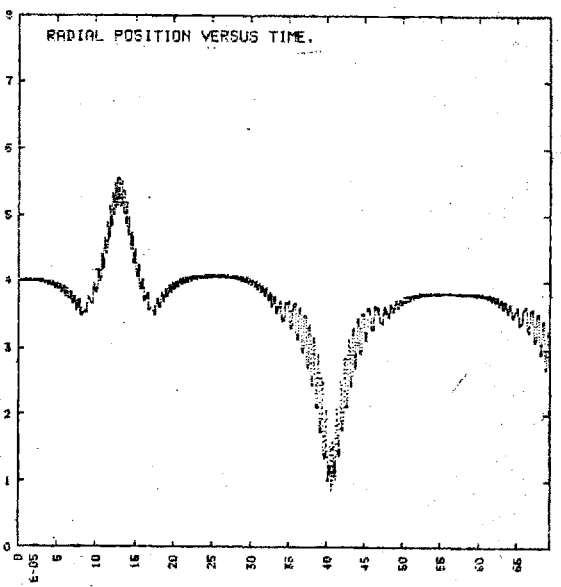
RADIAL POSITION VERSUS TIME.

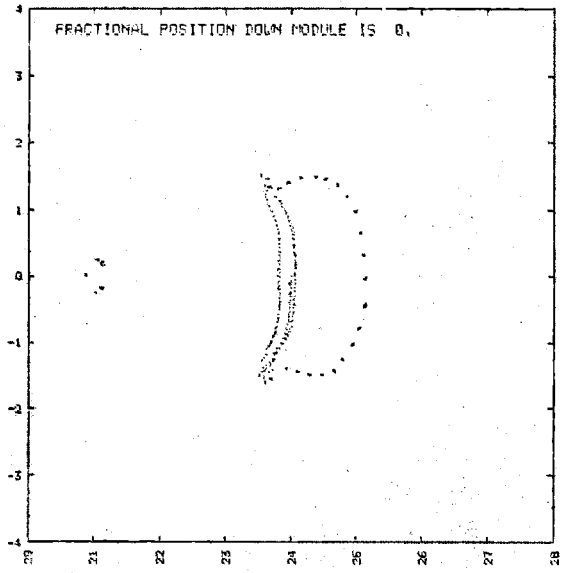
FRACTIONAL POSITION DOWN MODULE IS 0.

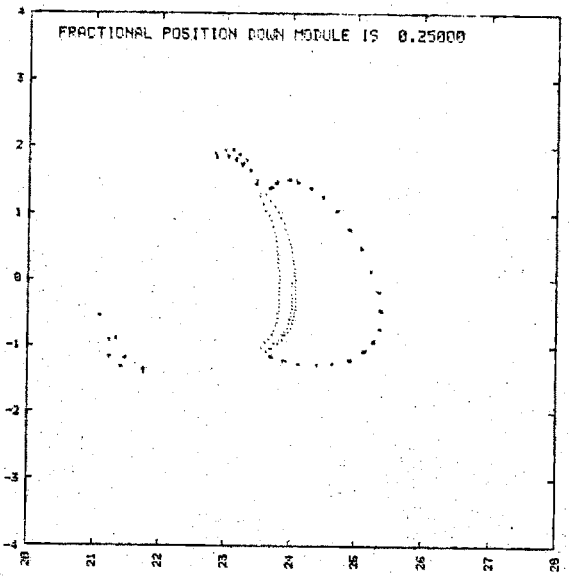
FRACTIONAL POSITION DOWN MODULE IS 0.25000

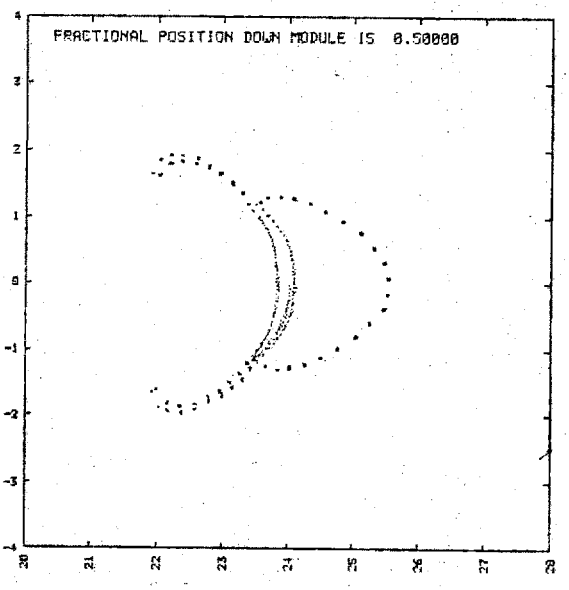
FRACTIONAL POSITION DOWN MODULE IS 0.50000

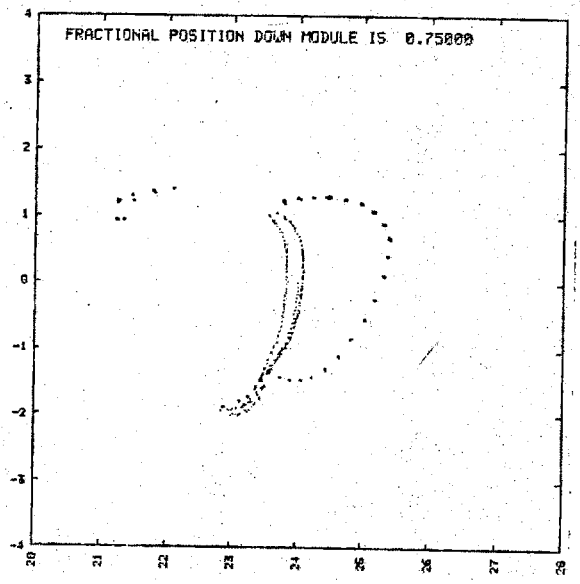
FRACTIONAL POSITION DOWN MODULE IS 0.75000

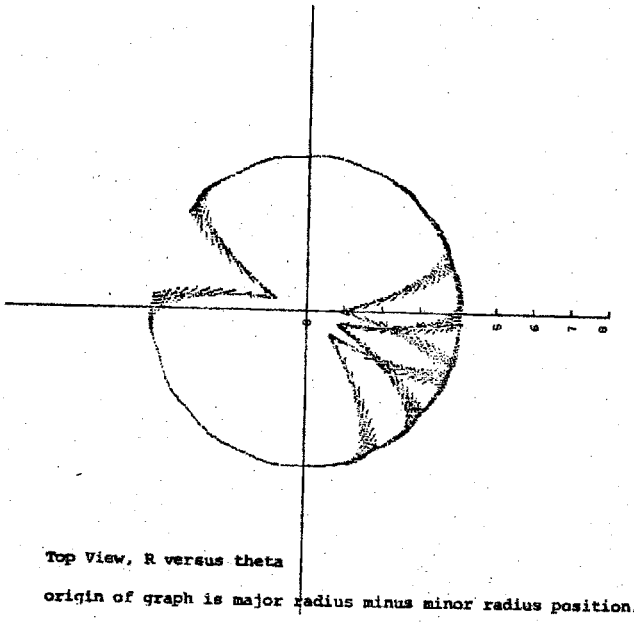

Top View, R versus theta

origin of graph is major radius minus minor radius position.

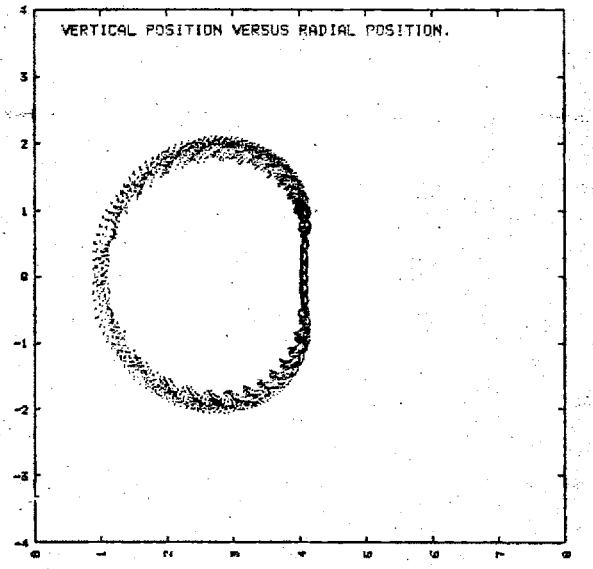

Detailed scans for deeply-trapped particle

Figures II-C-10

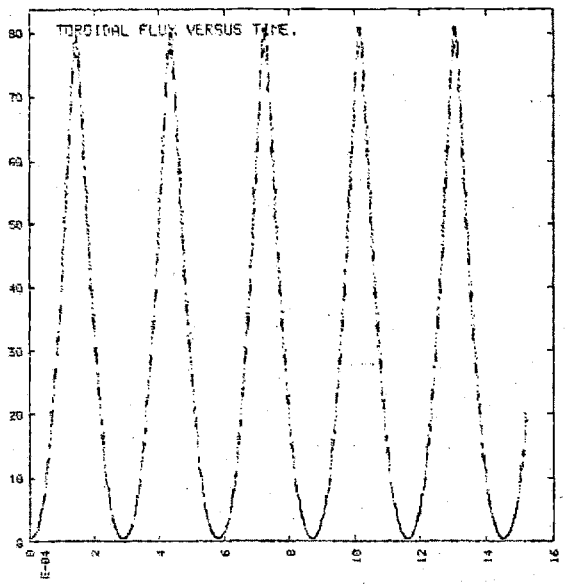
TOROIDAL FLUX VERSUS TIME.
E-04

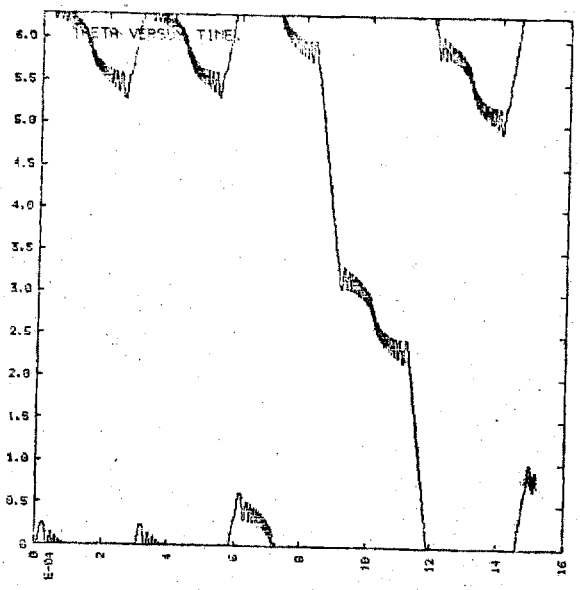
BETA VERSUS TIME.
E-04

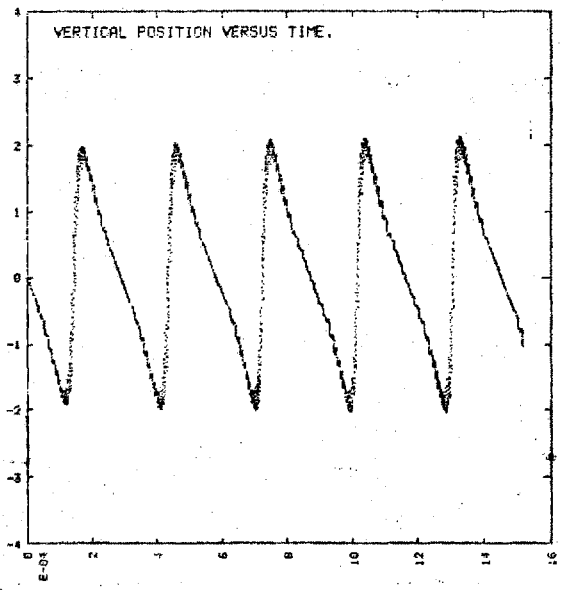
VERTICAL POSITION VERSUS TIME.
E-04

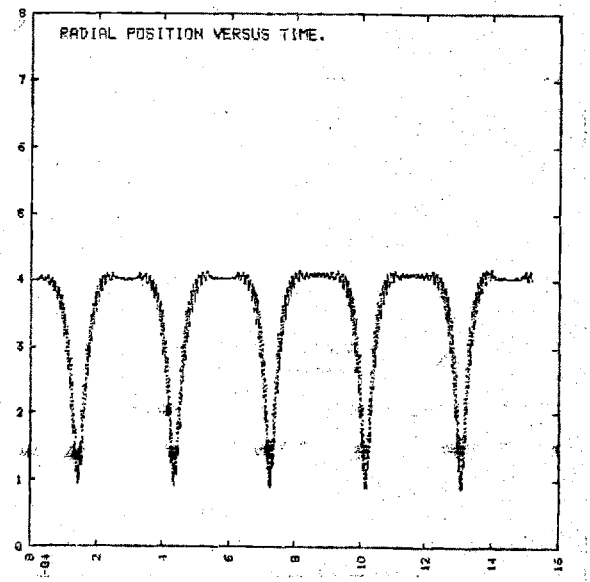
RADIAL POSITION VERSUS TIME.
E-04

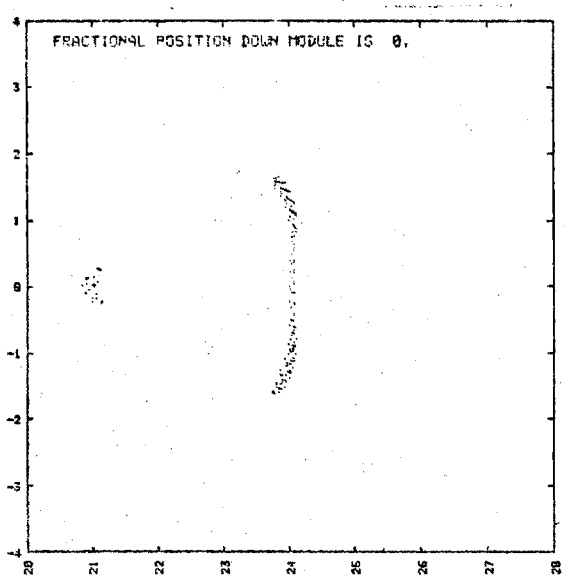
FRACTIONAL POSITION DOWN MODULE IS 0.

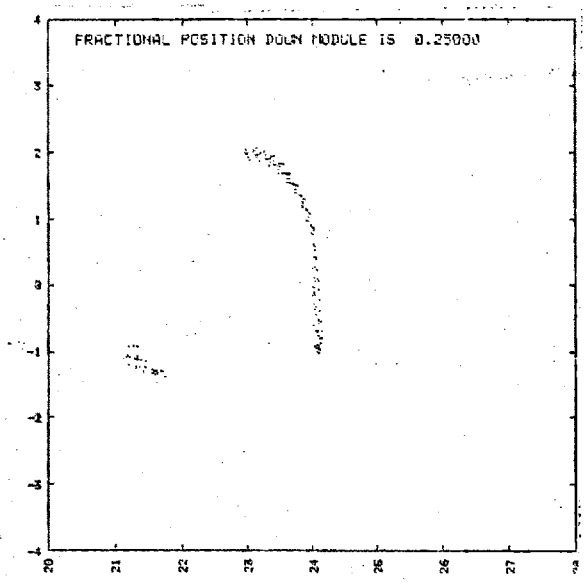
FRACTIONAL POSITION DOWN MODULE IS 0.25000

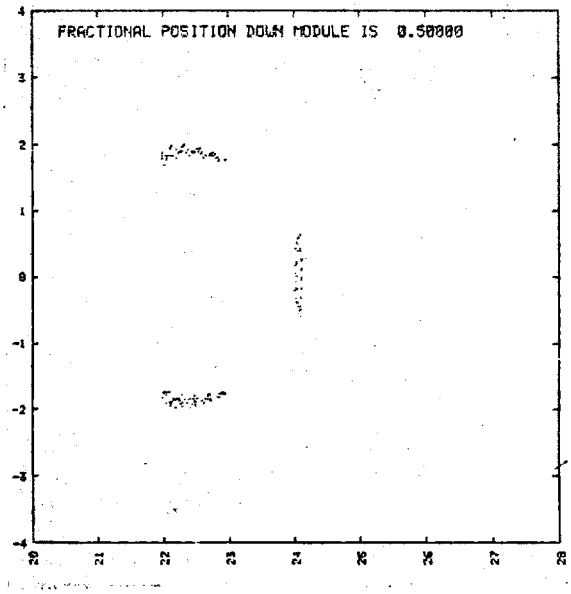
FRACTIONAL POSITION DOWN MODULE IS 0.50000

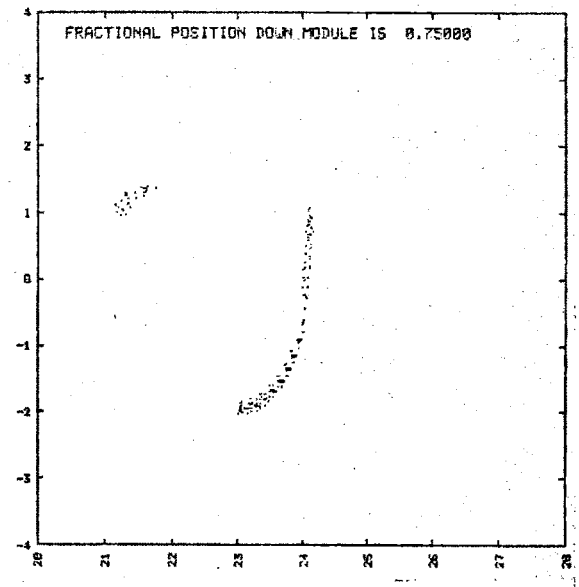
FRACTIONAL POSITION DOWN MODULE IS 0.75000

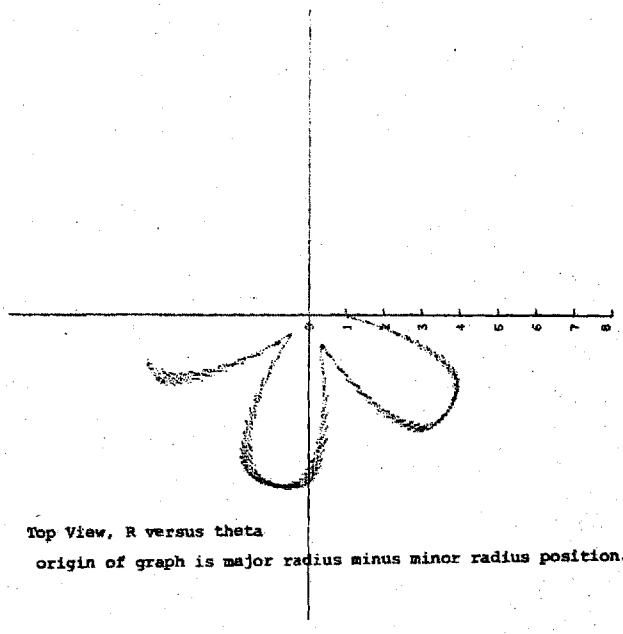

Top View, R versus theta
origin of graph is major radius minus minor radius position.

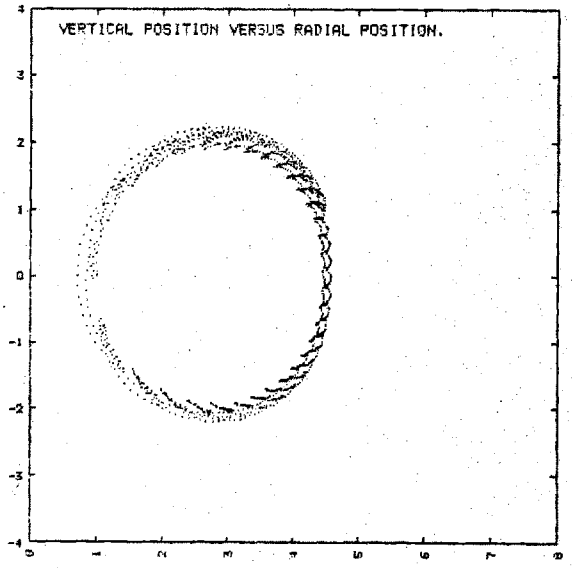

Detailed scans of particle permanently trapped in helical well.

Figures II-C-11

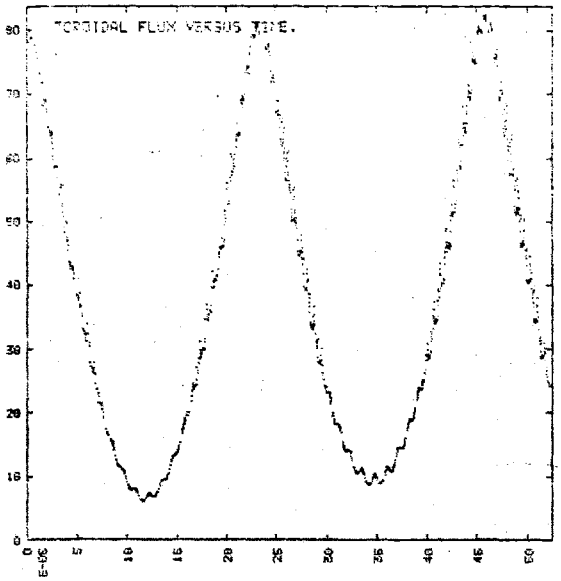
TOROIDAL FLUX VERSUS TIME.

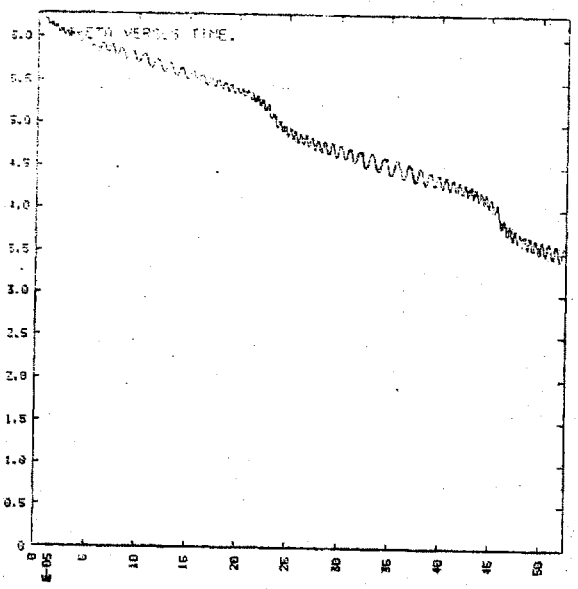

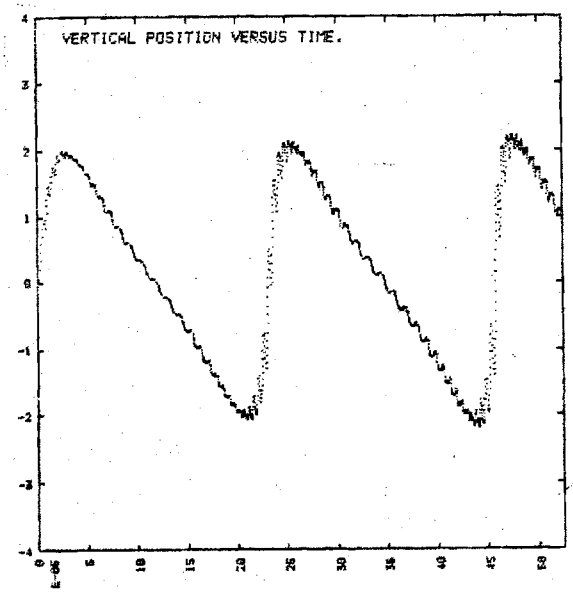
VERTICAL POSITION VERSUS TIME.

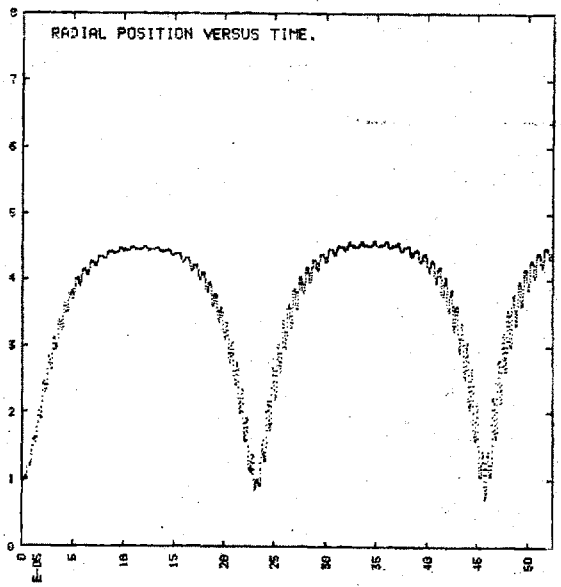
RADIAL POSITION VERSUS TIME.

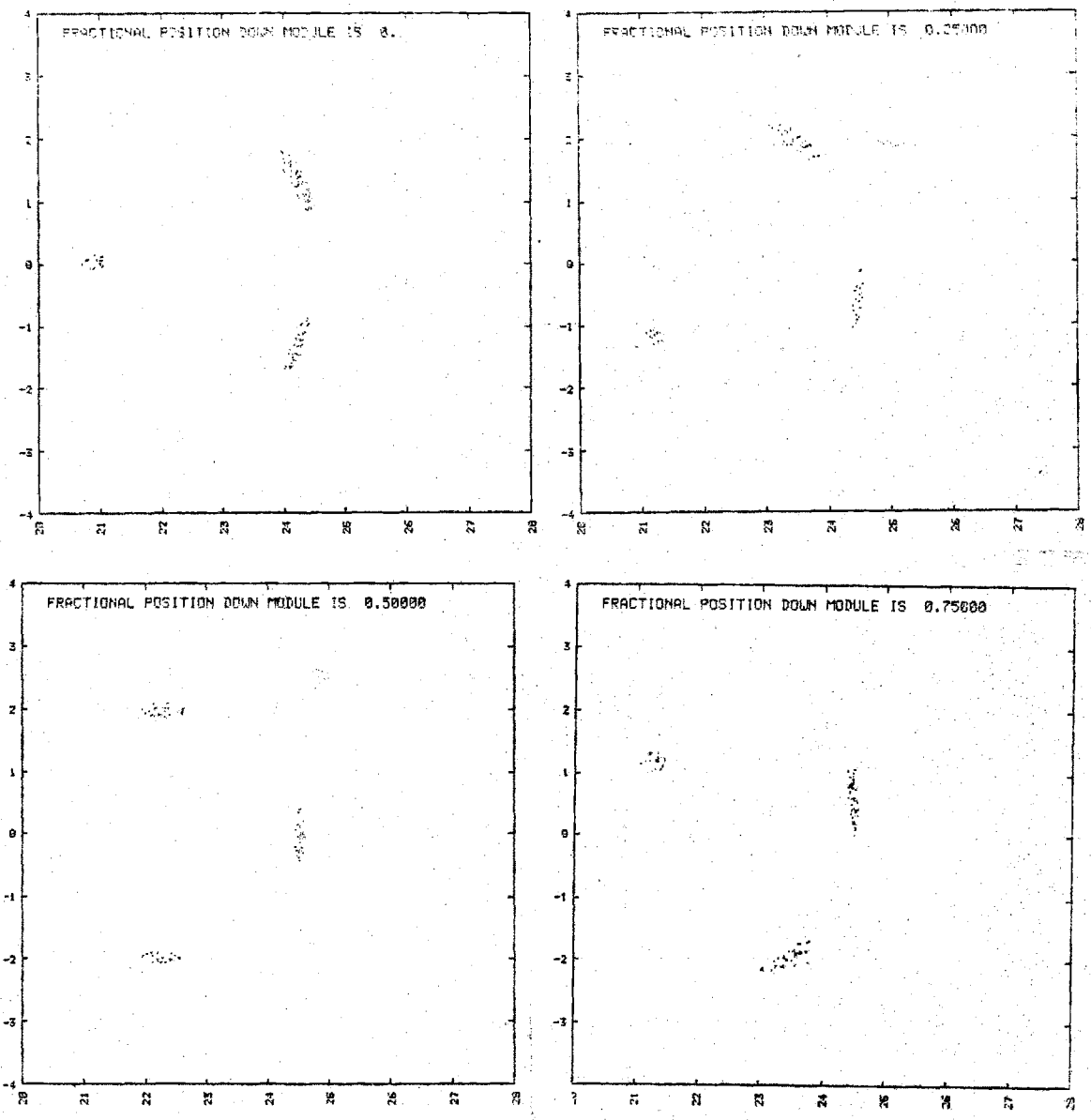
FRACTIONAL POSITION DOWN MODULE IS 0.
FRACTIONAL POSITION DOWN MODULE IS 0.25000
FRACTIONAL POSITION DOWN MODULE IS 0.50000
FRACTIONAL POSITION DOWN MODULE IS 0.75000

parallel velocity results in increased flux excursions due to the increased influence of the grad B drift. At $V_{axis} = -100$ kV, the test particle became unconfined (see Figure II-C-5). In general, potential wells near the magnetic axis tend to destabilize the orbits of deeply-trapped particles as these particles pass near the separatrix region. The effect of the voltage profile on 3.5 MeV deeply-trapped alpha particles was noticable when a potential difference of more than 10 kV was created along the particle orbit.

D. Conclusions

A highly accurate guiding-center tracking code has been developed, capable of tracking guiding-centers through thousands of poloidal orbits in helical toroidal fields without significant numerical error. The high degree of accuracy is obtained by integrating an equation of motion which is accurate to second order in μ, and by calculating $\underline{B}$ and $\underline{\nabla B}$ in the tracing code with a cubic spline interpolation routine.

The tracking code was used to investigate the confinement and orbit characteristics of charged particles in torsatron magnetic fields. An analytic investigation of particle confinement in helical, cylindrical magnetic fields showed that particles near the magnetic axis are limited to radial excursions of the order of a Larmour radius, due to the conservation of helical momentum in the particle orbit. A numerical scan of phase-space

demonstrated that this same limitation on radial excursion applied to all particles between the magnetic axis and coil position. These results are independent of the energy and pitch-angle positions of the particle, as long as $\rho_{\ell} << a_{coil}$.

The lack of a direction of symmetry inhibits an analytic investigation of the radial excursions of particles in helical toroidal fields. The analyses of confinement and orbit characteristics were done by examining guiding-center orbits obtained by the TAPIR code. The vacuum field orbits showed that the particles may be grouped into two general classes, well circulating particles and blocked particles. Particles with $V_{\parallel} \gtrsim V_{\perp}$ have sufficient parallel energy so that they are never reflected by the helical or toroidal modulations in the magnetic field. Their orbits are characterized by extremely periodic motion on well defined drift surfaces. Blocked particles, on the other hand, are reflected by the modulations in B, and generally spend part of their time in quasi-circulating orbits and other parts trapped in the helical ripples in B. Their motion is non-periodic, and the randomness of the phases of the bounce motion within a ripple results in varying particle drift positions after successive poloidal orbits. These particles' orbits are contained in three-dimensional drift "regions".

Finally, the effects of plasma voltage profiles on alpha particle orbits were investigated. It was found that

the orbits of well circulating alpha particles were very insensitive to plasma electric fields, even for a one megavolt potential difference between the magnetic axis and separatrix. The orbits of deeply-trapped alpha particles were affected by much lower potential differences, on the order of 10 kilovolts. It was found that a positive charging of the axis region aided in alpha particle confinement, since the particles, leaving the axis region, would pick up parallel energy from the decreasing potential and be less affected by the modulation of the magnetic field. Per contra, a negative charging of the axis region resulted in an increased number of unconfined orbits as particles leaving the axis region lost parallel energy due to the increased potential. This resulted in larger flux surface excursions by these particles, and in some cases, particle loss.

References, Chapter II

1) T. G. Northrop, The Adiabatic Motion of Charged Particles, John Wiley and Sons (1963).

2) A. H. Boozer, "Guiding Center Drift Equations," unpublished, Plasma Physics Laboratory, Princeton University (1979).

3) S. Chandrasekhar, Principles of Stellar Dynamics, University of Chicago Press, Chicago (1942), p. 89.

4) L. Spitzer, Jr., Physics of Fully Ionized Gases, Interscience Publishers, Inc., New York (1956), p. 78.

5) D. J. Rose and M. Clark, Jr., Plasma and Controlled Fusion, The M.I.T. Press, Cambridge (1961), p. 169.

6) D. J. Rose, "Engineering Feasibility of Controlled Fusion," J. of Nuclear Fusion, 9 (1969), p. 183, Figure 3.

7) P. A. Politzer, "Magnetic Fields in a Linear Torsatron," Torsatron Design Memo 77-1, M.I.T. Dept. of Nuclear Engineering (1977).

8) A. Gibson and J. B. Taylor, "Single Particle Motions in Toroidal Stellarator Fields," Physics of Fluids, 10 (1967), p. 2653.

9) T. G. Northrop, op. cit., p. 42.

Chapter III. ALPHA-PARTICLE DISTRIBUTIONS AND CONFINEMENT PROPERTIES

A. Motivations and Assumptions

In the previous chapter I described a set of orbit equations that was used to track particles in a torsatron magnetic field. In this chapter I describe the method by which the information contained in many α-particle orbit tracks was collected and used to find the α-particle distribution function and fractional energy confinement.

The guiding-center equations used are accurate to second order in $\langle\mu\rangle$, with

$$\langle\mu\rangle = \frac{1}{2}m\langle v_\perp^2\rangle/B_{GC} + O(\varepsilon^2) \qquad \text{[III-A-1]}$$

the time averaging done over a cyclotron period, with ε a smallness parameter scaling as ρ_ℓ/L_B and $\Delta B/B$. Since the torsatron magnetic fields are static, the criterion for conservation of $\langle\mu\rangle$ is that $(\Delta B/B)^2 \ll 1$ during one cyclotron orbit. I will now show that $\langle\mu\rangle$ is well conserved for 3.5 MeV α-particles in a torsatron reactor.

Case I: $V_\perp \gg V_{||}$

The Larmor radius of the alpha-particle is

$$\rho_\ell = 10.8 \left(\frac{5 \text{ tesla}}{B}\right) \text{ cm} \qquad \text{[III-A-2]}$$

Near the magnetic axis, the magnetic curvature is primarily

the toroidal curvature of the windings, with $B \cong B_o R_o/R$, and $L_B(\text{axis}) \cong R_o$. Near the separatrix, the helicity of the field dominates, and the curvature is of the order of the minor radius of the coils. The resulting criterion for $<\mu>$ conservation is:

$$\left(\frac{\Delta B}{B}\right)^2 \simeq \left(\frac{2\rho_\ell}{a_{coil}}\right)^2 << 1 \qquad \text{[III-A-3]}$$

For the reactors of this study, $a_{coil} = 4$ meters, $B \cong 5$ tesla, so:

$$\left(\frac{\Delta B}{B}\right)^2 = \frac{1}{343} << 1 \qquad \text{[III-A-4]}$$

Case II: $V_{\parallel} >> V_{\perp}$

A particle can experience a change in B due to the particle's longitudinal motion in rippled magnetic fields. In our cyclotron period a 3.5 MeV α-particle can move 68 cm along a field line. The maximum helical ripple observed occurred in the small aspect ratio device ($R_o/a = 3$) along the outside edge of the separatrix. The magnitude of the ripple was:

$$\text{ripple} = \frac{B_{max} - B_{min}}{B_{max} + B_{min}} = 17\% \qquad \text{[III-A-5]}$$

measured along the length of a module ($L_{module} = 9.4$ meters). Along the path length of the particle for one

cyclotron period, the observed ripple is:

$$\left(\frac{\Delta B}{B}\right)_{1 \text{ period}} = \left(\frac{\Delta B}{B}\right)_{\frac{1}{2} \text{ module}} \cdot \frac{\text{path length}}{\frac{1}{2} \text{ module length}}$$

$$\left(\frac{\Delta B}{B}\right)^2 = ((.34)(68\text{cm}/4.7\text{ m}))^2 \tilde{=} 1/413 << 1 \qquad \text{[III-A-6]}$$

It was observed that the magnetic ripple rapidly decreased one to two orders of magnitude as one moves from the separatrix to the magnetic axis. Thus $<\mu>$ should be an extremely well conserved quantity for all types of α-particle orbits in the torsatrons studied.

The background plasma parameters of temperature, density, and voltage were assumed to be functions only of the vacuum field magnetic flux coordinate. This is analogous to an ideal MHD plasma model, where $\nabla p = JxB$ is perpendicular to the flux surfaces. The displacement of the vacuum field surfaces due to plasma pressure was assumed negligible.

The profiles of density and electron temperature were chosen as conservatively flat estimates of profiles that might exist within a fusion reactor. The tracking runs were done in a high density, low temperature regime, with:

$$n_e(\text{axis}) = 3.10^{20}/\text{meter}^3$$

$$T_e(\text{axis}) = 8 \text{ keV}$$

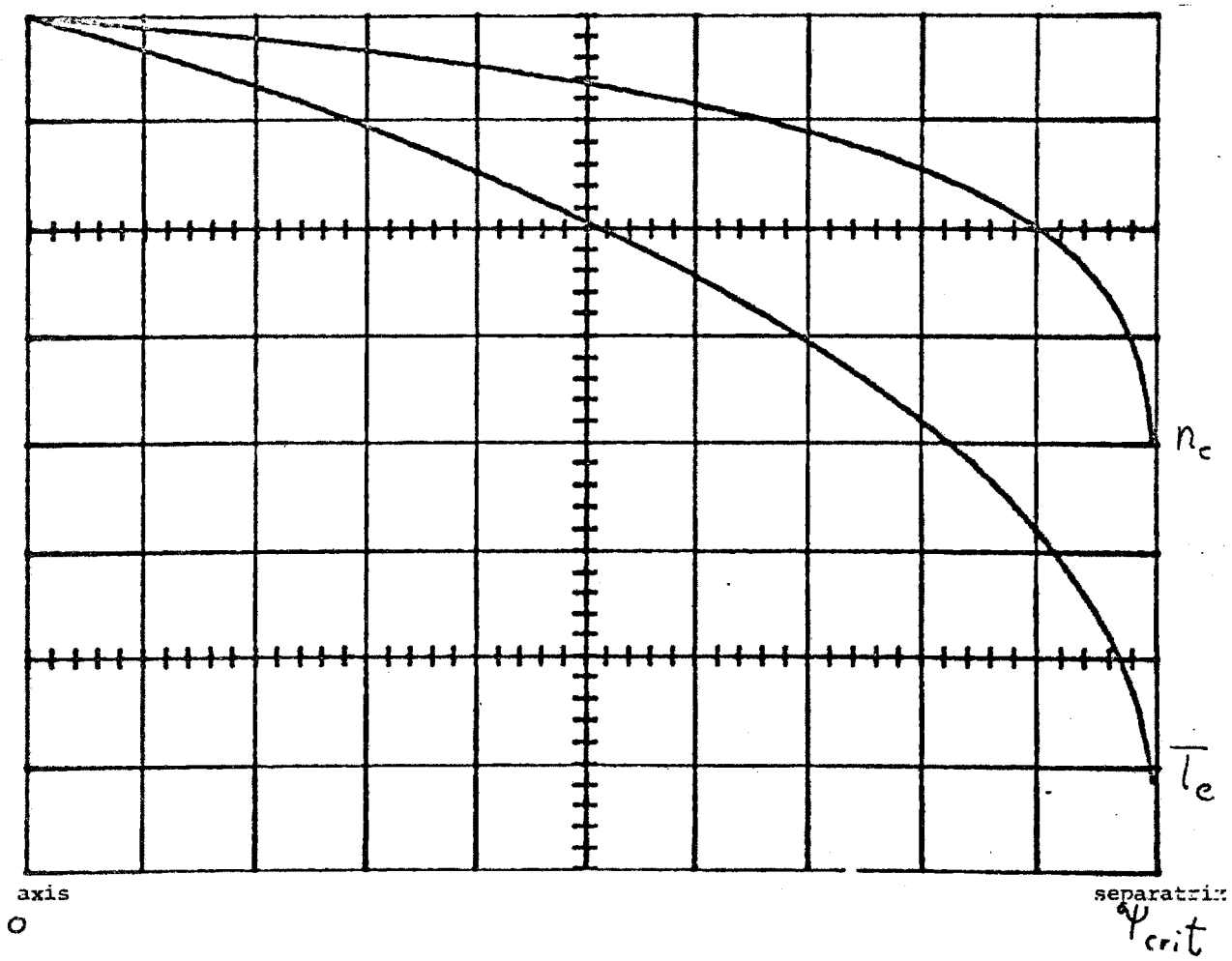

Plasma Profiles versus Toroidal Flux

Figure III-A-1

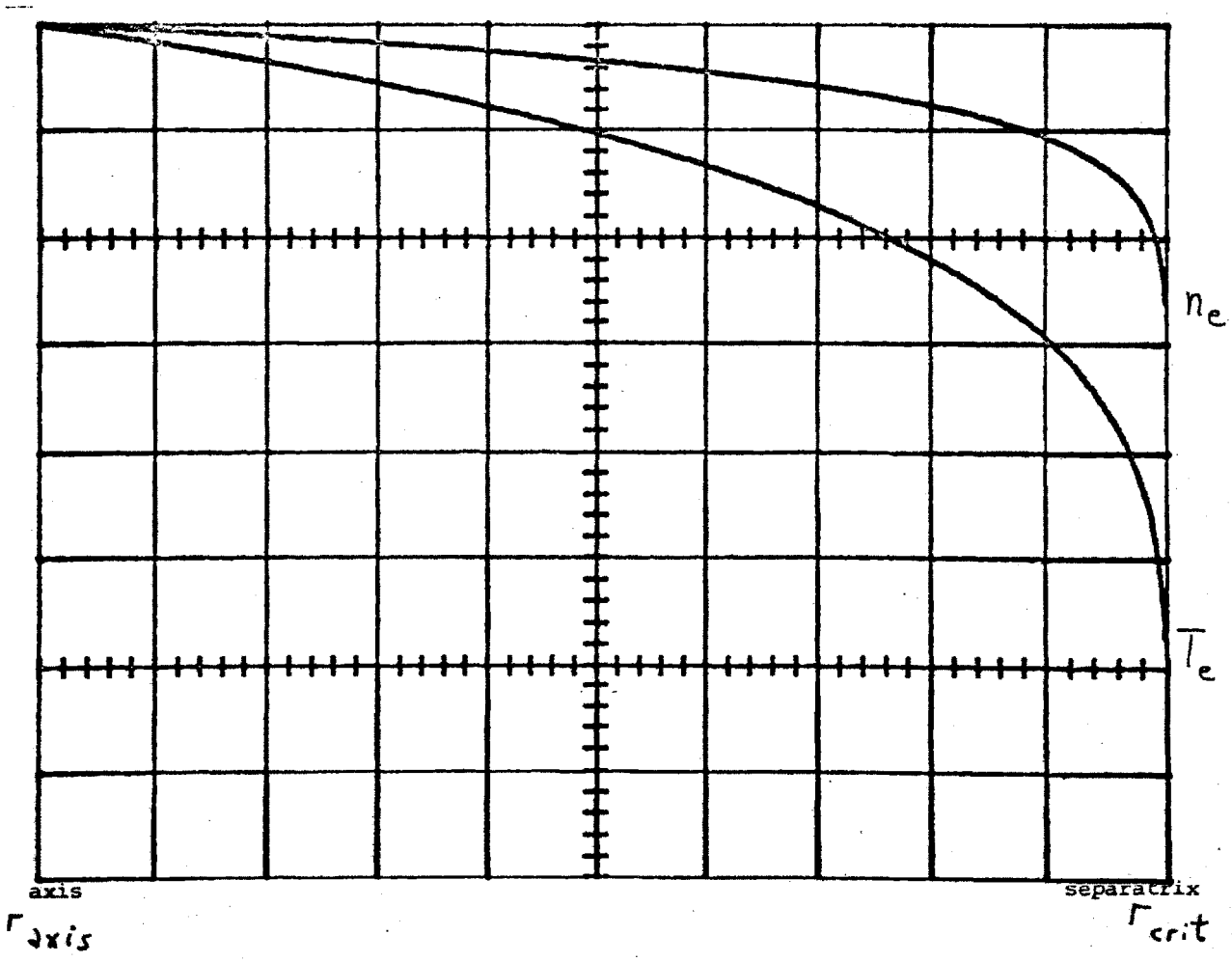

Plasma profiles versus Radius

Figure III-A-2

The reason this regime was chosen is that it is the easiest to explore numerically, since electron drag, the determining factor in the slowing down of the alpha particles, scales as $n_e/T_e^{3/2}$. The amount of computation required per particle track scales inversely with the drag on the particle. From a study of individual particle orbits, it was found that the drift surface motion was a function of the energy loss rate. If the drag force was increased, the displacement of the drift surface was also increased, but, as will be shown later, the plot of the drift surface position versus particle energy was not dependent on the drag force. Thus the data presented in this chapter should be valid for a wide range of plasma densities and temperatures. Particles born in loss cones escape immediately. Particles born far away from loss cones remain confined until they thermalize with the background plasma. Particles born near loss cones remain confined until they are pushed into a loss region by the drag and scattering forces. However, since the drag term $<(\Delta V_{\parallel})>$ and the scattering term $<(\Delta V_{\perp})^2>$ both scale linearly with time, an escaping particle will leave with a final energy nearly independent of the magnitude of the drag and scattering forces.

A change in the plasma's profile shapes will affect the net energy confinement of the reactor, since the

source distribution depends on the plasma's density and temperature. In general, flatter profile shapes result in a higher percentage of particles being born near the separatrix, where the loss regions are larger. Net energy confinement is, therefore, lower with flat profiles, and higher with more peaked profiles.

The choices for machine sizes were made as follows: the canonical size for the coil minor radius was chosen to be 4 meters, allowing a sufficient plasma volume to load the first wall with 1.5-2 MW/m^2 of primary fusion power, and enough space for the blankets and magnet shields. The pitch length was determined by the size of the separatrix, and the desire to be near the force-minimum winding configuration ($2\pi a/p \cong 1$). A constraint was imposed that the separatrix would be no closer than 1.75 meters to a helical coil. The closest point occurred along the inside edge of the small aspect-ratio machine, since large toroidicity tends to push the flux surfaces in towards the major axis. It was found that by unwinding the pitch so that $2\pi a/p \cong .89$, the 1.75 meter separation could be maintained at this point. (In general, a shorter pitch length enlarges the separatrix).

The current in the helical winding was chosen such that the machines of different aspect ratios would enclose the same amount of toroidal flux within their separatrixes. Also, their poloidal flux per unit length were closely

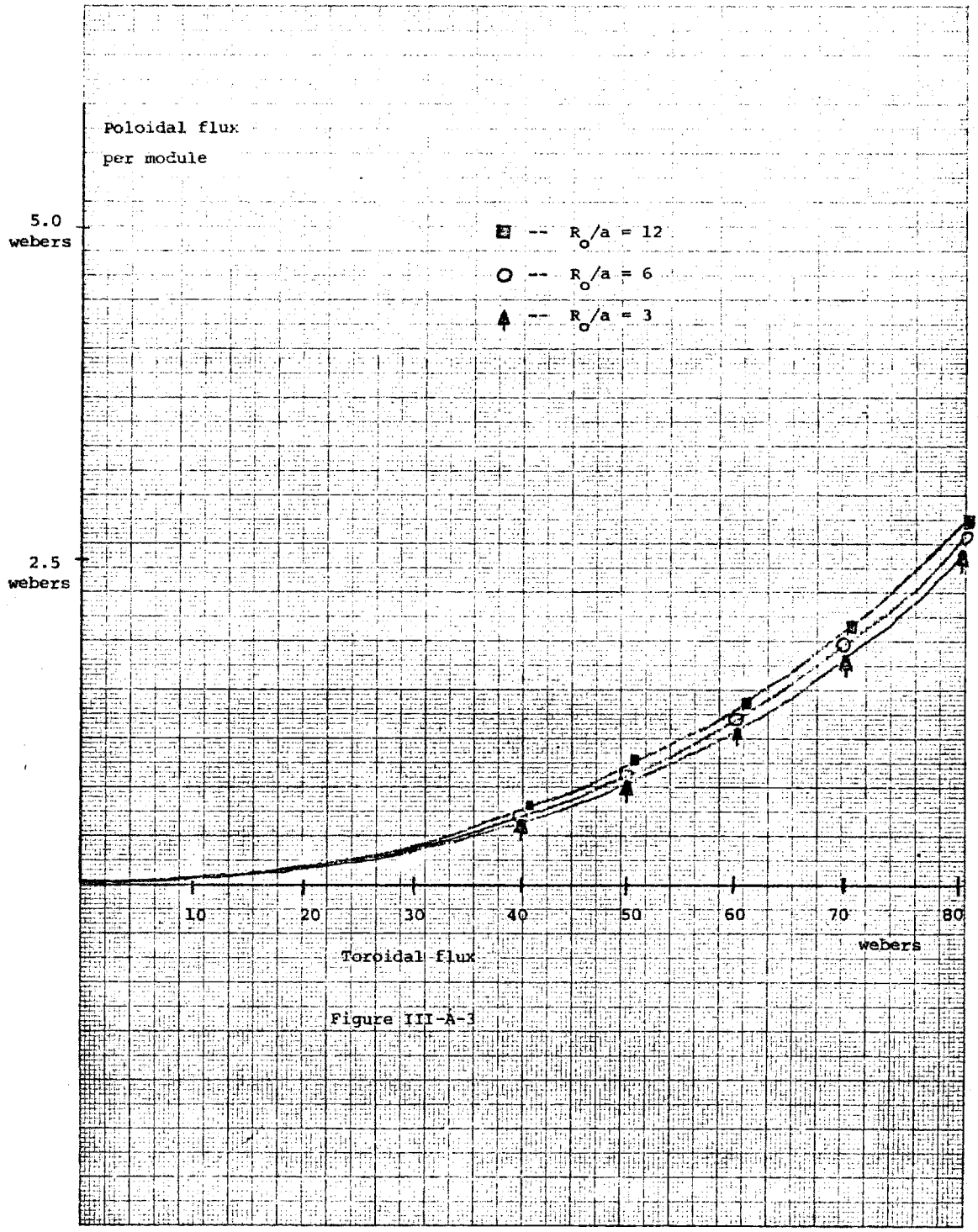

Figure III-A-3

matched, see Figure III-A-3. This shows that the rotational transform per module is approximately the same for each machine , since $\dot{t} = d\psi_p/d\psi_T$.

The values of flux and axis magnetic field are shown in Table III-A-1. Each machine was designed with $a_c = 4$ meters, $\ell = 3$, p = 9.42 meters = 1 module length, and with a constant pitch winding law that is described in Appendix A.

Machine Designation	A	B	C	D
aspect ratio	12	6	3	3
B_o(axis)	5.50 Tesla	5.31 Tesla	5.05 Tesla	10.10 Tesla
ψ_t(separatrix)	82.8 webers	82.8 webers	82.8 webers	165.6 webers
R_o	48 meters	24 meters	12 meters	12 meters
N	32	16	8	8

TABLE III-A-1

B. Description of Methods Used to Determine Alpha Particle Power Deposition

In Chapter II I described how a single alpha particle is tracked as it thermalizes with the background plasma. I now explain how many such orbits are combined to yield a power deposition profile in the plasma.

A 4-dimensional phase space grid (3 spatial directions and a pitch angle direction) was created within each reactor module with 4096 grid locations. The grid had 4

steps equally spaced in the toroidal direction, 8 steps equally spaced in the poloidal direction, 8 steps equally spaced in the flux direction from axis to separatrix, and 16 steps equally spaced in the cos(pitch angle) direction from -1 to +1 (resulting in each grid location representing an equal area on the velocity sphere). As an alpha particle was launched, a record was kept of all the phase-space locations in which the particle existed before it lost its first 100 keV of kinetic energy. (For a 3.51 MeV alpha particle, this represented about 2.8% of its initial kinetic energy). Also, as the particle was being tracked until either thermalization or escape, a record was kept of the flux regions in which the particle was depositing its energy. This process was continued for each alpha particle launched, until all of the phase space locations in the grid had at least one alpha particle passing through it before said particle lost its first 100 keV of kinetic energy. Then, for each grid location, the set of all particles making this initial contact was taken to be a set of particles originating at that grid location. The energy deposition profiles of the particles within each set were averaged, producing an energy deposition profile for each grid location. Then, each grid location deposition profile is weighted with a source strength determined by the values of n and T at the flux coordinate associated

with the grid location. These grid deposition profiles are then summed to obtain a grid sink profile, showing how much power is deposited at each grid location per unit power created in the total plasma volume. The percentage energy confinement for the entire plasma is the sum of the 4 dimensional sink grid. The percentage energy confinement for particles originating in the i'th velocity-space angle is obtained from the grid deposition profiles:

$$\%\text{energy confined}_{\chi_i} = \sum_{\psi=1}^{8} \sum_{\theta=1}^{8} \sum_{\phi=1}^{4} \frac{\text{Power deposited from } \psi\theta\phi\chi_i}{P_{total}/16}$$

for i = 1 to 16. [III-B-1]

Similarly, the percentage energy confinement for all particles originating on the j'th flux surface is:

$$\%\text{energy confined}_{\psi_j} = \frac{\sum_{\chi=1}^{16} \sum_{\theta=1}^{8} \sum_{\phi=1}^{4} \text{Power deposited from } \psi_j\theta\phi\chi}{\text{Power } (\psi_j)}$$

[III-B-2]

As described in Chapter II, considerable effort was spent in designing the orbit tracking code to be as efficient as possible. The use of cubic spline interpolation added two orders of magnitude in speed relative to a code which directly evaluated B and ∇B from current segments,

and the use of a guiding center code added two orders of magnitude in speed relative to a particle following code. This allowed an alpha particle with $V_\perp >> V_{||}$ to be tracked until thermalization in 30 to 60 sec. of CRAY CPU, which was an acceptably small number. The well circulating particles, however, made many more toroidal and poloidal orbits than the trapped particles, resulting in $\sim 5.10^6$ B and ∇B evalutions per particle as the particles were tracked through ~5000 poloidal orbits. This totaled to about 10 minutes CRAY CPU per particle, which was unacceptably large. In an effort to reduce this CPU requirement, noted that these well circulating particles, unlike their trapped counterparts, execute extremely periodic and well ordered motion in their poloidal orbits around their drift surfaces. Since the effect of the drag forces are a small perturbation on this motion, I calculated the track of one poloidal orbit and accumulated the drag and scattering effects of several orbits on this track. I termed this procedure "push processing" and refer to an orbit thus tracked as a "push-processed" orbit. See Figures II-B-1, 2,3 for a comparison between a standard and a push-processed orbit. For the standard orbit, 5163 poloidal orbits were tracked, requiring 20 minutes of CPU on a CDC 7600. In comparison, the push-processed orbit required only 388 poloidal orbits to be tracked, while the effect of an additional 4779 poloidal orbits was simulated by

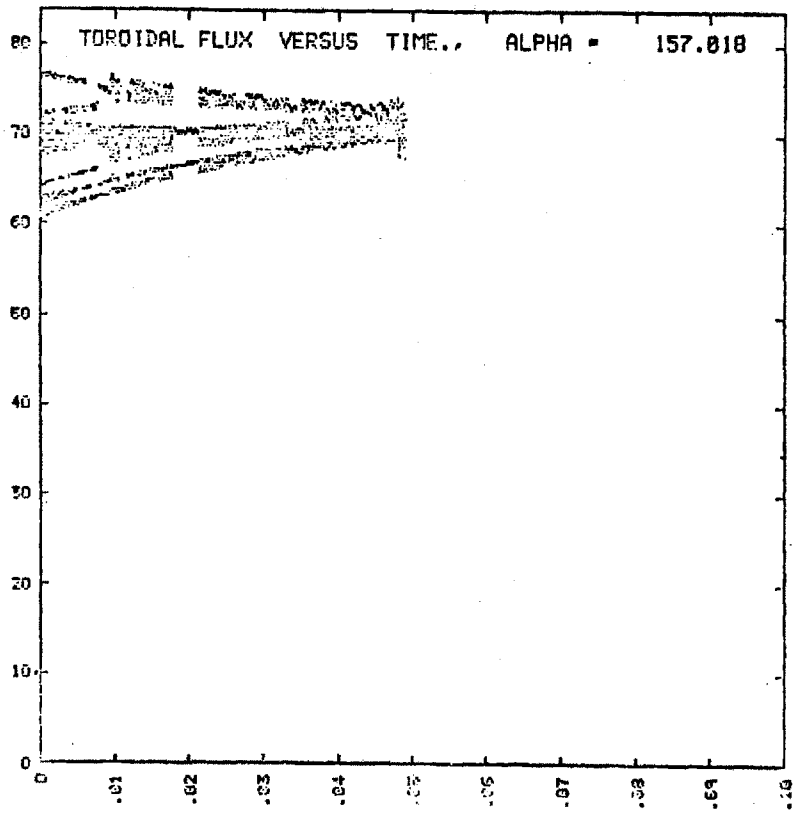

Standard Orbit

```
CPU =  1183145574
 IO =     2206422,  SYS =       65136
TIMEX = 4.9130062E-02
NIT =  1015241
EFINEV = 8.2319224E+03
ETE = 3.1801841E+06     ETI = 3.2458879E+05
XPOS =  10.0364,  YPOS =   2.0292
         0.          0.          0.          0.
         0.      32526.    2551247.     920999.

   69.88   69.51   69.61   71.08   69.00    0.      0.      0.      0.

 -0.9256 -0.9423 -0.9163 -0.9286 -0.9287  0.      0.      0.      0.

    5.6281E-13    3.0392E-13    1.5910E-13    7.8763E-14    3.2961E-14
    0.            0.            0.            0.

NPO =   5163
RNPPO =   -0.000
NEJ =     0
```

Figure III-B-1

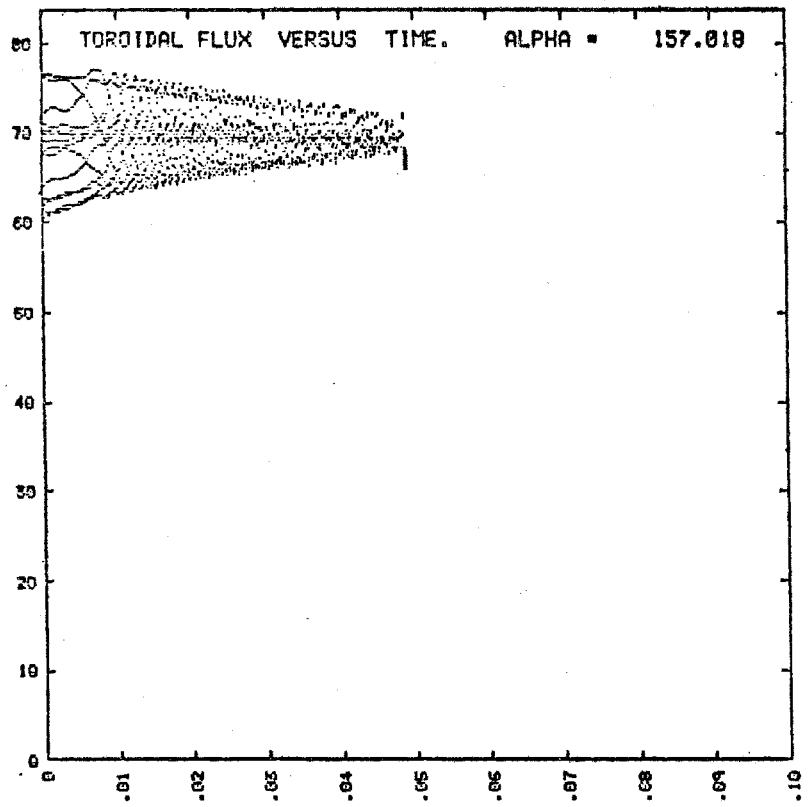

Push-processed Orbit

```
CPU =    94125498
 IO =     1708806.  SYS =      66131
TIMEX = 4.9799461E-02
NIT =    80002
EFINEV = 1.0774427E+04
ETE = 3.1713095E+06     ETI = 3.3092087E+05
XPOS =  10.2396.  YPOS =   1.6469
          0.        0.        0.        0.
          0.     42147.   2664122.    795962.

   69.88   70.07   70.09   72.76   69.67    0.      0.      0.      0.

 -0.9256 -0.9322 -0.9736 -0.9216 -0.6844  0.      0.      0.      0.

    5.6281E-13    3.0433E-13    1.6083E-13    8.1201E-14    3.5353E-14
    0.            0.            0.            0.

NPO =    388
RNPPO = 4779.728
NEJ =     0
```

Figure III-B-2

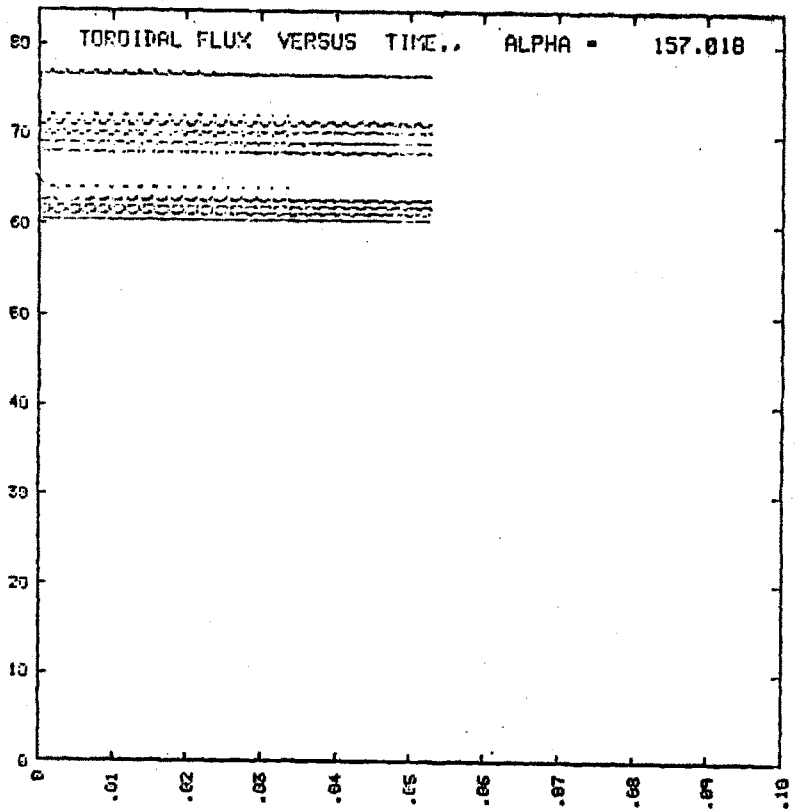

Vacuum Orbit

```
CPU =   230544803
 IO =     3160599,  SYS =       62591
TIMEX = 5.2773069E-02
NIT =   200001
EFINEV = 3.5130048E+06
ETE = 1.0593473E-24     ETI = 1.1603945E-26
XPOS =  13.0865,  YPOS =  -0.0118
        0.         0.         0.         0.
        0.         0.         0.         0.

   69.88   71.33   72.18   68.06   60.60   62.73    0.       0.       0.

 -0.9257 -0.9122 -0.9131 -0.9413 -0.9340 -0.9391  0.       0.       0.

    5.6282E-13    5.6282E-13    5.6282E-13    5.6282E-13    5.6282E-13
    5.6282E-13    0.            0.            0.

NPO =    416
RMPPO = 4180.944
NEJ =      0
```

Figure III-B-3

the push-processing technique. The push-processed orbit required only 1.6 minutes of CPU on the CDC7600. Figures II-B-1,2 show that push-processing does indeed produce the same deposition profile as the standard tracking algorithm. This is an extremely favorable result. Not only does this result allow a large saving in computation, it implies that, for given plasma profile shape, the calculated energy confinement for the circulating particles should be valid for a wide range of plasma regimes. Since the drift surface displacement is a function of the integrated effect of the drag forces, and the energy lost by the alpha particle is also a function of the time integrated effect of the drag forces, a plot of drift surface position versus particle energy is independent of the magnitude of the drag force (Figure II-B-4). Hence the calculated orbit is valid for a wide range of plasma conditions, as long as the scattering and slowing-down times are still much greater than a poloidal orbit time.

Figures III-B-1,2 also illustrate a general effect seen in the other well-circulating alpha particle tracks: scattering effects are small before the particle has lost 80% of its energy, and the primary effect of the drag force is to reduce the flux surface excursions of the well-circulating particles. This is plausible, since $V_{\parallel}$ of the guiding center scales with $\sqrt{\text{energy}}$ while $V_{\perp}$ scales with energy. One would expect the following scaling

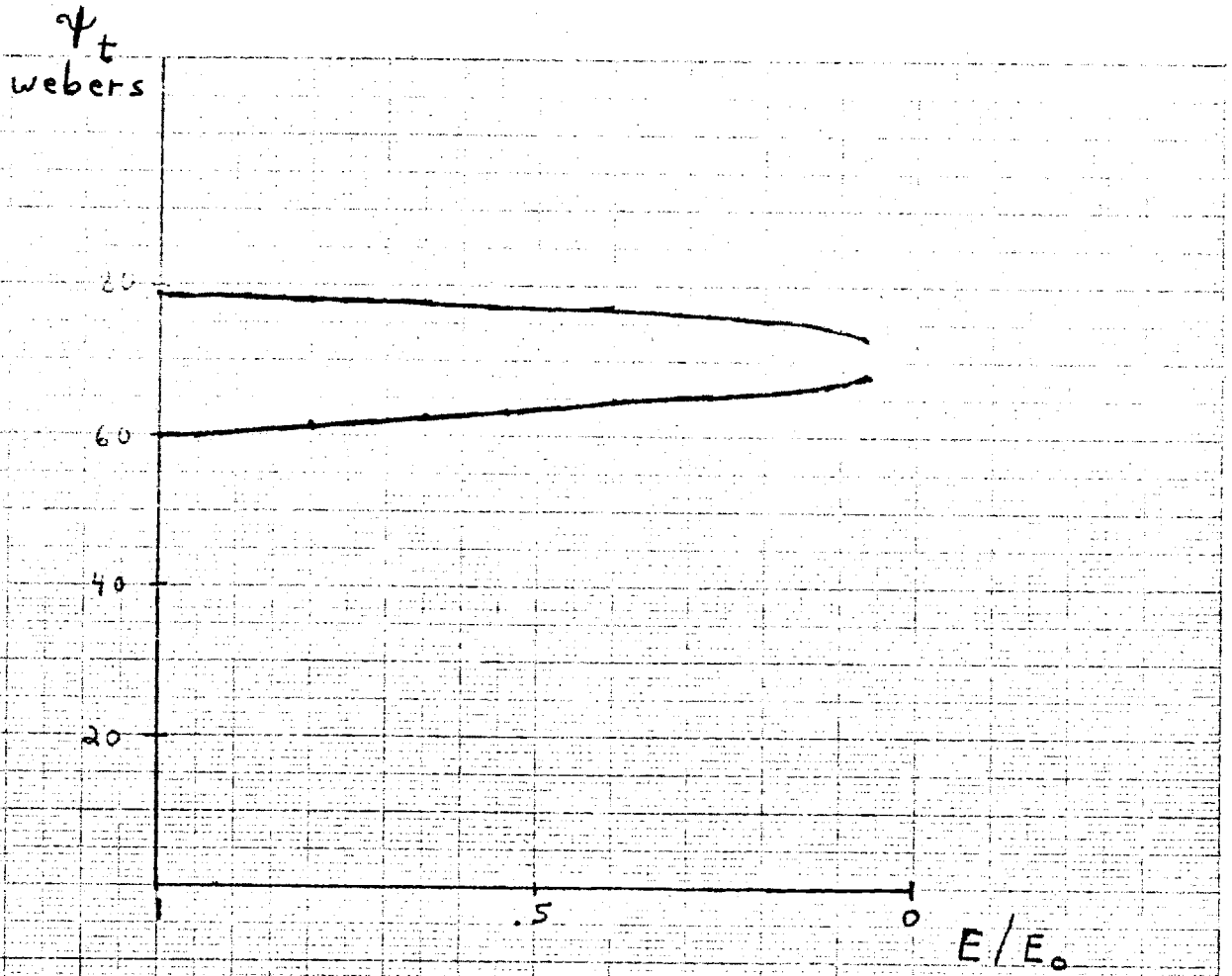

Figure III-B-4

Maximum and minimum flux position during poloidal orbit versus alpha-particle energy. Plot is for both figures III-B-1 and III-B-2, no change observed when drag and scattering forces augmented by a factor of 13.

for the magnetic surface excursion Δr:

$$\Delta r \sim V_\perp \ \delta t_{\text{poloidal orbit}} \sim \frac{V_\perp}{V_{||}} \sim \sqrt{E}$$

Near the separtrix, $\Delta\psi \alpha \Delta r$, so a table can be made from Figures III-B-1,2 showing the scaling of $(\Delta r)^2$ with E.

Time (ms)	$\Delta\psi_t(t)^2/\Delta\psi_t(0)^2$	$E(t)/E_o$
0	1	1
10	.51	.54
20	.30	.28
30	.15	.14
40	.09	.06

TABLE III-B-1

The excursion scales with energy in the expected manner.

I will now describe how puch-processing was implemented into the orbit tracking code. Push processing was only done on the orbits of well circulating particles, since the orbits of the bouncing particles have nonperiodic motion that would not be accurately simulated with a push-processing code involved identifying the well-circulating particles. A well-circulating particle was defined in the code as any particle which, in its previous five poloidal orbits, had $\delta_{min} > 1/8$, where δ_{min} is the minimum value of $|\cos(V_{||}/V)|$ during these orbits. The drag and scattering forces on a well-circulating particle were en-

hanced by a factor $1+20*(\delta_{min} - \frac{1}{8})$. This factor resulted in a tenfold savings in computation requirements, yet still kept the poloidal orbit times of the hot alpha particles much shorter than their slowing down times. After each poloidal orbit, δ_{min} and the enhancement factor were recomputed. This resulted in a smooth turn-off of push-processing when a particle drifted in velocity space from a well-circulating region towards a trapped region.

C. Presentation of Data

Using the procedures and parameters described in the previous two sections, the percentage of α-particle power deposited in the plasma was found for the four reactor designs described in Table III-A-1. Graphs of the fractional power confinement versus cos (pitch angle) and flux surface are given in Figure III-C-1, and the confinement percentages are listed in Table III-C-1,

Machine	Aspect Ratio	%power confined	Prompt Loss Loss
A	12	99.4%	60%
B	6	90.3%	83%
C	3	65.6%	88%
D	3(high field)	70.1%	86%

TABLE III-C-1

As can be seen in Figure III-C-1, both trapped and circulating particles are well confined in the large aspect ratio machines, and only trapped particles are poorly

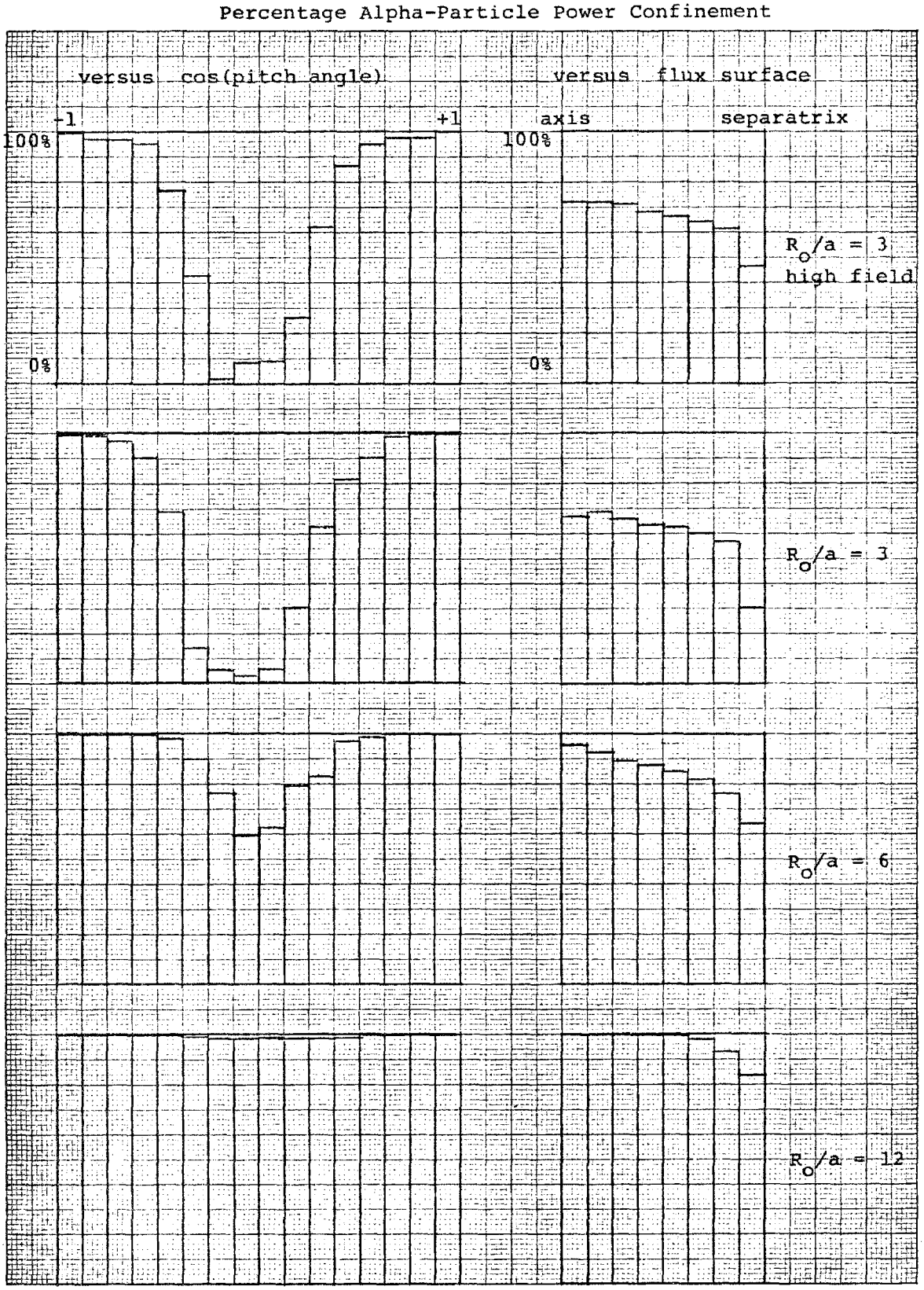

Figure III-C-1

confined in the low aspect ratio machines. Also, the high field device shows a narrowing of the loss cones produced by the toroidicity of the windings, though this effect is small compared to the effect produced by changing the aspect ratio.

As discussed in Chapter II, the effect of a background electrostatic profile on the alpha particles is negligible for potential differences between the axis and separatrix that are less than 10 kV. The actual voltage profiles that would be established in a torsatron by ambipolar diffusion is unknown, and depends in a complex way on the plasma equilibrium and conductivity, and on the sources and sinks of alpha particles and injected ions. For the confinement studies of this thesis, a low value of V_{axis} (3000 volts $\cong$ 40% T_e) was chosen as an intermediate value, the weak electric fields neither aiding nor hindering particle confinement.

In each of the four confinement studies, between 80% and 90% of the energy loss was due to particles escaping before completing one poloidal orbit. Particles born in loss cones escape immediately. Particles born on confined orbits will in general lose most of their energy to the background plasma before scattering into a loss cone. The data from the R_o/a = 12 reactor case also show that bouncing alpha particles can spend a long time

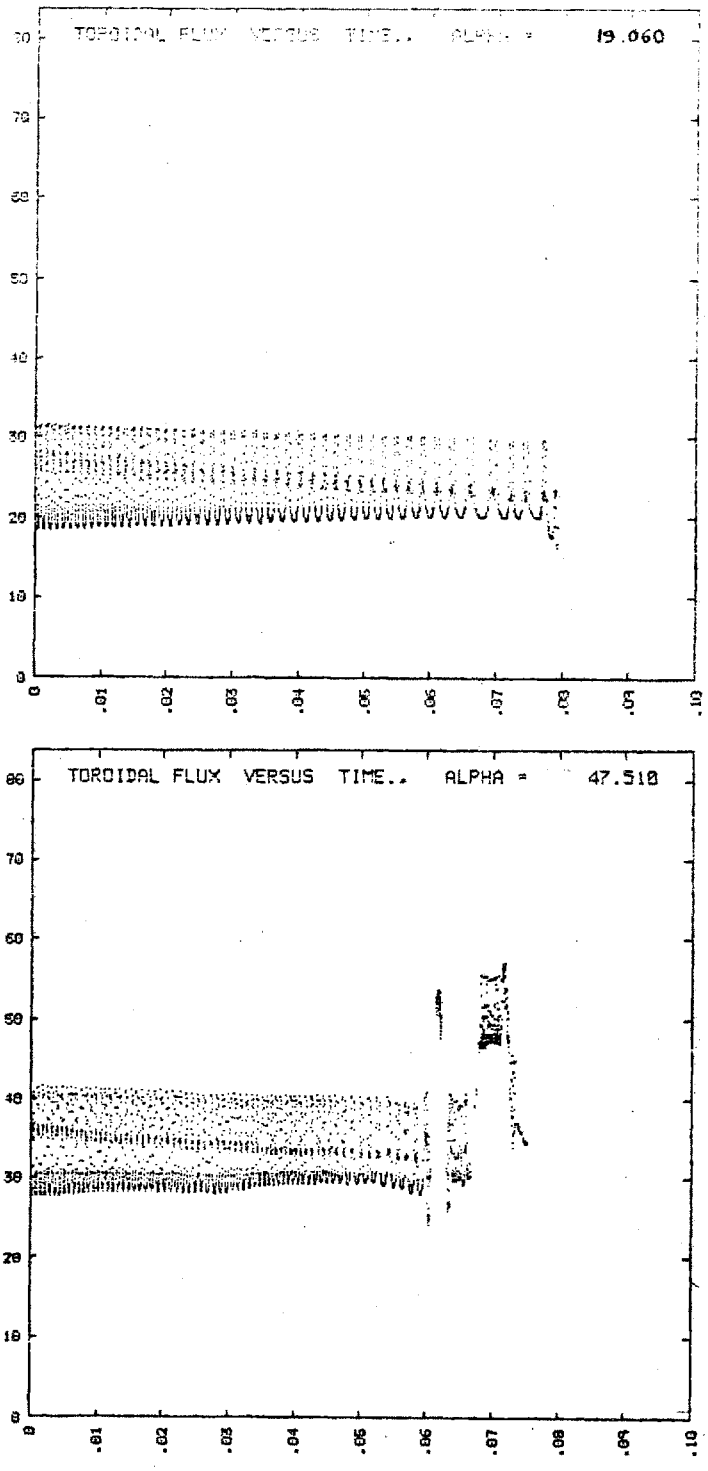

Figure III-C-2. These graphs show typical alpha particle orbits during thermalization for various pitch angles (ALPHA), which are given in degrees. (ALPHA = 0 implies a co-streaming particle.)

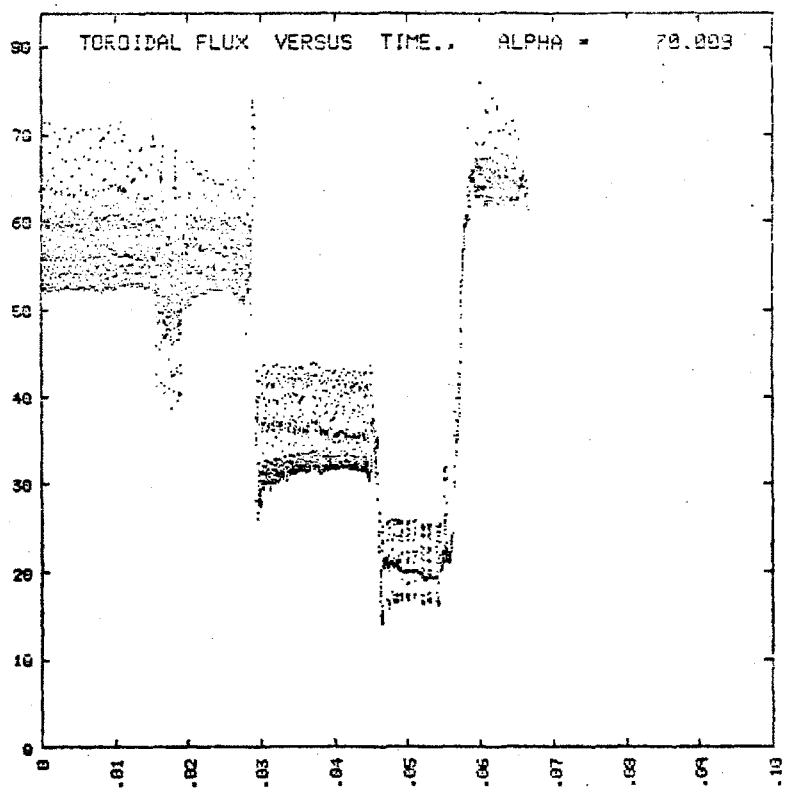
TOROIDAL FLUX VERSUS TIME.. ALPHA = 70.000
80
70
60
50
40
30
20
10
0
0
.01
.02
.03
.04
.05
.06
.07
.08
.09
.10

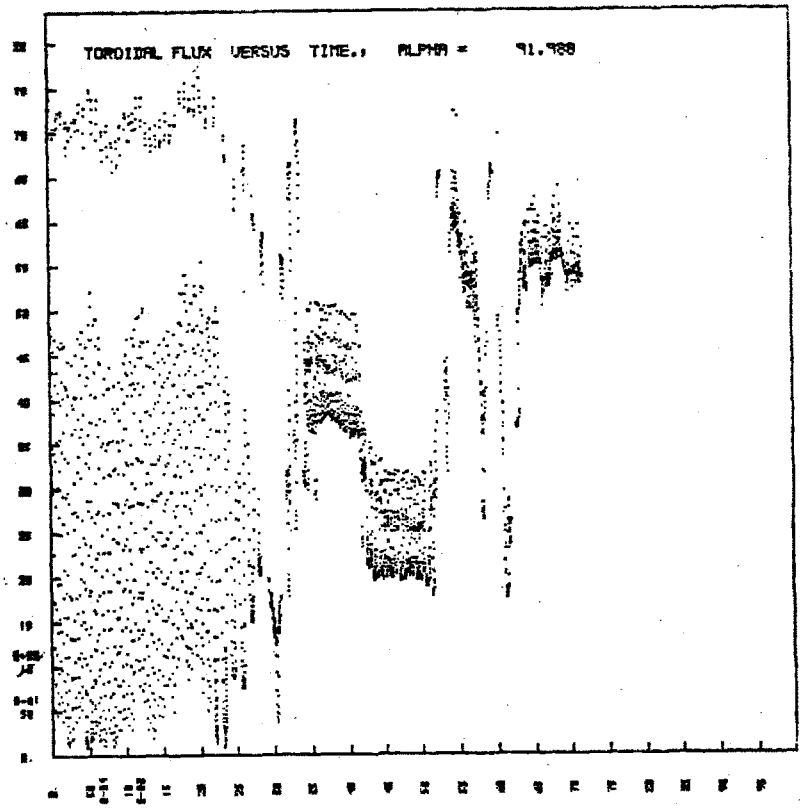
TOROIDAL FLUX VERSUS TIME.. ALPHA = 71.988

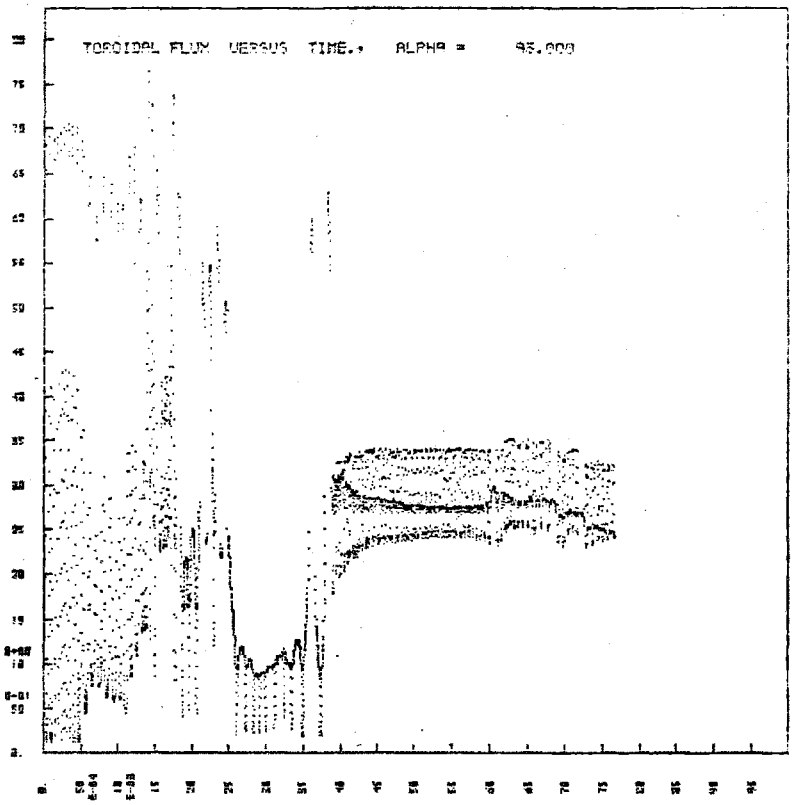
TOROIDAL FLUX VERSUS TIME., ALPHA = 95.000

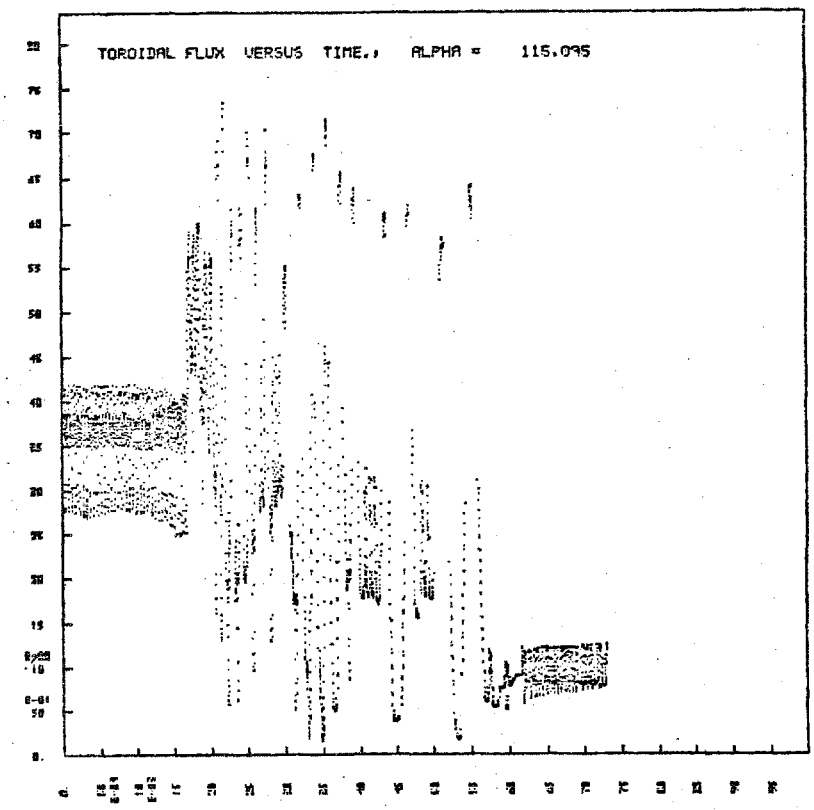
TOROIDAL FLUX VERSUS TIME., ALPHA = 115.095

(~100 ms) wandering in the helical grooves of the torsatron without escaping (see Figure III-C-2). The toroidal curvature of the magnetic field tends to creat loss cones in velocity space at these bounce regions. A severe example of this is the $R_o/a = 3$ torsatron, where the toroidal effects are large and almost all of the alpha particles born in the bounce cone are unconfined.

D. Conclusions

Within torsatrons of reactor size, the magnetic moment μ of alpha particles was found to be an extremely well-conserved quantity. Using a μ conserving integration code, several hundred α particle orbits were tracked in torsatrons with aspect ratios of 3, 6 and 12. These orbits were used to calculate the percentage confinement of alpha particle energy as a function of flux position and pitch angle. The results are shown in Figure III-C-1.

Well circulating alpha particles were found to be well confined in all the torsatrons investigated. This is consistent with the model for well-criculating orbits developed in Chapter II. The motion of well-circulating particles is extremely periodic and relatively insensitive to energy and pitch angle scattering. Hence most α-particles that are born with closed, circulating orbits tend to remain confined until thermalization.

Non-circulating α-particles were found to be well

confined in torsatrons with $R_o/a = 12$, moderately confined with $R_o/a = 6$, and poorly confined with $R_o/a = 3$. In the low aspect ratio device, the large toroidal curvature of the magnetic field created a large loss cone in phase space where $|\cos(\text{pitch angle})| \lesssim 0.3$. This loss cone was slightly decreased by raising the magnetic field strength on axis from 5.05 tesla to 10.1 tesla, resulting in an overall percentage increase in confined alpha-particle power of 4.5% (from 65.6% to 70.1% power confinement). This benefit is slight compared to the advantage of a higher aspect-ratio device; the $R_o/a = 6$ machine had 90.3% overall power confinement, while the $R_o/a = 12$ machine had 99.4%.

Alpha-particle power confinement was found to be insensitive to the background plasma conditions. Between 60% and 90% of the lost power is carried away by alpha particles born in loss cones and escaping before completing a poloidal orbit. The remaining loss results from particles being scattered into the loss cones by the integrated effects of the scattering and drag forces. Since energy deposition into the background plasma is also proportional to the integrated effect of the drag forces, the power loss due to alpha particles being scattered into loss cones is independent of the background plasma's temperature

and density, as long as

$$\tau^{\alpha}_{\text{poloidal orbit}} \ll \tau^{\alpha}_{\text{slowing down}}.$$

Chapter IV. THERMAL PARTICLE CONFINEMENT AND DIFFUSION

A. Motivations and Assumptions

The main object of this thesis is the estimation of energy deposition and diffusive transport in a torsatron plasma. The data from Chapter III give the energy deposition into the plasma from the fusion-produced α-particles. In this chapter, a method is developed to numerically measure the diffusive transport of energy due to the ion thermal conductivity (χ_i). The scaling of χ_i is compared with that predicted by ripple transport theory. This theory associates large transport coefficients with the helical modulation, or ripple, of the field strength on the flux surfaces of the torsatron, due to particles trapped in the helical magnetic wells.[1, 2]

Power losses due to bremsstrahlung and particles scattering into unconfined orbits are also calculated. These losses, together with the diffusive energy loss rates, are then compared with energy deposition rates due to the α-particles, and an estimate is given for the minimum aspect ratio of an ignited torsatron.

B. Loss Cones of Thermal Particles

This section describes the techniques used in finding the loss regions in phase space of thermal deuterons. The methods used were very similar to those used in finding the percentage of α-particle confinement (see Chapter III, Section B). A 4-D phase space grid (3 spatial directions

and a pitch angle direction) was again created within each reactor module studied. A set of deuterons was launched, and the phase space partitions that each deuteron entered were recorded. Each deuteron was tracked for 16 msec, and was considered to be promptly lost if it escaped during this time. This tracking time is long compared to the ion-ion scattering time of the α-particle confinement study of Chapter III (with $n_e = 3 \cdot 10^{20}/m^3$ and $T_i = 8$ keV, $\tau_{ii}^{scat} \tilde{=} 2.7$ msec). Also, the tracking time was sufficient to allow the 8 keV deuterons to complete 10 to 20 circulating orbits or 1 to 3 trapped orbits; thus if a particle remains confined for 16 msec, it is probably on a confined orbit. The tracking runs were done without a background plasma, since I desired to locate in the vacuum field the positions of loss regions in phase space for thermal energy deuterons.

For each reactor study, deuterons were launched until each of the phase space locations in the grid had at least one deuteron passing through it. Then, for each grid location, the set of all deuterons passing through the location was equated with the fraction of deuterons in the set that remained confined during the 16 msec tracking runs. The percentage confinement for all particles originating on the j'th flux surface is:

$$\% \text{ confined}_{\psi_j} = \frac{\sum_{\chi=1}^{16} \sum_{\theta=1}^{8} \sum_{\phi=1}^{4} \% \text{ confined}_{\chi\,\theta\,\phi\,\psi_j}}{512} \qquad \text{[IV-B-1]}$$

Similarly, the percentage confined for all particles originating in the i'th velocity space angle is obtained by:

$$\%\ \text{confined}_{\not\leftarrow_i} = \frac{\sum_{\theta=1}^{8}\sum_{\phi=1}^{4}\sum_{\psi=1}^{8} (\%\ \text{confined}_{\not\leftarrow_i\,\theta\phi\psi})\ n^*(\psi)}{32\sum_{\psi=1}^{8} n^*(\psi)} \qquad \text{[IV-B-2]}$$

where $n^*(\psi)$ is the density shape function. The results are plotted in Figure IV-B-1. The four reactors studied were those used in the alpha-particle confinement study described in Chapter III. In the plots of thermal deuteron confinement versus cos(pitch angle), the same $n^*(\psi)$ profile shape was chosen that existed for the alpha-particle populations of Chapter III. This allows a direct comparison of the loss regions in pitch angle space between high energy alpha-particles and thermal deuterons, since most of the escaping alpha-particles were promptly lost and hence their percentage power confinement profiles are approximately equal to their percentage particle confinement profiles. The plots of particle confinement versus flux surface position are independent of the density shape profile, and the confinement percentages of alphas and deuterons versus flux position can again be directly compared. A discussion on these results is postposed until Part E of this chapter.

C. Description of Methods Used in Finding the Ion Thermal Conductivity

The ion thermal conductivity of a plasma can be obtained from the rate of diffusive spreading of a test

Percentage particle confinement for thermal deuterons

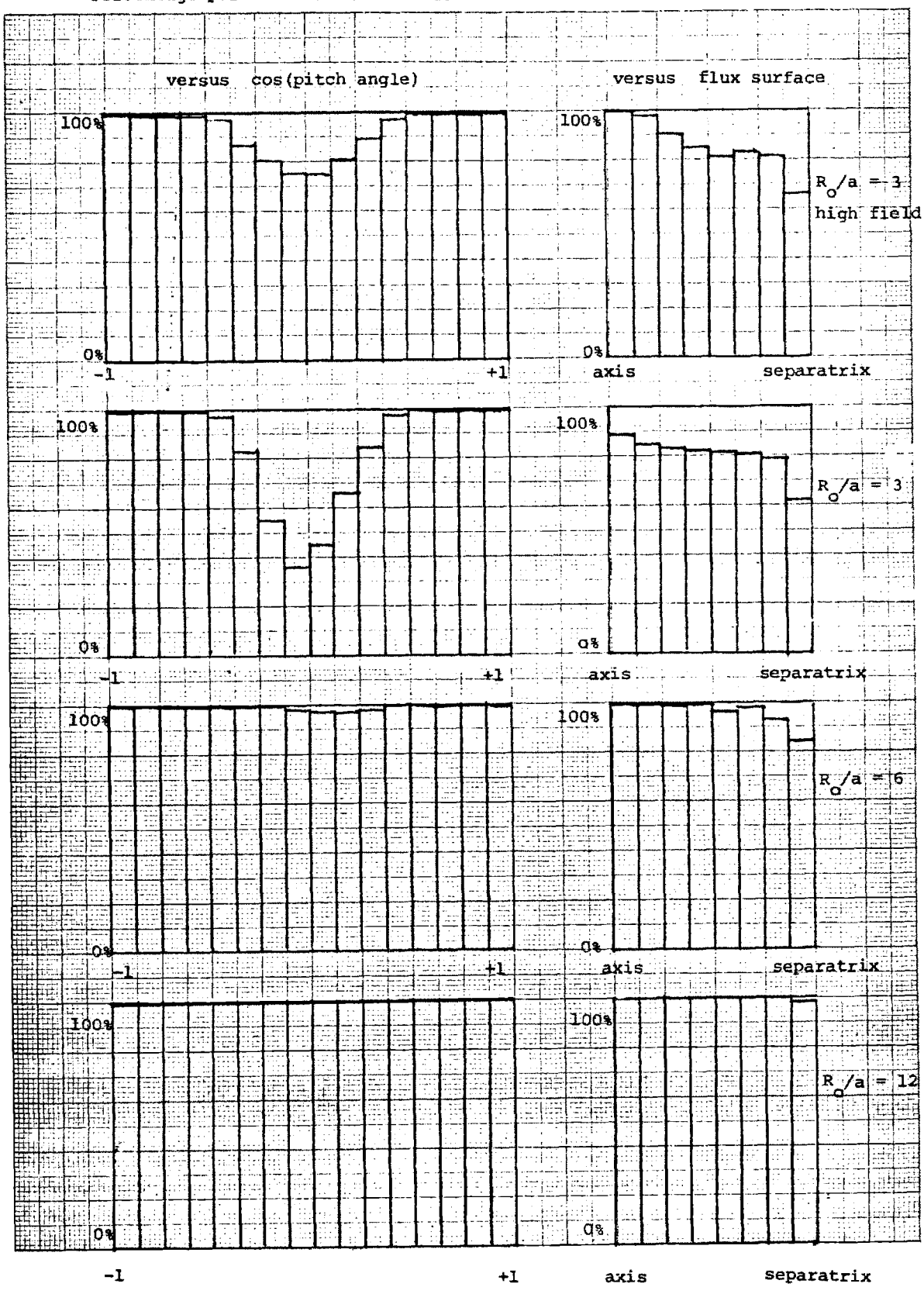

Figure IV-B-1

particle distribution interacting with a background plasma. All relevant collisional effects must be included in the orbits of the test particles. These effects are represented by the following Coulomb interaction coefficients:[3]

1) dynamical friction term --

$$\frac{\langle \Delta V_{\parallel} \rangle}{\Delta t} = - \sum_{\beta} A_{\beta} \left(1 + \frac{m_{test}}{m_{\beta}} \right) \frac{1}{\nu_{th_{\beta}}^{2}} \; G\left(\frac{\nu_{test}}{\nu_{th\beta}} \right) \qquad \text{[IV-C-1]}$$

2) energy scattering term --

$$\frac{\langle (\Delta V_{\parallel})^{2} \rangle}{\Delta t} = \sum_{\beta} A_{\beta} \frac{1}{\nu_{test}} \; G\left(\frac{\nu_{test}}{\nu_{th_{\beta}}} \right) \qquad \text{[IV-C-2]}$$

3) pitch-angle scattering term --

$$\frac{\langle (\Delta V_{\perp})^{2} \rangle}{\Delta t} = \sum_{\beta} A_{\beta} \frac{1}{\nu_{test}} \left[\Phi\left(\frac{\nu_{test}}{\nu_{th_{\beta}}} \right) - G\left(\frac{\nu_{test}}{\nu_{th_{\beta}}} \right) \right] \qquad \text{[IV-C-3]}$$

where :

$\sum_{\beta}$ = summation over all relevant field particle species.

$$A_{\beta} = \frac{n_{\beta} Z_{test}^{2} Z_{\beta}^{2} e^{4} \ln \Lambda_{\beta}}{2\pi \epsilon_{o}^{2} m_{test}^{2}} \qquad \text{[IV-C-4]}$$

$$\Lambda_{\beta} = \frac{12\pi \left(\epsilon_{o} k_{B} T_{\beta} / e^{2} \right)^{3/2}}{\sqrt{n_{\beta}}} \qquad \text{[IV-C-5]}$$

n_β = density of β'th field species

$$v_{th_\beta}^2 = \frac{2 k_\beta T_\beta}{m_\beta} \qquad \text{[IV-C-6]}$$

$$\Phi(X) = \frac{2}{\sqrt{\pi}} \int_0^X e^{-y^2} dy \qquad \text{[IV-C-7]}$$

$$G(X) = \frac{\Phi(X) - X\Phi'(X)}{2X^2} = \frac{2}{\sqrt{\pi} X^2} \int_0^X y^2 e^{-y^2} dy \qquad \text{[IV-C-8]}$$

In measuring the diffusive spreading of the test particle distribution, only ion-ion scattering effects were included. This simplification is possible when thermal conductivity is being calculated, since the test ions interact much more strongly with the field ions than with the field electrons. The momentum of the test particle distribution is not conserved, since the test particles are exchanging momentum and energy with the background plasma. This is acceptable, since I am only measuring the energy transport. It is questionable whether this approach would be valid in measuring particle transport, as the method only would measure the Lorentz part of particle diffusion, and not the momentum conserving part, D_m. It is currently unknown to what extent D_m cancels $D_{Lorentz}$ in the torsatron magnetic configuration.[17]

I now describe how the ion-ion interaction terms were implemented in the test-particle tracking code. After each time step, $\frac{<\Delta V_{\parallel}>}{\Delta t}$, $\frac{<(\Delta V_{\parallel})^2>}{\Delta t}$ and $\frac{<(\Delta V_{\perp})^2>}{\Delta t}$ were were computed, and multiplied by the Δt of the time step. Then, random directions were chosen in pitch-angle and V, and used as the directions of $<(\Delta V_{\perp})^2>$ and $<(\Delta V_{\parallel})^2>$, respectively. These velocity vectors, along with the $<\Delta V_{\parallel}>$ vector, were added to the test particle's velocity space position, and the particle's new V, $V_{\parallel}$, and μ were computed. This method is valid when $\Delta V/V << 1$ for the time step. In the tracking runs, using ions of mass 2.5 u, $\Delta V/V$ was << 1 for plasma densities up to and including one order of magnitude above the regime of reactor interest (i.e., for an 8 keV plasma, $n_{max} = 2 \cdot 10^{21}/m^3$). The accuracy of the scattering was tested by observing whether the test particle would have a Maxwellian distribution in kinetic energy if tracked over many scattering times, and if it would maintain a random position on the velocity sphere. In a trial run shown in Figures IV-C-1, 2 a particle was tracked for 5200 scattering times. In the graph of probability versus energy, the histogram represents the particle's energy distribution, while the solid curve represents a theoretical Maxwellian distribution (the horizontal tic marks show units of energy). The close match between theory and observation was taken as confirmation that the code was accurately simulating drag and energy scattering. Observation of the tracking code results

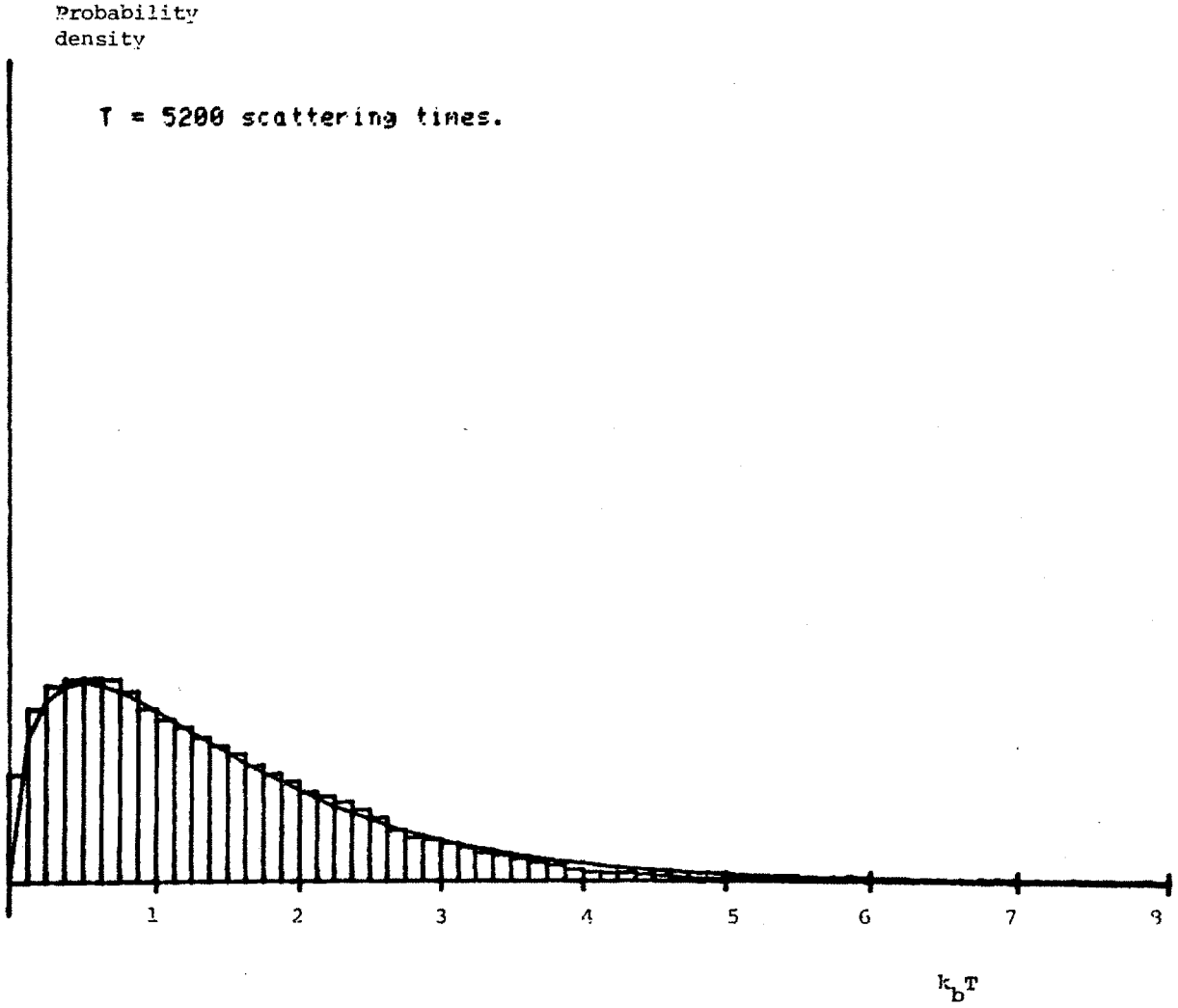

Figure IV-C-1

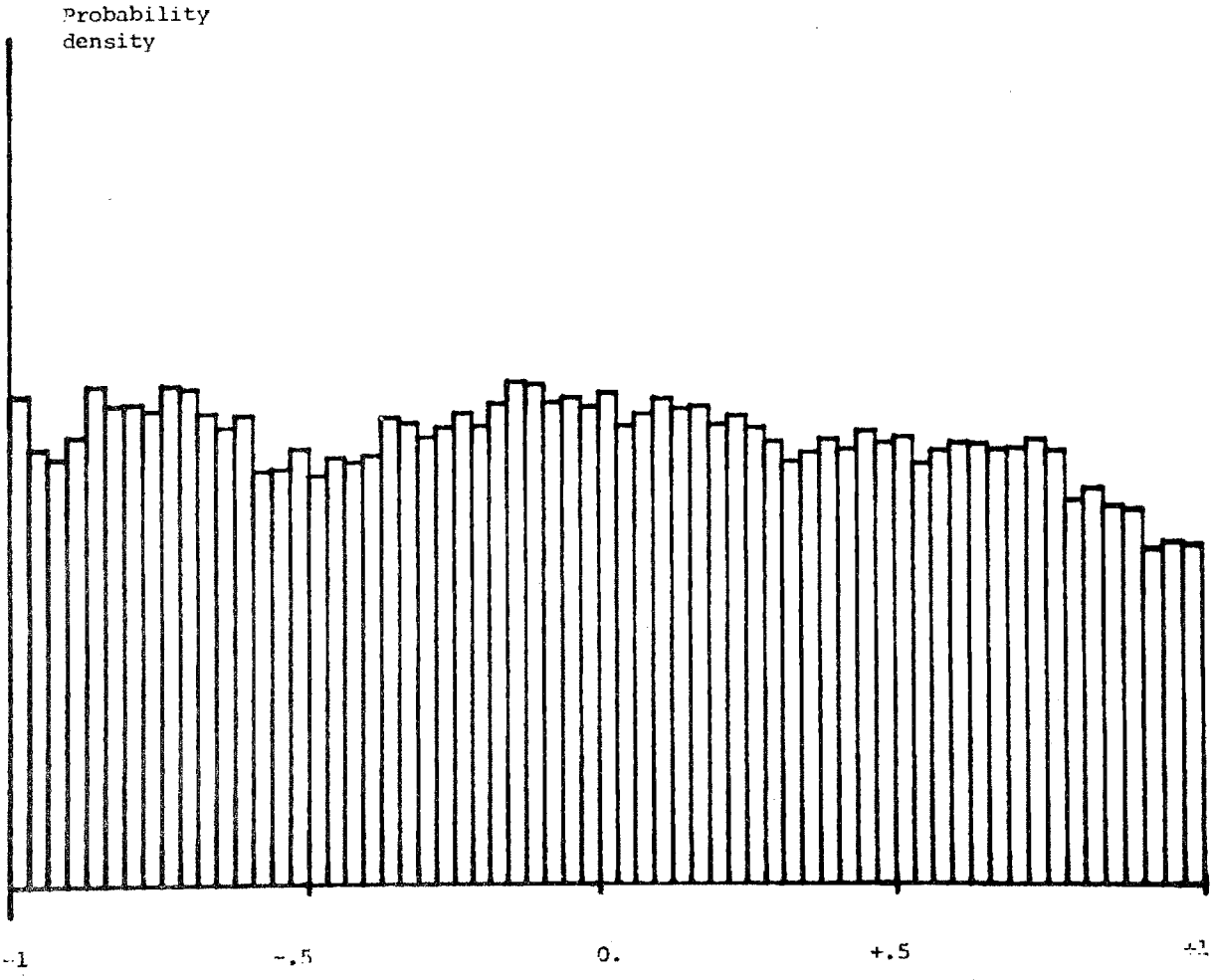

Figure IV-C-2

showed that a pitch-angle correlation time was about equal to a theoretical scattering time, and Figure IV-C-2 shows that the tracked particle was spending approximately equal time in the equal area segments of the velocity sphere. This was taken as confirmation that the code was accurately simulating pitch-angle scattering.

In measuring ion conductivity, the plasma density and temperature were chosen to be independent of ψ_t, and no electric fields were present. For each measurement, 360 test ions were launched on a given flux surface, ψ_{t_o}. These test particles were launched with a pitch-angle and energy distribution appropriate to an isotropic Maxwellian with temperature equal to that of the background ions, and were uniformly spaced poloidally. The particles were weighted according to the flux surface area each particle represented. Each test particle was followed for 30 msec, and after every 3 msec its energy and flux position were recorded. Thus, a test particle distribution function $f_i(X,V,t)$ was created, with X being defined by $X = \langle r_{sep} \rangle (\psi_t/\psi_{sep})^{1/2}$, where ψ_{sep} is the toroidal flux function at the separatrix and $\langle r_{sep} \rangle$ is the average radius of the separatrix.

The ion thermal conductivity can be determined from the test particle distribution by[4]

$$\chi_i = \frac{1/t \int dX \frac{1}{2}(X - X_o)^2 U_i(X,t)}{\int dX \; U_i(X,t)}$$

[IV-C-9]

where U_i is the distribution's kinetic energy density

$$U_i(x,t) = \int d^3v \; f_i(x,v,t) \; \tfrac{1}{2} m_i v^2 \qquad \text{[IV-C-10]}$$

Numerically, χ_i was found by performing a least-squares fit to

$$A + \chi_i t_j = y(t_j) \qquad \text{[IV-C-11]}$$

with

$$y(t_j) = \frac{\sum_k \tfrac{1}{2} (x_k - x_o)^2 U_{kj}}{\sum_k U_{kj}} \qquad \text{[IV-C-12]}$$

where the index j denotes the time and the index k denotes the spatial interval.

Although all test particles in a particular case are started on the same flux surface, there is a spreading of the test particle distribution because the collisionless drift surfaces differ from the flux surfaces. This spreading results in a statistical fluctuation in y(t) which occurs on a time scale comparable with the total tracking time (30 msec). The diffusive broadening should manifest itself in a linear dependence of y(t) on t. In fitting the data for y(t) to an expression of the form $A + B\,t^p$, I found $\langle p \rangle = 1.0 \pm .4$ for the cases of greatest broadening (the six highest density cases for the $R_o/a = 6$ torsatron). In the other runs, the statistical fluctuations are of the same order as the diffusive broadening, and the best fits

for p varied from 0 to 2. For these runs, the measurements for χ_i should be regarded as upper limits, since the distribution broadenings were caused both by diffusive and non-diffusive effects. This method for calculating X_i was tested in axisymmetric tokamaks and found to reproduce neoclassical results to within 10% throughout the banana and plateau regimes.

The values of y(t) for the χ_i versus density scans of the A and B reactors (see Table III-A-1), and for the χ_i versus T_i at constant fusion power scan of the A reactor, are given in Tables IV-C-1, 2, 3. Sample plots of y(t) for the B reactor scan are given in Figure IV-C-3.

Here is a description of how the errors in the χ_i measurements were estimated. The statistic χ^2 is a measure of the goodness of a fit and is defined as

$$\chi^2 = \sum_{i=1}^{N} \frac{1}{\sigma_i^2} \left(y_i - y(t_i)\right)^2 \qquad \text{[IV-C-13]}$$

where N = number of data points in fit

σ_i^2 = variance in i'th measurement

y_i = i'th data point

$y(t_i)$ = fitted values for i'th data point.

(Please note that I am now using the symbol χ for two different quantities; χ^2 is the measure of the goodness of fit, and χ_i is the ion thermal conductivity.) The probability $P(\chi^2, \nu)$ that any random set of N data points would yield a value of χ^2 larger than χ^2 is:[5]

y(t) [units of cm^2] for the scans of χ_i versus density for the $R_o/a = 12$ torsatron

density $[10^{20}/m^3]$	t [msec] 3	6	9	12	15	18	21	24	27	30
.005	83	123	164	160	182	170	147	169	187	178
.01	90	130	151	173	171	147	166	176	196	180
.02	164	241	280	277	292	286	219	237	274	268
.03	57	168	273	301	186	162	246	231	205	215
.05	49	53	86	155	202	192	194	221	184	158
.1	67	144	165	145	189	202	164	233	320	299
.2	73	175	208	216	266	258	224	294	284	258
.4	120	131	141	145	221	274	242	232	228	297
.6	68	145	191	207	241	249	241	347	294	286
1	55	62	110	100	92	102	120	160	158	219
2	67	86	100	86	113	119	150	189	159	203
3	53	69	98	103	192	171	103	163	177	184
5	68	70	77	124	127	139	154	166	194	185
8	49	67	111	148	113	192	170	138	176	162
13	45	58	81	101	124	108	97	142	131	153

Table IV-C-1

y(t) [units of cm^2] for the scans of χ_i versus density for the $R_o/a = 6$ torsatron

density $[10^{20}/m^3]$	t [msec]									
	3	6	9	12	15	18	21	24	27	30
.01	87	140	160	215	213	284	204	158	186	213
.02	187	219	244	289	205	302	320	317	226	275
.03	228	259	245	365	302	370	253	256	347	278
.06	85	160	202	205	199	217	199	261	303	256
.1	215	243	164	194	281	265	183	180	274	246
.2	187	144	147	222	176	162	237	181	353	303
.3	104	154	168	233	276	225	227	315	302	393
.6	103	115	204	340	370	288	383	429	431	371
1	203	271	251	321	359	354	417	345	358	346
2	108	126	175	203	223	356	383	457	368	440
3	61	149	231	198	186	275	276	308	407	524
6	212	159	191	169	245	301	336	352	404	383
10	62	142	180	179	215	235	296	328	345	480
20	101	119	159	251	304	391	430	479	462	550

Table IV-C-2

y(t) [units of cm^2] for the scans of χ_i versus T_i at constant plasma fusion power density

T_i [keV]	t [msec] 3	6	9	12	15	18	21	24	27	30
6	50	61	81	103	94	118	159	186	144	188
8	53	69	98	103	192	171	103	163	177	184
10	70	76	96	117	123	115	144	157	224	229
12	53	104	106	202	217	246	248	239	251	303
15	209	191	247	196	255	245	369	266	260	408
18	217	173	312	300	322	333	411	399	448	475
21	288	342	319	475	312	381	408	472	465	516

Table IV-C-3

Sample plots of y(t) versus time in the $R_o/a = 6$ torsatron.

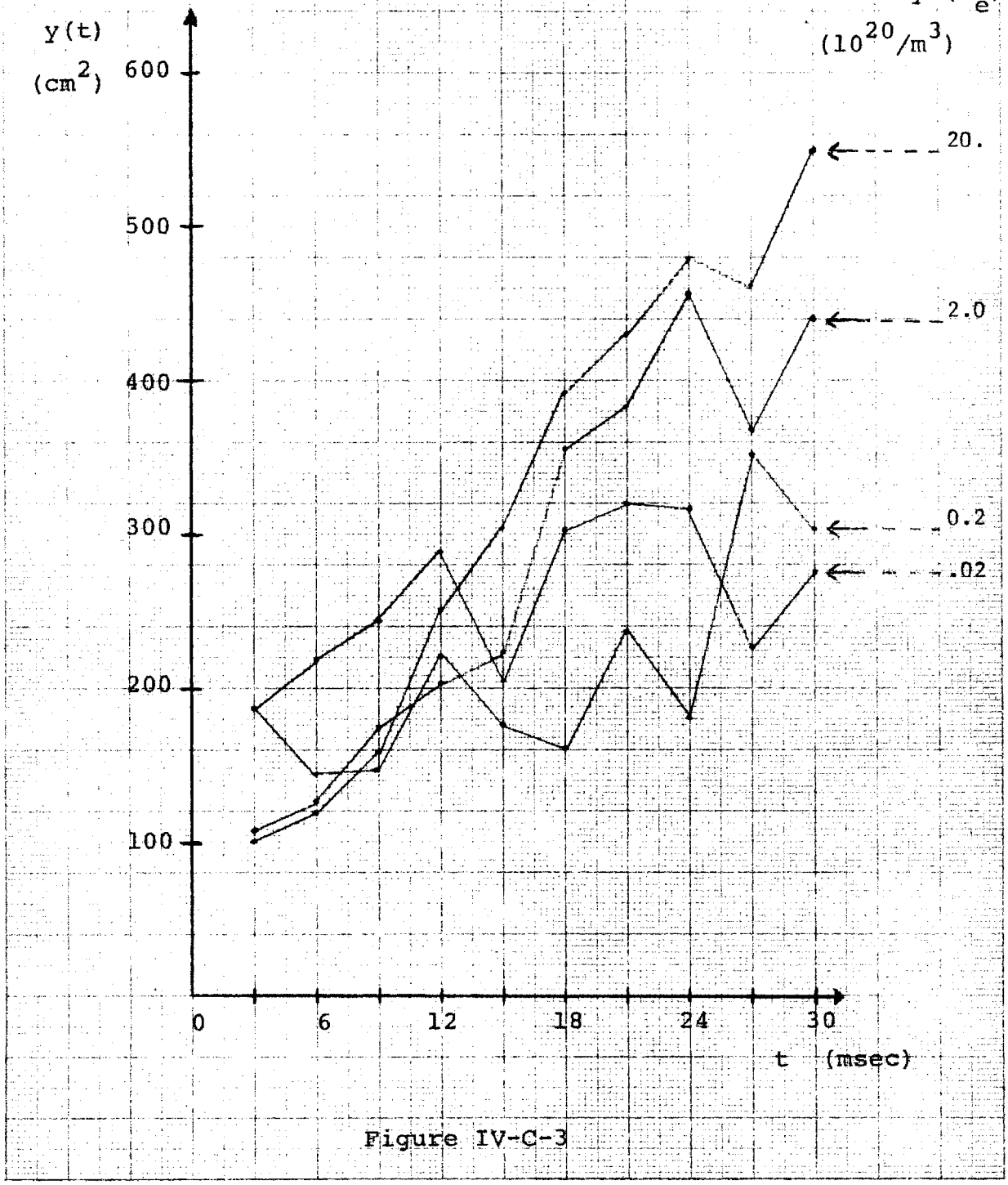

Figure IV-C-3

$$P(\chi^2, \nu) = \int_{\chi^2}^{\infty} \frac{z^{\frac{\nu-2}{2}} e^{-z/2}}{2^{\nu/2}\,\Gamma(\nu/2)}\, dz$$

$$= e^{-\chi^2/2} \sum_{m=0}^{\frac{1}{2}(\nu-2)} \frac{(\chi^2/2)^m}{m!}$$

[IV-C-14]

where $\nu \equiv$ number of degrees of freedom

= N-n-1 for a fit to a function with n coefficients plus one constant term.

For 10 data points, $\nu \equiv 8$ for a straight line fit. Choosing $P(\chi^2, \nu) = .3174$ (corresponding to a standard deviation confidence level on a χ^2 test), the associated value for χ^2 is 9.44.[6] Assuming equal uncertainties in the data points y_i, the variance σ^2 of the data points is determined. This variance is then used in a standard least squares fit to produce error estimates for the coefficients of the fit. This fit corresponds to a standard deviation confidence interval.

D. Measurements of χ_i and Comparisons with Ripple Transport Theory

In Figure IV-D-1 I plot the results of a scan of χ_i versus ν_{ii} for a large aspect ratio, reactor-sized torsatron with the following parameters:

R_o = 48 m	B_z(axis) = 5.5 T
a_c = 4 m	ψ_{sep} = 82.8 webers
ℓ = 3	$\langle r_{sep} \rangle$ = 2.1 m
N = 32	

Table IV-D-1

Both the test and background ions have a temperature of 8 keV, giving $\nu_{ii} = 125(n_i/10^{20})$ sec^{-1} for ions with mass 2.5 u. The test ions for this case were started at $\psi_{t_o} = .25\ \psi_{sep}$ where $\epsilon_t = 0.02$, $\epsilon_h = 0.015$, and $\iota = 1/q = 0.25$; ϵ_t is the toroidal modulation given by the local value of the inverse aspect ratio and ι is the local rotational transform. In the same figure I plot for comparison the theoretical ion thermal conductivity for an axisymmetric torus of otherwise identical parameters. Also plotted is a theoretical estimate for χ_i resulting from particles trapped in the helical magnetic wells. This estimate has been given for stellarators by Connor and Hastie[7] as:

$$\chi_i \simeq 11.6\ \epsilon_h^{3/2} \frac{\rho_i^2\ V_{th\,i}^2}{\nu_{ii}\ R^2} \qquad \text{[IV-D-1]}$$

where ϵ_h is the helical modulation of the field, ρ_i is the ion gyro-radius, $V_{th\,i} = \sqrt{2T_i/m_i}$ is the ion thermal velocity, R is the major radius, and ν_{ii} is the ion-ion collision frequency. This expression is presumed to be valid when the

collision frequency is small enough for particles to complete bounce orbits in the helical modulation but large enough that these trapped particles do not complete their poloidal drift orbits.

In Figure IV-D-2, I plot χ_i versus ν_{ii} for a torsatron with R_o = 24 meters, N = 16. In Figure IV-D-3a, I plot for the conditions of Figure IV-D-1, χ_i versus ψ_{t_o} for ν_{ii} = 370 sec^{-1}. In Figure IV-D-3b, the values of ε_t and ε_h are shown. Apparently, the thermal transport for fixed collisionality is not sensitive to the exact value of the modulation in the parameter range examined.

Figure IV-D-4 is a plot of ion thermal conductivity versus aspect ratio for R_o/a = 3, 6, and 12 (the same machines for which the alpha-particle confinement studies were done, see Table III-A-1). Also plotted is the best fit to the equation $C_o(a/R_o) = \chi_i$, given the observed points and their associated error bars. In Figures IV-D-5 and IV-D-6, the helical and toroidal ripple in these machines are plotted versus the flux coordinate.

The principal result of these computations is that the predicted $1/\nu$ behavior does <u>not</u> occur; instead ion thermal conductivity is independent of collision frequency over a wide range of collisionality. This transport coefficient is approximately equal to that derived for the neoclassical axisymmetric plateau regime, and maintains this value over at least two orders of magnitude in density (or collision frequency) variation.

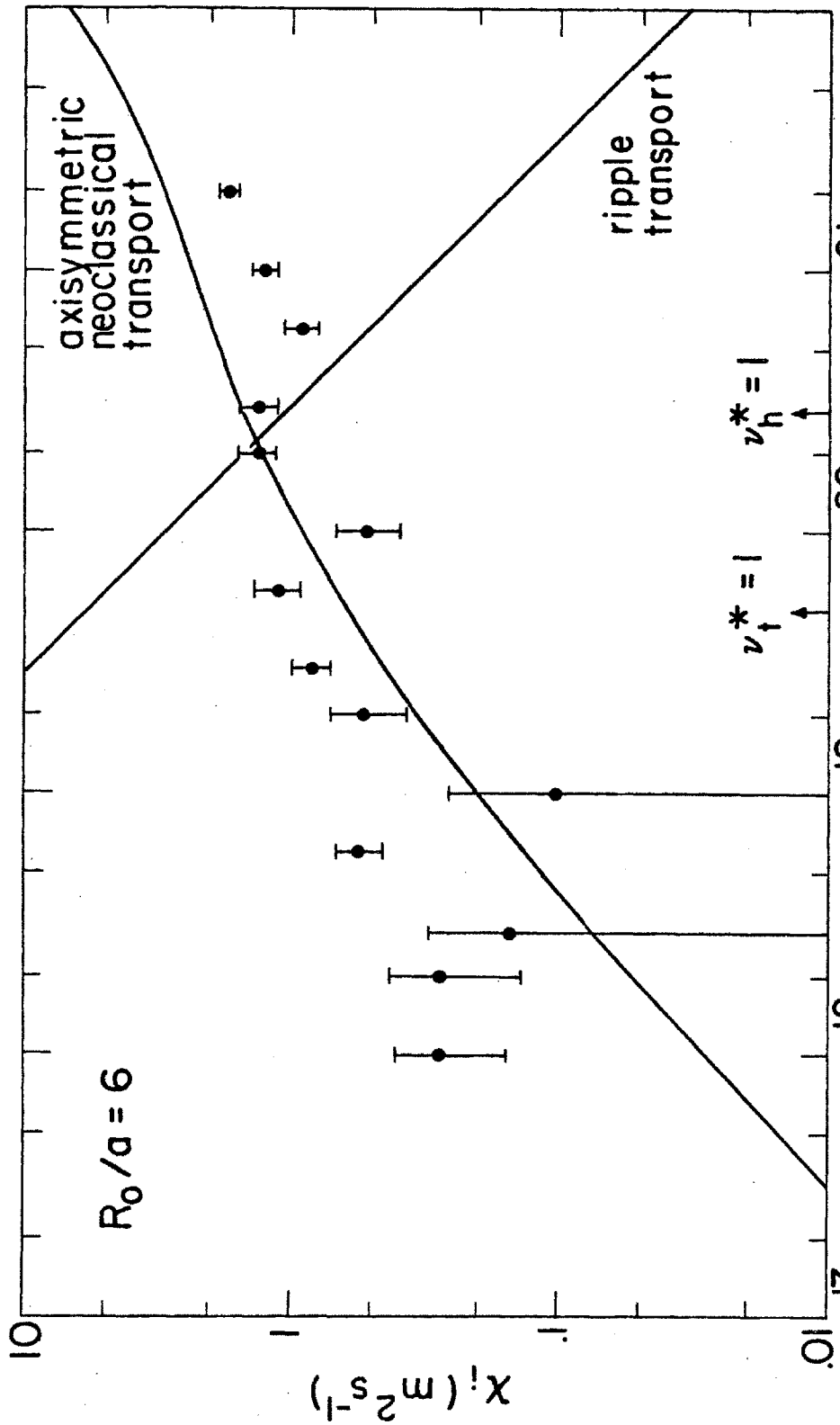
axisymmetric
neoclassical
transport
ripple
transport
$R_o/a = 6$
$\nu_t^* = 1$
$\nu_h^* = 1$
$\chi_i\ (m^2 s^{-1})$
density (m^{-3})
10
1
.1
.01
10^{17}
10^{18}
10^{19}
10^{20}
10^{21}

Figure IV-D-1

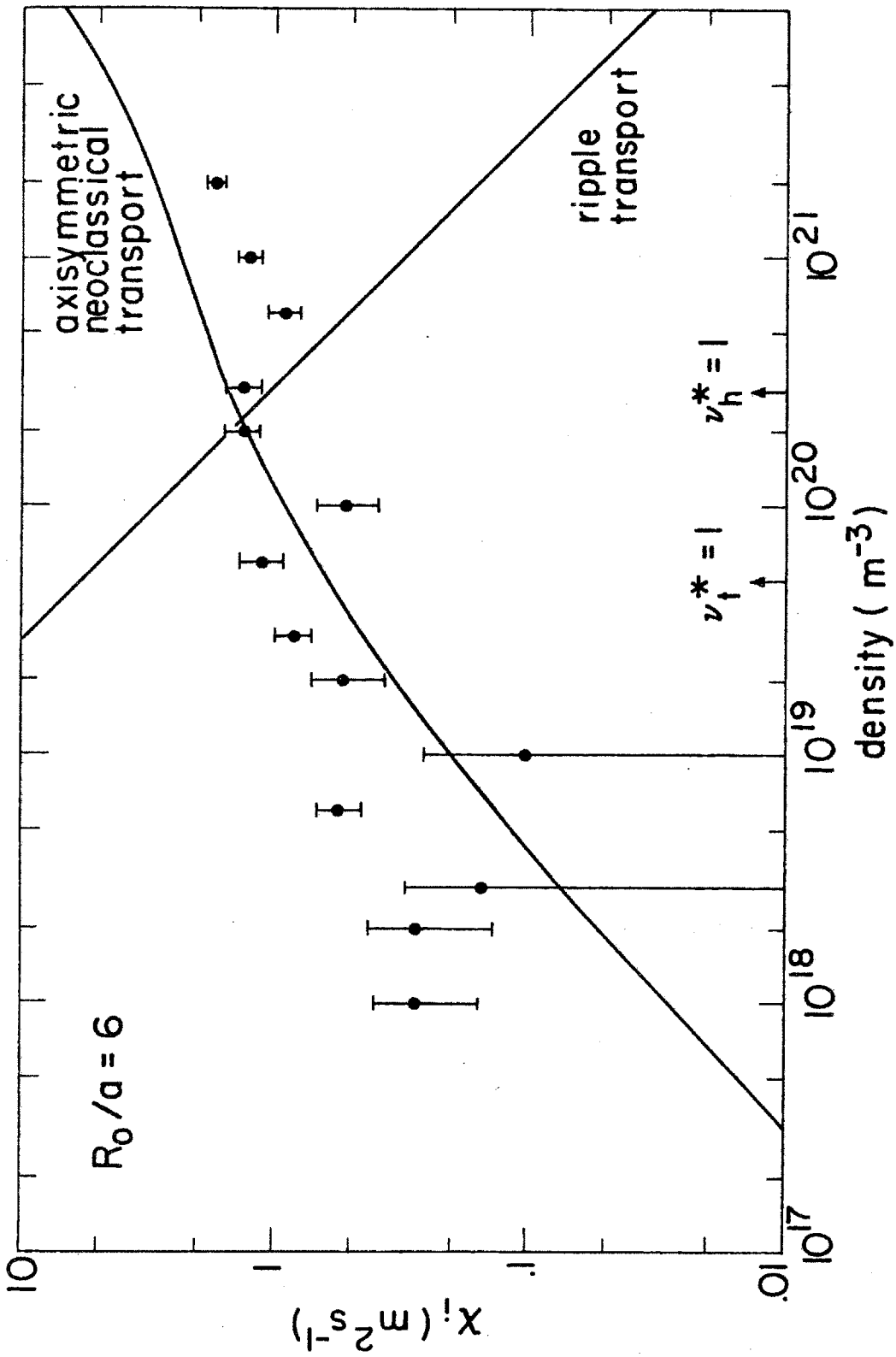
axisymmetric
neoclassical
transport
ripple
transport
$R_0/a = 6$
$\nu_t^* = 1$
$\nu_h^* = 1$
$\chi_i\ (m^2 s^{-1})$
density (m^{-3})
10
1
.1
.01
10^{17}
10^{18}
10^{19}
10^{20}
10^{21}

Figure IV-D-2

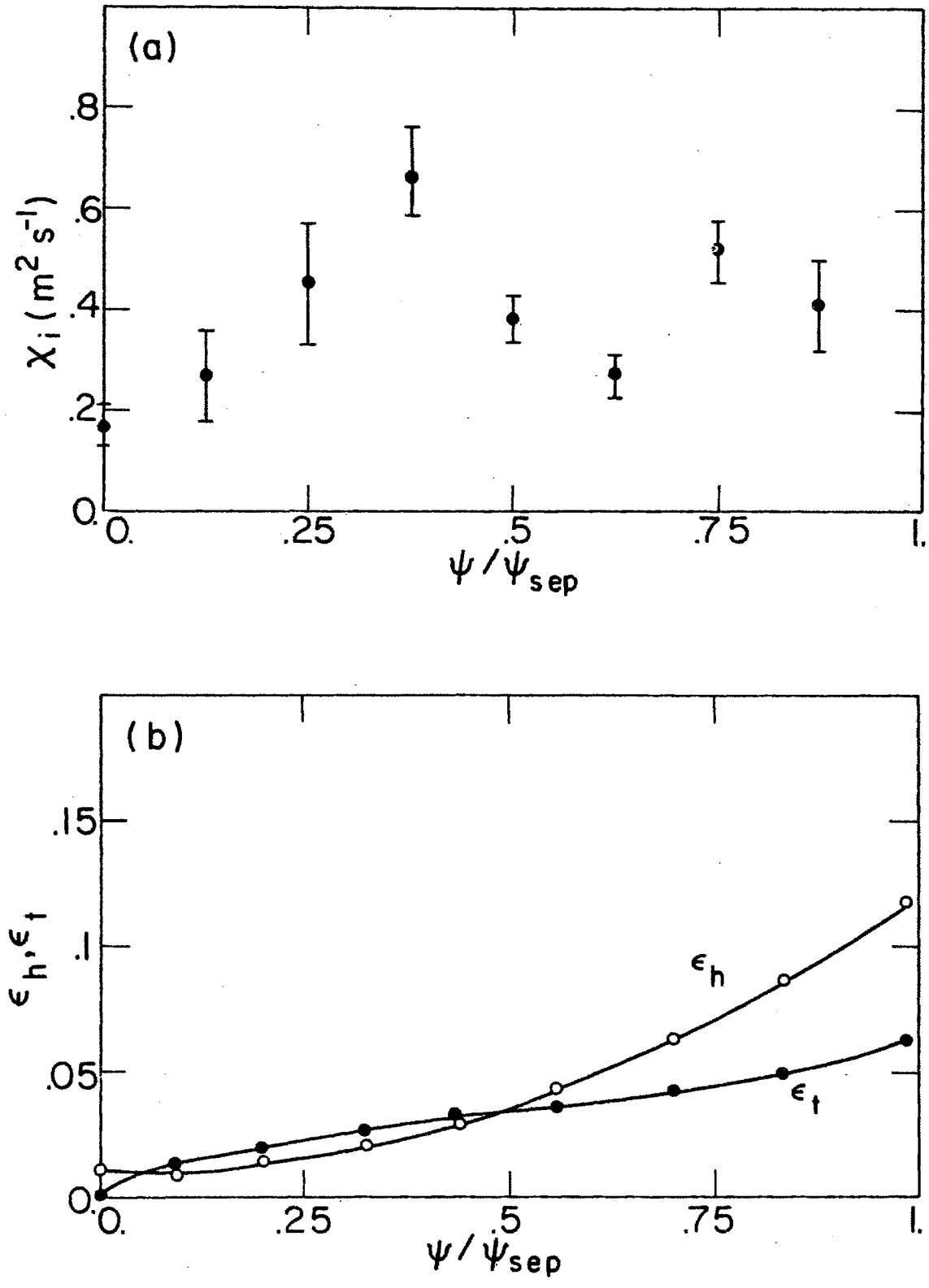
(a)
.8
.6
.4
.2
0.
χ_i ($m^2 s^{-1}$)
0.
.25
.5
.75
1.
ψ / ψ_{sep}
(b)
.15
.1
.05
0.
ϵ_h, ϵ_t
ϵ_h
ϵ_t
0.
.25
.5
.75
1.
ψ / ψ_{sep}

Figure IV-D-3

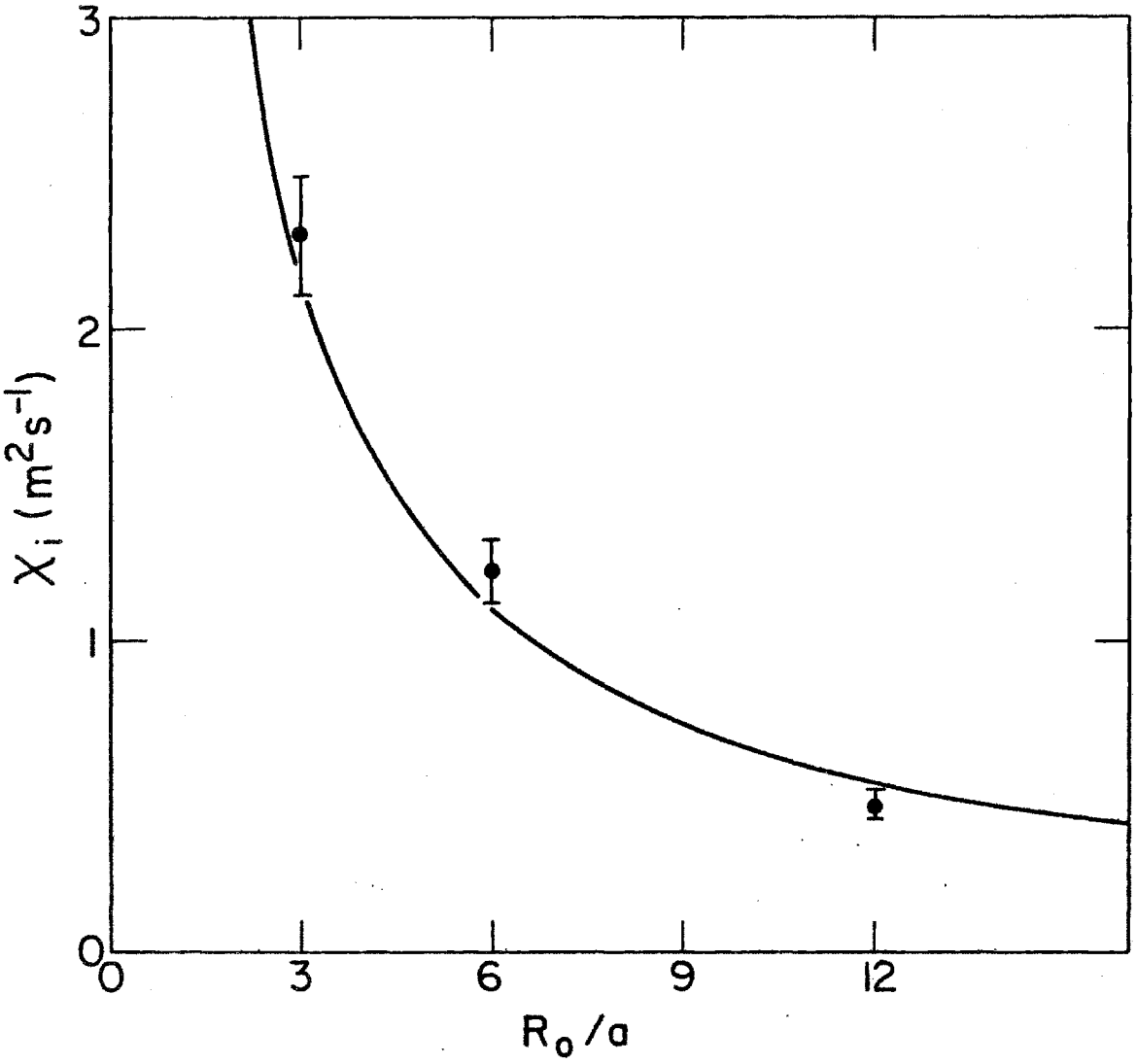

Figure IV-D-4

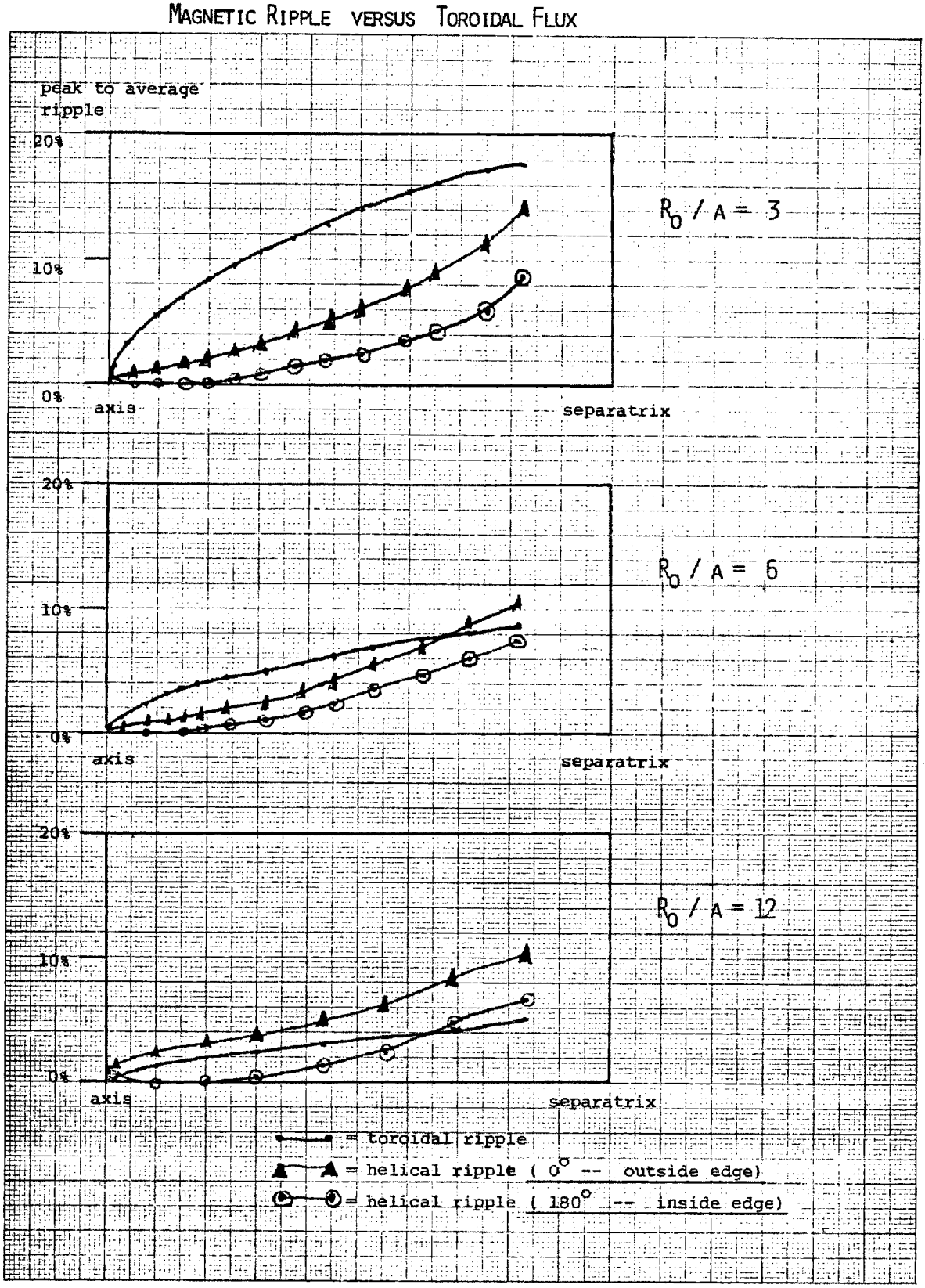
MAGNETIC RIPPLE VERSUS TOROIDAL FLUX
peak to average ripple
20%
10%
0%
axis
separatrix
$R_0 / A = 3$
20%
10%
0%
axis
separatrix
$R_0 / A = 6$
20%
10%
0%
axis
separatrix
$R_0 / A = 12$
= toroidal ripple
= helical ripple (0° -- outside edge)
= helical ripple (180° -- inside edge)

Figure IV-D-5

Magnetic Ripple versus Toroidal Flux (Fourier components)

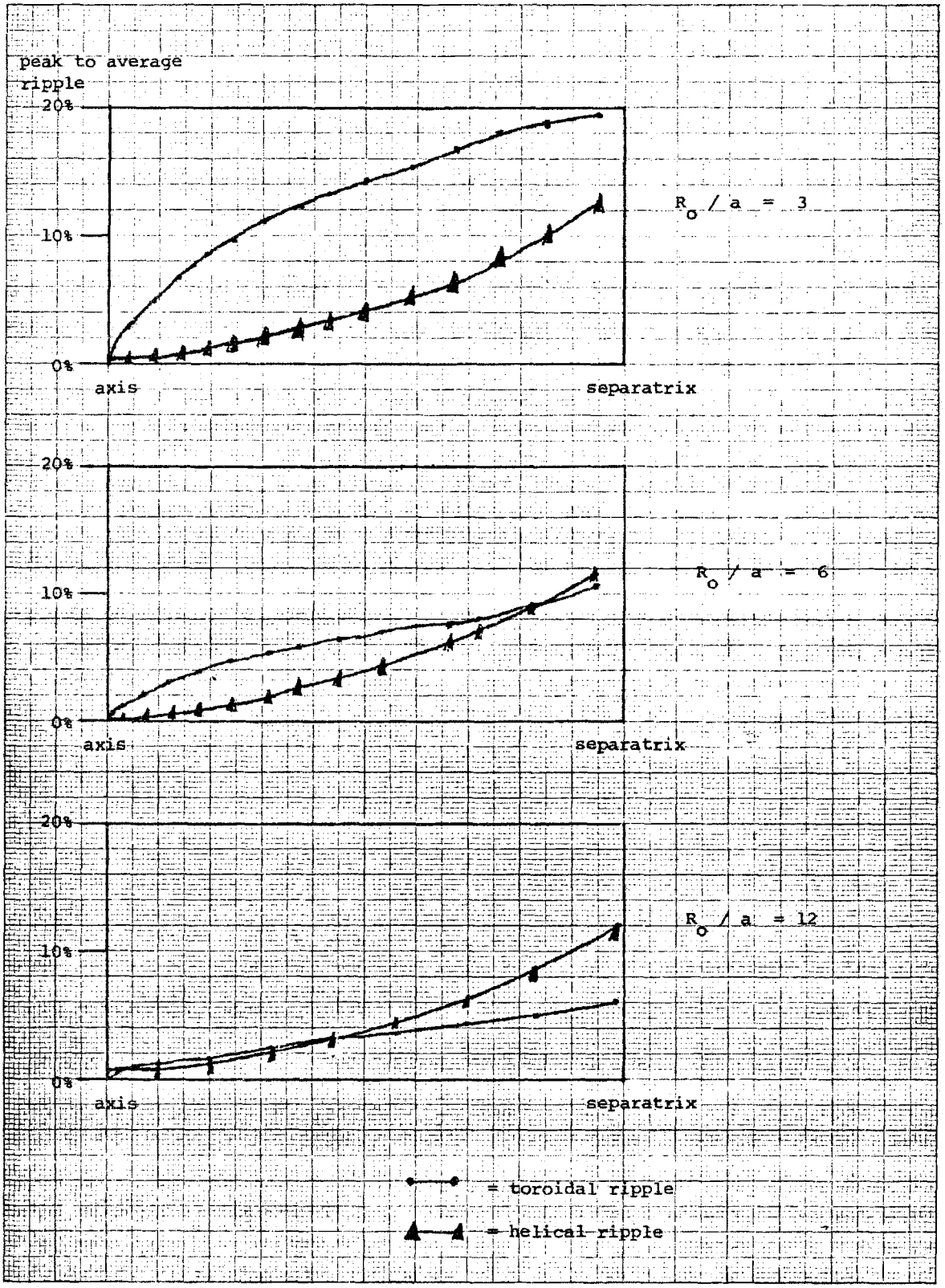

Figure IV-D-6

It appears that ripple transport theory is not applicable to the torsatron geometry. The usual calculation of transport due to ripple trapping relies on the assumption that a significant fraction ($\sim\varepsilon_h^{1/2}$) of the particles in the system are trapped in the helical ripples, and that the deviation of their collisionless drift orbits from their initial flux surface positions is determined primarily by the vertical drift caused by the toroidal 1/R magnetic field gradient. The $\varepsilon_h^{1/2}$ dependence of the trapped particle population originates from the relation between the maximum mirroring angle in velocity space and the field modulation:

$$\sin^2\theta_m = \frac{v_{\perp o}^2}{v_o^2} \cong \frac{B_o}{B_{max}} \cong 1 - \varepsilon_h \qquad \text{[IV-D-2]}$$

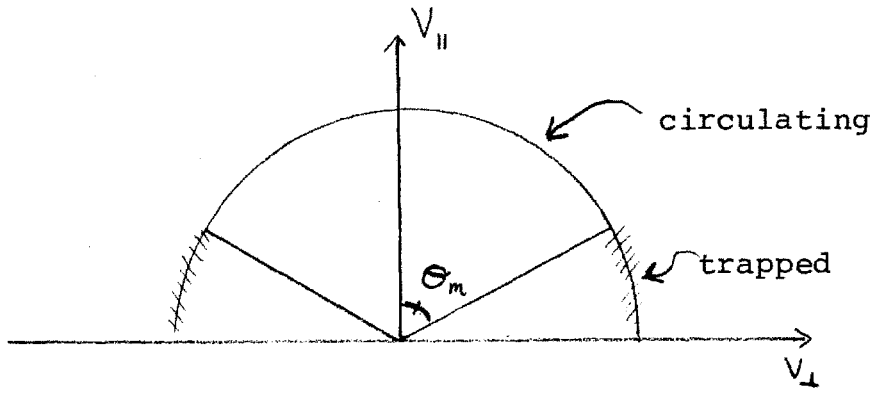

Figure IV-D-7

$$\frac{n_{trapped}}{n_{total}} \cong \cos\theta_m \sim \sqrt{\varepsilon_h} \qquad \text{[IV-D-3]}$$

Detailed calculations of collisionless particle orbits in a wide variety of helical toroidal configurations, however, indicate that this model is invalid (see details of particle orbits in Chapter II). As in axisymmetric systems, most particles are never reflected, make small excursions from flux surfaces, and do not contribute significantly to transport in low to moderate collisionality regimes. In helical toroidal systems, the rest of the particles undergo very complex motions. They can make frequent transitions among quasi-circulating ("blocked"), tokamak-like banana, and helically trapped orbits.[8] Even for large aspect ratios ($\varepsilon_h > \varepsilon_t$), the contribution from particles with simple, helically trapped orbits is negligible. The transition particles comprise a fraction of the total which is the larger of $\sqrt{\varepsilon_t}$ or $\sqrt{\varepsilon_h}$. Their orbits do not conserve the adiabatic invariant J, because of the transitions between trapped and quasi-circulating motion. The "plateau" character of the thermal conductivity is demonstrated by the 1/R dependence seen in Figure IV-D-4. This is consistent with a transport model in which χ_i scales as $\varepsilon_t \varepsilon_h$, the transport resulting from an orbit resonance between the motion in the helical modulation and the bounce motion in the toroidal modulation of the field.[9, 10] A model developed by Miyamoto[9] leads to a transport coefficient which is independent of collision frequency ($D_h \sim \varepsilon_t \varepsilon_h \, T / B$)[9] for $\varepsilon_t >> \varepsilon_h$ and $\nu \cong \varepsilon_t \varepsilon_h \, T / (eB r^2)$. In this model, the drift is dominated by the toroidal curvature,

and the step length is $V_\perp/\nu^{eff} = V_\perp \varepsilon_h/\nu$.

I suggest that neoclassical ripple transport was not observed because it is based on a toroidal ordering of the distribution function f in a series of powers in m/e, using the periodic function $X(\phi) = \tilde{X} + \bar{X}$, where $\partial\bar{X}/\partial\phi = 0$ and $\int \tilde{X}\, d\phi = 0$.[11] Helical ripple is usually treated as a perturbation on the toroidal ordering of f. In the torsatron case, where ε_t is of the same order as ε_h, this toroidal ordering of f is inappropriate, hence the deviation between theory and observation.

E. Measurement of χ_i and Analysis of Torsatron Ignition Criteria

The results of the previous section are of particular importance for plasma conditions appropriate to fusion reactors. The $1/\nu_{ii}$ dependence of the ripple transport coefficients has led recent torsatron reactor design studies to concentrate on low temperature, high density plasma regimes where collisionality is large and χ_i acceptably small.[12, 13] Recent experimental results have indicated, though, that the $1/\nu_{ii}$ behavior may not be occurring.[14, 15] In order to compare the ignition criteria at various plasma temperatures with the scaling of χ_i, a number of χ_i measurements were made with varying plasma temperature, but with a constant fusion power density of 3.76 MW/m^3. This value is consistent with the axis values of n_e and T_i used in the α-particle energy deposition studies described in Chapter III ($n_e = 3 \cdot 10^{20}/m^3$, $T_i = 8$ keV), and would result in an

acceptable first wall loading of 1 to 2 MW/m^2 of primary fusion power (the exact value depending on the profile shapes). For the diffusion runs, flat profiles were assumed for n and T. The results are shown in Figure IV-E-1. The energy confinement times at the various plasma temperatures were calculated by

$$\tau_E = \langle r_{sep} \rangle^2 / 4 \chi_i \qquad \text{[IV-E-1]}$$

where $\langle r_{sep} \rangle$ = 2.1 meters for the A machine (R_o/a = 12).

The energy confinement time necessary for ignition was found by a power balance equation:

$$\tau_{ig} = \frac{\text{energy contained in plasma}}{\text{source power - (non-conductive power loss)}}$$

$$= \frac{\frac{3}{2} \int \sum_\alpha n_\alpha T_\alpha \, d\,\text{Vol}}{(\%\ \alpha\ \text{confinement}) \cdot \alpha_{power} - W_x} \qquad \text{[IV-E-2]}$$

where W_x is the bremsstrahlung radiation loss calculated by[16]

$$W_x = 4.8 \cdot 10^{-37} n_i n_e \sqrt{T_e(\text{keV})} \quad \text{watts/m}^3 \qquad \text{[IV-E-3]}$$

and

$$\alpha_{power} = Q_i \, n_D \, n_T \, \langle \sigma v \rangle_{DT} \quad \text{plasma volume} \qquad \text{[IV-E-4]}$$

with Q_i = 3.5 MeV/fusion reaction.

The results are shown in Table IV-E-1. The data for τ_E/τ_{ig} indicates that, for T_i = 8 - 20 keV and $\langle a_p \rangle$ = 2.1 m,

Constant fusion power plasma

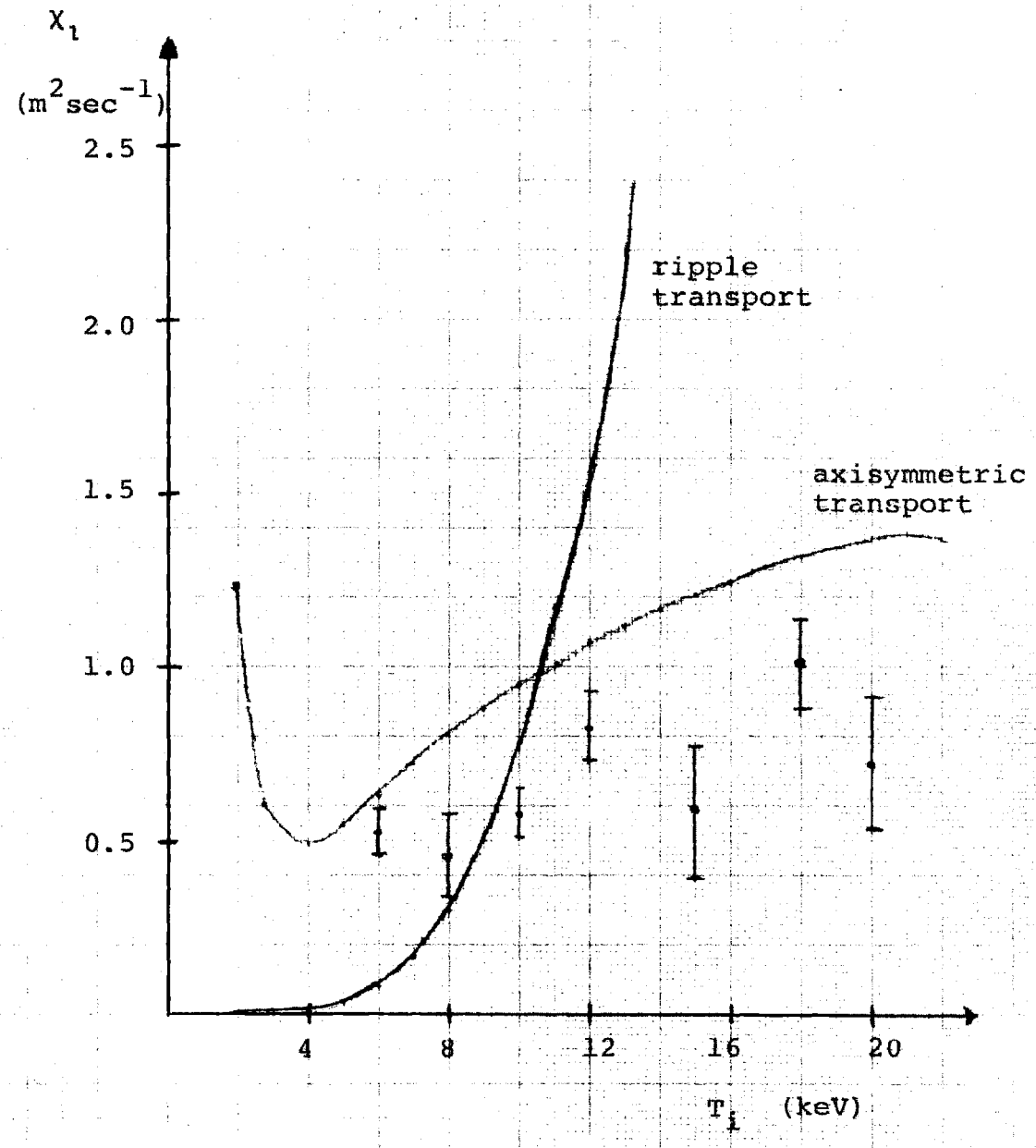

Figure IV-E-1

T_i (keV)	n_i (m^{-3})	ion pressure (tesla^2)	τ_{ig} (sec)	χ_i (m^2/s)	τ_E (sec)	τ_E/τ_{ig}
6	$4.70 \cdot 10^{20}$	1.135	2.79	.51	2.15	.77
8	$3.00 \cdot 10^{20}$	.966	1.85	.46	2.39	1.29
10	$2.22 \cdot 10^{20}$	.892	1.59	.58	1.90	1.19
12	$1.82 \cdot 10^{20}$	.878	1.52	.83	1.33	.87
15	$1.42 \cdot 10^{20}$	.857	1.45	.58	1.90	1.31
18	$1.22 \cdot 10^{20}$	.884	1.48	1.02	1.07	.73
21	$1.09 \cdot 10^{20}$	.918	1.53	.71	1.56	1.02

Table IV-E-1

Comparison of ignition and energy containment times at varying plasma temperatures for an $R_o/a = 12$ torsatron.

the energy containment time in an $R_o/a = 12$ torsatron will approach or exceed the ignition times. The plot of the neoclassical ripple transport in Figure IV-E-1 again clearly demonstrates that χ_i does not show the adverse $1/\nu_{ii}$ scaling predicted by this theory. This implies that, in moderate aspect ratio helical systems, the ion temperature may be raised to 15 keV (the value for minimum $n\tau$ at ignition) without suffering from increased loss due to ripple transport.

Equation IV-E-2 will be valid only when the non-diffusive power loss is limited to bremsstrahlung. Power loss may also occur from ions scattering into unconfined orbits. This is potentially a very detrimental loss term. If loss cones in velocity space exist near the magnetic axis, the particle containment time would be on the order of a scattering time. In addition, the resulting non-Maxwellian nature of the plasma might excite micro-instabilities and further decrease plasma containment. The resulting power loss would probably exceed the source power from the α-particles.

From Figure IV-B-1, we see that there are no loss regions in phase space for the $R_o/a = 12$ torsatron. This fact was confirmed by the diffusion runs. During the 29 runs reported in this chapter in the $R_o/a = 12$ torsatron, only one particle (out of 10440) managed to escape during its 30 msec track. During the 14 runs in the $R_o/a = 6$ torsatron (see Figure IV-D-2), only 18 particles escaped,

which corresponds to an e folding time of 8.38 sec for the test ion distribution. The e folding time τ was determined by:

$$n(t) = n_o e^{-t/\tau} \qquad \text{[IV-E-5]}$$

The observed ion losses occurred uniformly during the 30 msec tracking period, consistent with

$$\frac{dn}{dt} \cong -\frac{n_o}{\tau} = \text{constant (for } t << \tau) \qquad \text{[IV-E-6]}$$

The principal result of these computations is that the energy transport due to loss cones is negligible in $R_o/a \gtrsim 6$ torsatrons. For torsatrons of smaller aspect ratios, this is not the case. Figure IV-B-1 shows sizable loss cones existing near the magnetic axis for the $R_o/a = 3$ machine. The single diffusion run done for this machine had 20 particles out of 360 escape during 30 msec of tracking. This results in an e folding time of .52 sec for the density distribution, on the same order as the energy confinement time due to diffusive spreading ($\tau_E = .47$ sec). This indicates that the low aspect ratio torsatrons cannot be ignited. In addition to suffering from the observed $1/R_o$ increase in χ_i, energy confinement is further degraded due to particles scattering into unconfined orbits.

Figure IV-B-1 indicates that loss cones near the magnetic axis are diminished in the R_o/a torsatron by a

high field. A diffusion run made in the high field machine confirmed this. With the test particle distribution launched at $\psi_{t_o} = .25\ \psi_t$(separatrix), no particles were lost during the high field (B_{z_o} = 10.1 tesla) compared with 20 for the normal field. The observed value of χ_i was 1.22 ± .05 for B_{z_o} = 10.1 tesla, compared to χ_i = 2.31 ± 0.2 for B_{z_o} = 5.05 tesla. This is suggestive of a 1/B scaling for χ_i, another characteristic of resonance diffusion.[9] (Please note that I presented Miyamoto's diffusion coefficient in section D only to illustrate the characteristic scalings of diffusion based on a resonance between helical and toroidal ripples. I am <u>not</u> comparing Miyamoto's results directly with my observations, since Miyamoto's basic assumption that $\varepsilon_t >> \varepsilon_h$ is not valid for torsatrons with moderate aspect ratio.)

F. Conclusions

A detailed optimization of a torsatron reactor design is well beyond the scope of this thesis. It would involve a complex interaction of the engineering constraints (power balance, first wall loading, total reactor size) with the numerous design parameters (plasma radius, aspect ratio, coil pitch length and winding law, field strength on axis, etc.). Still, I believe the choices made in this thesis for the fixed design parameters of the torsatron reactors were reasonable, and that my results allow a number of conclusions to be drawn concerning the viability of the torsatron as a

power reactor.

The numerical measurements of the ion thermal conductivity show the presence of a plateau regime extending over two orders of magnitude in collision frequency. The value of χ_i is approximately equal to the neoclassical plateau value for an equivalent torus without helical modulation. This plateau regime, plus the observed 1/R and 1/B scaling of χ_i, are characteristic of diffusion resulting from an orbit resonance between the motion in the helical modulation and the bounce motion in the toroidal modulation of the field.[9, 10]

I suggest two reasons why neoclassical ripple transport was not observed in the torsatron fields. First, the toroidal ordering of the distribution function in the neoclassical calculation is inappropriate to the torsatron magnetic geometry, because the helical and toroidal modulations in the torsatron's field are of the same order. Second, the observed orbits of the trapped particles within the torsatron (which are the fraction of the population that contribute most to the diffusion) differ markedly from the trapped orbit characteristics assumed by neoclassical theory. Neoclassical ripple theory assumes that a significant fraction ($\sim\sqrt{\varepsilon_h}$) of the particles are trapped in the helical ripples of the field. The observed orbits indicate that this assumption is incorrect. The trapped particles were observed to make frequent transitions from ripple trapped to tokamak-like banana to quasi-circulating motion

in vacuum fields. Their motion does not conserve the second adiabatic invariant J, which is assumed conserved in neoclassical theory.

An analysis of the power balance of a torsatron reactor, based on the observed plateau character of the ion thermal conductivity, indicates that an $R_o/a = 12$ torsatron can ignite at moderate density and temperature ($n_e \cong 1.5 \cdot 10^{20}/m^3$, $T_i \cong 10 - 20$ keV). For the reactor sized torsatron described in Table IV-D-1, the power deposited in the plasma by thermalizing α-particles (42.1 MW/module) was sufficient to balance the bremsstrahlung power loss ($\sim$ 10 - 15 MW/module) and the diffusive power loss due to the ion thermal conductivity. The power loss due to particles scattering into unconfined orbits was found to be negligible for an $R_o/a = 12$ torsatron, about 15 percent of the diffusive power loss for an $R_o/a = 6$ torsatron, and approximately equal to the diffusive power loss for an $R_o/a = 3$ torsatron. The observed 1/R scaling of χ_i suggests that, for $\langle a_p \rangle = 2.1$ m and $B_{z_o} = 5$ tesla, the minimum aspect ratio for ignition is $\sim$ 10. In this aspect ratio regime, the power loss due to ions scattering into unconfined orbits was found to be much less than the bremsstrahlung power loss. The diffusion measurements also point to a 1/B scaling of χ_i, which suggests that the minimum aspect ratio for ignition might be lower if the magnetic field strength of the reactor were increased, assuming that the new values for plasma β and/or wall loading were acceptable.

References, Chapter IV

1. T. E. Stringer, "Neo-Classical Theory for Non-Axisymmetric Systems," Third International Symposium on Toroidal Plasma Confinement , Garching, 1973.

2. J. W. Conner and R. J. Hastie, "Neo-classical Diffusion in an $\ell = 3$ Stellarator," Physics of Fluids, 17, 1 (1974), p. 114.

3. S. Ichimaru, Basic Principles of Plasma Physics, W. A. Benjamin, Inc. (1973), p. 246.

4. K. Molvig (M.I.T. Plasma Fusion Center), personal communication.

5. P. R. Bevington, Data Reduction and Error Analysis for the Physical Sciences, McGraw-Hill Book Company (1969), p. 202.

6. G. W. Snedecor and W. G. Cochran, Statistical Methods, The Iowa State University Press (1967), p. 550.

7. J. W. Conner and R. J. Hastie, op. cit., p. 122.

8. A. Gibson and J. B. Taylor, "Single Particle Motion in Toroidal Stellerator Fields," Physics of Fluids, 10 (1967), p. 2653.

9. K. Miyamoto, "Diffusion of Plasma Confined in Stellarator with $\varepsilon_t > \varepsilon_h$," Physics of Fluids, 17, 7 (1974), p. 1476.

10. R. H. Cohen, "Orbital Resonances in Non-axisymmetric Mirror Machines," Comments Plasma Phys. Cont. Fusion, 4 (1979), p. 157.

11. E. A. Frieman, "Collisional Diffusion in Nonaxisymmetric Toroidal Systems," Physics of Fluids, 13, 2 (1970), p. 490.

12. A. V. Georgievskii, et al., "Characteristics of a Hypothetical Thermonuclear Stellarator Reactor in the 'Plateau' Regime," CTO/1299 (Culham Translation of KhTFI76-38), (1976).

13. A. Iiyoshi and K. Uo, "Helotron as a Steady State Fusion Reactor," IAEA-CN-33/G-4, Conference on Plasma Physics and Controlled Nuclear Fusion (1974).

14. D. W. Atkinson, et al., "Heating and Confinement in the Cleo Stellarator," CLM-P-505 (1977).

15. V. S. Voltsenya, et al., "Confinement of a Low Collision Frequency Plasma in the 'Saturn I' Torsatron," Third International Symposium on Toroidal Plasma Confinement, Garching, 1973.

16. D. J. Rose, Plasmas and Controlled Fusion, The M.I.T. Press, Cambridge, Mass. (1973), p. 233.

17. A.H. Boozer and G. Kuo-Petravic, "Monte Carlo Evaluation of Transport Coefficients," PPPL, 1703, (1980).

Chapter V. SUMMARY

In this thesis I studied high-energy particle orbits and energy diffusion in reactor sized torsatrons. In particular, I investigated the orbit characteristics of 3.5 MeV α-particles, the power deposition profiles of thermalizing α-particle distributions, and the characteristics of the plasma's ion thermal conductivity. The results were used to estimate a minimum aspect ratio at which power deposited in the plasma by thermalizing α-particles would balance power losses due to bremsstrahlung, escaping particles, and ion thermal conductivity. I present here an abbreviated collection of these results and conclusions.

For particles orbiting in helical, cylindrical magnetic fields, energy and helical momentum are absolute invariants of motion. For particle orbits with $\rho_\ell << a_{coil}$ and $\rho_\ell << L_B$ (the local field curvature), the magnetic moment μ is an adiabatic invariant of motion. The invariance of these three quantities limits the radial excursion of a particle to approximately a Larmor radius (ρ_ℓ). This indicates that the large radial excursions observed for trapped particles in helical, toroidal fields were not due solely to the presence of helical ripple, but were the result of orbit resonances between the motion in the helical modulation and the bounce motion in the toroidal modulation of the field.

The analysis of orbit characteristics in helical, toroidal magnetic fields was done by examining numerical tracks of guiding-center orbits. These tracks showed that the particles may be grouped into two general classes, well circulating particles and blocked particles. Well circulating particles are in general confined particles; their orbits are characterized by periodic motion on well defined drift surfaces. Blocked particles, on the other hand, exhibit more complex and non-periodic motion, and their general confinement is dependent on the toroidal curvature of the magnetic field. Blocked α-particles were found to be well confined in a reactor sized torsatron with $R_o/a = 12$, moderately confined with $R_o/a = 6$, and poorly confined with $R_o/a = 3$. This led to an overall percentage power confinement (from thermalizing α-particles) of 99.4% for a torsatron reactor with $R_o/a = 12$, 90.3% with $R_o/a = 6$, and 65% with $R_o/a = 3$. By raising the axis field from 5.05 tesla to 10.1 tesla in the $R_o/a = 3$ machine, the overall percentage power confinement was increased to 70.1%.

The α-particle orbits were found to be insensitive to moderate potential differences between the axis and separatrix regions of the plasma (0 - 10 kV). Above 10 kV, a positive charging of the axis region aided the confinement of blocked α-particles. These particles, when leaving the axis region, would pick up parallel energy from the decreasing potential and be less affected by the magnetic field modulations. Per contra, a negatively charged axis resulted

in blocked particles losing parallel energy near the separatrix region, which led to larger flux surface excursions, and in some cases, particle loss.

Numerical determination of the ion thermal conductivity showed the presence of a plateau regime extending over two orders of magnitude in collision frequency. The theoretically predicted adverse $1/\nu$ scaling of χ_i due to ripple trapping was not seen. On the contrary, χ_i was approximately equal to the neoclassical plateau value for an equivalent torus without helical modulation. These results indicate that ripple transport theory is not applicable to the torsatron geometry. The usual calculation of transport due to ripple trapping relies on the assumption that a significant fraction ($\sim\sqrt{\varepsilon_h}$) of the particles in the system are trapped in the magnetic ripples, and that the deviations of their collisionless drift orbits from their initial flux surface positions are determined primarily by the vertical drift caused by the toroidal 1/R magnetic field gradient. However, an analysis of blocked particle orbits shows that this assumption does not hold. The orbits of the blocked particles are complex. These particles can make frequent transitions between quasi-circulating, tokamak-like banana, and helically trapped orbits. The fraction of particles with simple, helically trapped orbits is negligible.

An analysis of the ignition criteria of a torsatron reactor, based on the observed plateau character of the ion termal conductivity, indicates that an $R_o/a = 12$ torsatron

can be ignited at moderate density and temperature ($n_e \tilde{=} 1.5 \cdot 10^{20}/m^3$, $T_i \tilde{=} 10 \rightarrow 20$ keV). In this machine, the power deposited in the plasma by thermalizing α-particles (42.1 MW/module) was sufficient to balance the bremsstrahlung power loss (~10 - 15 MW/module), the power loss due to particles scattering into unconfined orbits (<< 1 MW/module), and the diffusive power loss due to the ion thermal conductivity (20 - 30 MW/module). The diffusive power loss was found to scale with 1/R. The power loss due to particles scattering into unconfined orbits was found to be negligible for an $R_o/a = 12$ torsatron, about 15% of the diffusive power loss for an $R_o/a = 6$ torsatron, and approximately equal to the diffusive power loss for an $R_o/a = 3$ torsatron. These results indicate that moderate aspect ratio torsatrons with the design parameters chosen for this study ($B_{Z_o} \hat{=} 5$ tesla, $\langle a_p \rangle = 2.1$ meters, $a_c = 4$ meters) can meet or exceed ignition requirements. Power losses due to ions scattering into unconfined orbits are negligible, and the power deposited by the well confined, thermalizing α-particles can balance bremsstrahlung and diffusive power losses. The 1/B scaling of the ion thermal conductivity and diffusive power loss also suggests that torsatrons of lower aspect ratio might also be ignitable if a higher axis field strength ($\sim$ 10 tesla) were used.

Appendix A

This appendix describes the calculation of $\underline{B}$ on a three-dimensional grid inside a torsatron reactor. In particular, it describes:

1) the mathematics of the constant-pitch winding law
2) a method to approximate helical, toroidal windings with straight line segments
3) the calculation of $\underline{B}$ from a line segment
4) a method of constructing the three-dimensional grid which allows finite poloidal thickness of the coils with very little extra computation time.

The pitch angle α of the torsatron's helical windings is defined by the equation:

$$\tan \alpha = \frac{a}{R_o + a \cos(\theta)} \frac{d\theta}{d\phi} \qquad [A\text{-}1]$$

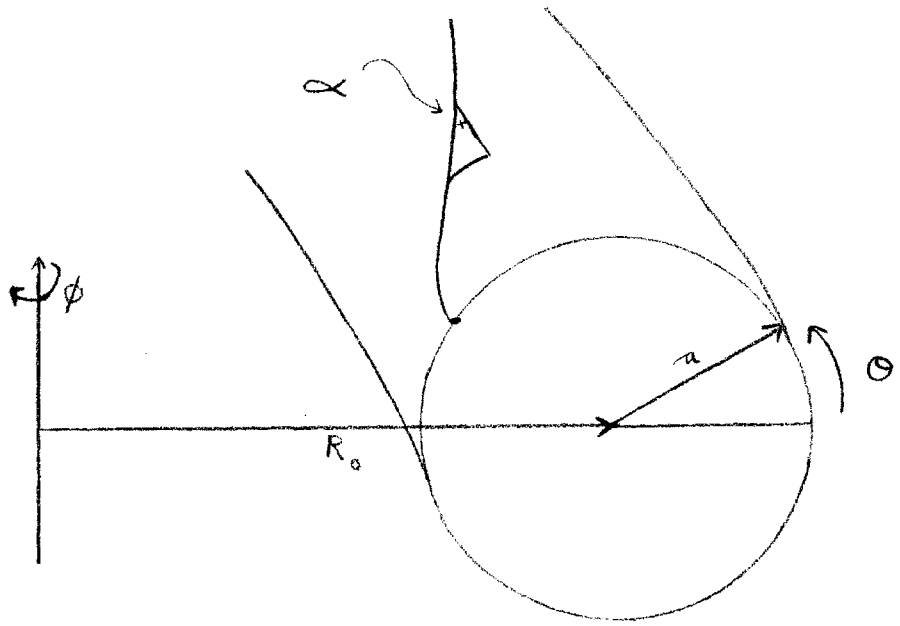

Figure A-1

Two common winding laws involve keeping $d\theta/d\phi$ constant (sinusoidal windings) or the angle α constant (constant pitch windings). For this study, the constant pitch winding law was arbitrarily chosen. With tan α a constant, an equation relating the θ coil position to the ϕ position may be derived. I start by solving for tan α.

Since the winding makes $1/N_t$ toroidal turns for one poloidal turn,

$$\tan \alpha = \frac{\int_0^{2\pi} \frac{a \, d\theta}{R_o + a \cos\theta}}{\int_0^{2\pi/N_t} d\phi}$$

$$= \frac{N_t \, a}{\sqrt{R_o^2 - a^2}} \qquad \text{[A-2]}$$

(All angles expressed in radians.)

Rewriting equation A-1:

$$d\phi = \frac{a \; d\theta}{\tan \alpha \; (R_o + a \cos \theta)} \qquad \text{[A-3]}$$

and integrating:

$$\phi + \phi_o = \frac{a}{\tan \alpha} \frac{2}{\sqrt{R_o^2 - a^2}} \tan^{-1}\left(\sqrt{\frac{R_o - a}{R_o + a}} \tan \frac{\theta}{2}\right)$$

$$= \frac{2}{N_t} \tan^{-1}\left(\sqrt{\frac{R_o - a}{R_o + a}} \tan \frac{\theta}{2}\right) \qquad \text{[A-4]}$$

$$\tan \frac{\theta}{2} = \sqrt{\frac{R_o - a}{R_o + a}} \quad \tan \frac{N_t(\phi + \phi_o)}{2} \qquad [A-5]$$

The computer code constructs the helical coils in the following manner: first, a set of points, uniformly spaced in ϕ, is positioned on the helical winding. This is done by picking the appropriate ϕ_o for the initial position, spacing the points in ϕ, and then solving for their θ positions with the help of the last equation. My goal is to approximate the helical winding with a series of straight line segments. One method would be to connect the set of points with straight line segments. I used a more accurate method, which I will illustrate with a simple example. Suppose I have a set of points of an arc of a circle, and I want to connect the points with line segments such that the segments closely followed the curve of the circle.

Given that I know the slope of the circle at each point, I create a line segment at every other point, matching each segment to the local slope of the circle, with each segment having length 2ℓ.

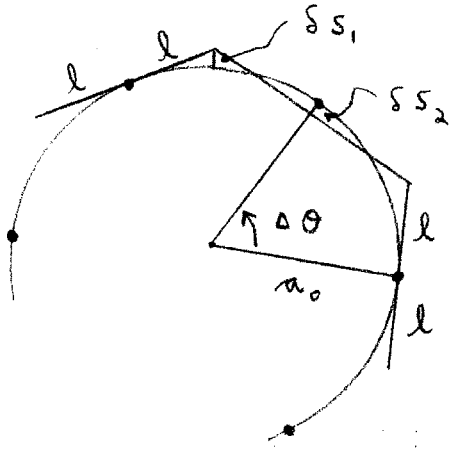

Figure A-2

"ℓ" is chosen so that $\delta s_1 = \delta s_2$, and is found as follows:

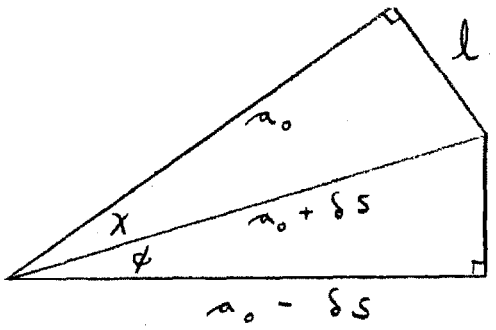

Figure A-3

$$\cos \phi = \frac{a_o - \delta s}{a_o + \delta s} \qquad [A\text{-}6]$$

$$\cos \chi = \frac{a_o}{a_o + \delta s}$$

with $\Delta\theta = \phi + \chi$ a known quantity, solve for δs.

$$a_o^2 + \ell^2 = a_o^2 + 2a_o\,\delta s + \delta s^2 \qquad [A\text{-}7]$$

$$\ell = \sqrt{(\delta s + 2a_o)\,\delta s} \qquad [A\text{-}8]$$

I will now extend this procedure so that it will work on a helical winding. I already have a set of N points on the helix, and I know that the direction of the winding at each of these points by the equation:

$$\hat{\ell} = \hat{\phi} \cos\alpha + \hat{\theta} \sin\alpha \qquad [A\text{-}9]$$

Again I create a line segment at every other point, matching each segment to the local slope of the helix, with each

segment having length $2\ell^*$. To determine the appropriate length ℓ^*, note that $\Delta\theta$ is known, so that the θ component of ℓ^* is ℓ, which has been found. Now, ℓ^* can be determined from the following relationship:

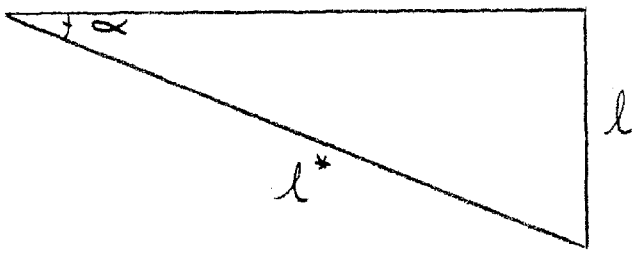

Figure A-4

$$\ell^* = \ell/\sin\alpha \qquad [A\text{-}10]$$

The toroidicity of the helix introduces an additional error of a/R_o order, which for the cases run added about 20 percent onto an already small deviation. The following data represent an average run by the computer code. The deviation figures were obtained by a detailed integration of the line segments' positions, relative to the true positions of the helical toroidal windings.

R_o	24 meters
a	4 meters
N_t	5 2/3
number of line segments representing winding	148

(continued...)

average radial deviation	.0013 meters
average magnitude of radial deviation	.0111 meters
|maximal radial deviation|	.0546 meters
average circumferencial deviation	-.0003 meters
average magnitude of circumferencial deviation	.0030 meters
|maximum circumferencial deviation|	.0138 meters

Table A-1

The deviations are small compared to the dimensions of an actual winding (even assuming a high current density of 6000 A/cm^2, the winding would still have a radial thickness of ~ 30 cm). Also, a test case was made with a winding represented by only 74 line segments, resulting in a four-fold increase in the deviations. No noticable differences were seen in the flux surfaces produced by this winding and the winding with 148 line segments. This matching was taken as confirmation that the coil's true helical position was being accurately represented.

After the set of line current segments is created, I next need to calculate the magnetic field at arbitrary positions due to these line currents. This is done by a simple summation of the contributions of each segment. I will now describe how the magnetic field from any line current is determined.

I am using a right-handed Cartesian coordinate system ($\hat{W}$, $\hat{D}$, $\hat{Z}$), with the observer at the origin, and the current segment L lying in the DW-plane with the current

flowing in the positive W direction.

Writing the Biot-Savart law:

$$d\underline{B} = \frac{\mu_o I}{4\pi} \frac{\underline{r} \times d\underline{L}}{r^3} \qquad \text{[A-11]}$$

(note direction of r)

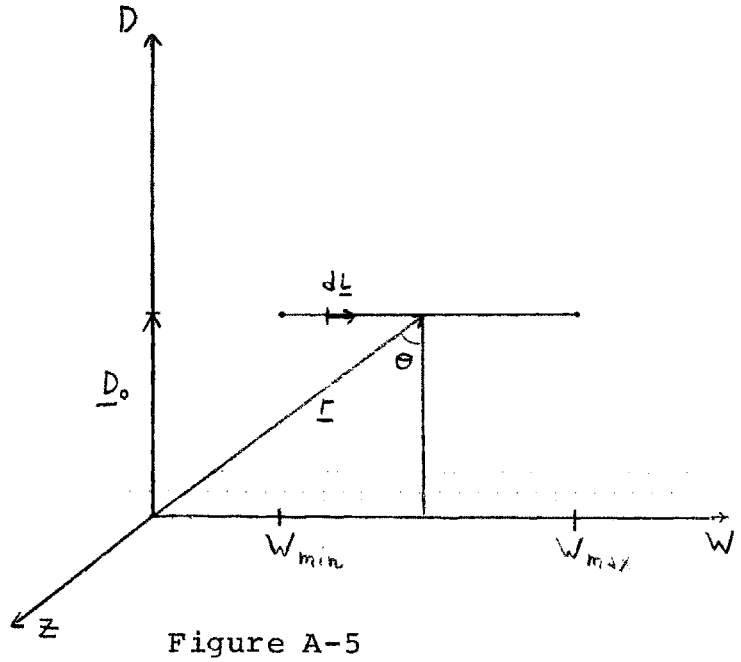

Figure A-5

where $\underline{r} = D_o \hat{D} + W \hat{W}$ [A-12]

$$d\underline{L} = dW \hat{W} \qquad \text{[A-13]}$$

$$d\underline{B} = \frac{\mu_o I}{4\pi} \frac{D_o \, dW (\hat{D} \times \hat{W})}{(D_o^2 + W^2)^{2/3}} \qquad \text{[A-14]}$$

Integrate:

$$\underline{B} = \frac{\mu_o I}{4\pi} \frac{\hat{D} \times \hat{W}}{D_o} \int_{W_{min}}^{W_{max}} \frac{D_o^2 \, dW}{(D_o^2 + W^2)^{3/2}}$$

$$= \frac{\mu_o I}{4\pi} \frac{\hat{D} \times \hat{W}}{D_o} = \frac{W}{(D_o^2 + W^2)^{1/2}} \Bigg|_{W_{min}}^{W_{max}} \qquad \text{[A-15]}$$

Any line segment can be oriented so as to conform to this representation, when the appropriate coordinate system is chosen. For example, assume the observation point is at the origin, the line current begins at point $P_1 = (x_1, y_1, z_1)$ and ends at point $P_2 = (x_2, y_2, z_2)$.

Let $\underline{r}_{12} = P_2 - P_1 = (\delta x, \delta y, \delta z)$. I want to find D_o in this coordinate system; I start by writing a set of locus equations:

$$D_{o\,x} = x_1 + \delta x \quad t$$

$$D_{o\,y} = y_1 + \delta y \quad t$$

$$D_{o\,z} = z_1 + \delta z \quad t \qquad \text{[A-16]}$$

$$\underline{D}_o \cdot \underline{r}_{12} = 0 = (\delta x^2 + \delta y^2 + \delta z^2)\, t + \delta x\, x_1 + \delta y\, y_1 + \delta z\, z_1 \qquad \text{[A-17]}$$

$$t = - \frac{(\delta x\, x_1 + \delta y\, y_1 + \delta z\, z_1)}{\underline{r}_{12} \cdot \underline{r}_{12}} \qquad \text{[A-18]}$$

$$W_{min} = - | \underline{r}_{12} |\, t \qquad \text{[A-19]}$$

$$W_{max} = W_{min} + | r_{12} | \qquad \text{[A-20]}$$

$\hat{W}$ = unit vector in $\underline{r}_{12}$ direction

All the terms in the equation for $\underline{B}$ are now known.

Now that the procedure for finding B has been described, I will describe the method by which a three-dimensional grid containing the values for $\underline{B}$ is created.

The periodicity length of $\underline{B}$ in a torsatron is a module length; hence the grid need only extend one module length in ϕ. Also, the grid need only cover the top half of the torsatron, since the bottom half is a mirror image of the top half. (This can be seen by flipping the torsatron over and reversing the current direction.) The relationship between $\underline{B}$ in the top half and $\underline{B}$ in the bottom half of the torsatron is given by the following equations:

$$B_r(r, y, \phi) = -B_r(r, -y, \phi_{mirror} - \phi) \qquad [A-21]$$

$$B_Y(r, y, \phi) = B_Y(r, -y, \phi_{mirror} - \phi) \qquad [A-22]$$

$$B_\phi(r, y, \phi) = B_\phi(r, -y, \phi_{mirror} - \phi) \qquad [A-23]$$

where ϕ_{mirror} is any ϕ-plane in the torsatron where the coils' radial positions in the top half are equal to those in the bottom half. This occurs at two different planes in any module, regardless of "ℓ" number.

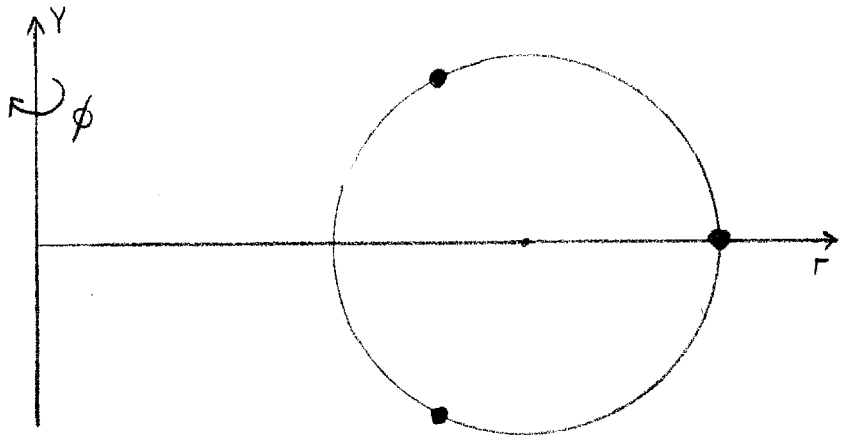

Figure A-6

The first step in creating the three-dimensional grid involves creating a grid extending only in two dimensions (r and Y) and containing separately the contributions from wires covering the surface of the torsatron (see Figure A-7). From this data base the 3-D grid is created by adding the wire contributions appropriate for the individual ϕ-planes. This procedure enables me to mock up windings of finite poloidal thickness with very little extra computation.

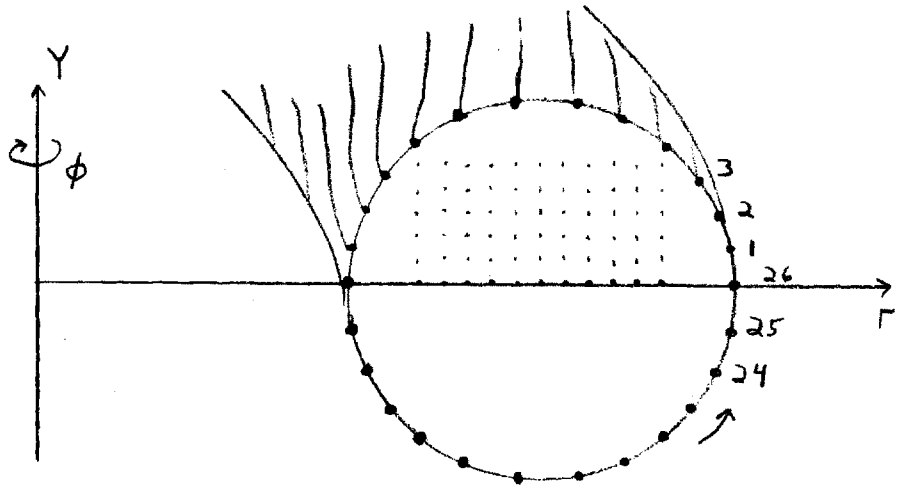

Figure A-7

To explain: suppose I wanted thirteen divisions in ϕ in a module length, and that the ℓ number is 2. I would then calculate the 2-D grid with 26 coils, spaced in θ so that when I move one division in ϕ, coil 1 is in the old θ position of coil 2; coil 2 is in the old θ position of coil 3; and so on. Note how this implies $\Delta\theta$ between coils

is not a constant, since $d\phi/d\theta$ is not a constant in a constant pitch winding. The next step involves calculating a true 3-D grid. Assume that I want each winding to cover about 19 percent of the torsatron surface area. I can approximate this poloidal thickness by adding the contributions of 5 of the 26 helical current filaments to represent one coil. For example, in the ϕ = 0 plane,

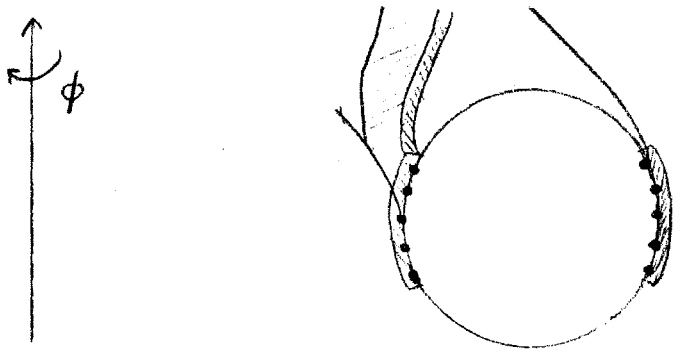

Figure A-8

where both coils are at Y = 0, I would add the contributions of coils 24, 25, 26, 1, 2 and 11, 12, 13, 14, 15 of the 2-D grid to get the ϕ = 0 values of the 3-D grid. For ϕ = one division (i.e., the next ϕ-plane in the 3-D grid, ϕ = 1/13 module displacement). I take the values of the ϕ = 0 plane, subtract the contributions of coils 24 and 11 of the 2-D grid, add the contributions of coils 3 and 16 of the 2-D grid, and have the ϕ = one division values of the 3-D grid. The net saving of this method is that only 1/ # filaments per coil amount of computation need be done, compared to solving for the 3-D grid values by integrating the effect of the ten filaments at each point. In a typical

computer run, with perhaps 60,000 points in the 3-D grid, and 15 filaments per coil, the routines to calculate the B field grid take about 3.5 minutes of CPU on a CDC 7600, rather than an hour which would be required by the direct 3-D evaluation.

Appendix B

This appendix describes the placement of the vertical field coils of the torsatron reactors. It contains:

1) a description of the effect the vertical field coils have on the flux surfaces

2) a description of how the coils' positions were chosen

3) an expression for magnetic field produced by circular current loops

4) a polynomial approximation for the elliptic integrals K and E.

The vertical field coils (VFC) of a torsatron consist of large, circular current loops lying alongside the main helical windings, carrying current in the opposite toroidal direction. Their primary purpose is to cancel

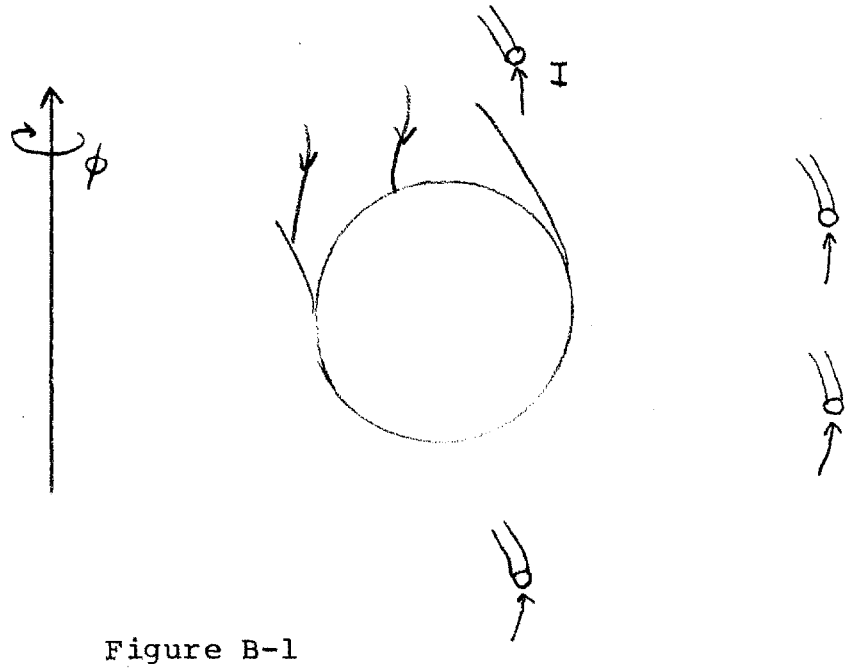

Figure B-1

the large vertical field produced by the helical windings, and thereby allow the formation of closed flux surfaces.

(The VFC also have the desirable property of canceling most of the dipole moment of the helical windings.)

The placement of the VFC of the torsatron designs considered in this study was done by the non-linear multi-parameter optimization code SOLVE.[1] This code solves for positions and currents of vertical field coils when required constraints are specified. These requirements can include geometrical constraints, specification of the magnetic field at many points, and specification of flux linkages and magnetic moments. For the reactor cases studied, it was found that nulling the field at 10 to 15 points on a grid loosely spread within the separatrix produced acceptable flux surfaces (see Table B-1).

Once the flux surfaces were created, I found that the location of the magnetic axis and the well depth of the surfaces are very sensitive to the amount of current in the VFC. A change of VFC current of 5 percent can move the magnetic axis the distance of a minor radius. An increase in the VFC current pushes the magnetic axis in towards the toroidal center, and decreases the well depth. Thus the VFC current can be changed to obtain more or less well depth, up to a maximum of about 10 percent well depth for the large aspect ratio torsatron ($R_o/a = 6$), and up to about 20 percent well depth for the small aspect ratio torus ($R_o/a = 3$), with well depth defined as:

$$\text{well depth} = \frac{\langle B^2 \rangle_{max} - \langle B^2 \rangle_{axis}}{\langle B^2 \rangle_{max}} \qquad [B\text{-}1]$$

Sunday, September 9, 1979 12:56:38 JOK:NPOL;SOUT 1112

SOLVE VERSION 3.4
****

RUN NUMBER 1112 AT 06:44:20
AA MACHINE ON 08/21/79

DETAILS OF DIPOLE MODEL OF HELIX

TOTAL AZIMUTHAL CURRENT	1.200E+08
MAJOR RADIUS	2.400E+01
MINOR RADIUS	4.000E+00
CONDUCTOR RADIUS	2.000E-02
FIXED COILS FOR HELIX	50
WINDING LAW	CONSTANT PITCH ANGLE LAW

NON-LINEAR MINIMIZER CALLED WITH M = 14 WISHES:

	-AT COORDINATES-		-WISH-		
	R	Z	TYPE	VALUE	WEIGHT
1	22.000	0.	2 VERTICAL B FIELD	0.	1.000E+00
2	22.600	1.410	2 VERTICAL B FIELD	0.	1.000E+00
3	24.000	2.000	2 VERTICAL B FIELD	0.	1.000E+00
4	25.400	1.410	2 VERTICAL B FIELD	0.	1.000E+00
5	26.000	0.	2 VERTICAL B FIELD	0.	1.000E+00
6	22.600	1.410	1 RADIAL B FIELD	0.	1.000E+00
7	24.000	2.000	1 RADIAL B FIELD	0.	1.000E+00
8	25.400	1.410	1 RADIAL B FIELD	0.	1.000E+00
9	23.000	0.	2 VERTICAL B FIELD	0.	5.000E+00
10	24.000	1.000	2 VERTICAL B FIELD	0.	5.000E+00
11	25.000	0.	2 VERTICAL B FIELD	0.	5.000E+00
12	24.000	1.000	1 RADIAL B FIELD	0.	5.000E+00
13	24.000	0.	2 VERTICAL B FIELD	0.	1.000E+01
14	24.000	0.	5 DIPOLE MOMENT	0.	1.000E+00

4 NULLING COILS WERE STARTED AT :

R	Z	I	
23.000	14.300	-2.570E+07	(PAIR AT +/- Z)
34.000	5.830	-1.380E+07	(PAIR AT +/- Z)

INPUT PARAMETERS TO THE MINIMIZER :

IOPT =	1	(ALGORITHM OPTION)
MAXFN =	1000	(MAXIMUM FUNCTION CALLS)
NSIG =	5	(SIGNIFICANT FIGURES)
EPS =	1.00E-08	(RESIDUAL SUM OF SQUARES)
DELTA =	1.00E-07	(NORM OF GRADIENT)

1 1112

FINISHED WITH INFER = 2 IER = 0.

Sunday, September 9, 1979 12:56:38 DCK:RPOL;SOUT 1112

FINAL COIL POSITIONS

R	Z	I	
22.758	13.859	-2.770E+07	(PAIR AT +/- Z)
33.548	5.777	-1.753E+07	(PAIR AT +/- Z)

DETAILS OF SOLUTION
SUM OF SQUARES OF RESIDUALS : 3.38951E-06

RESIDUAL (ERROR W.R.T. WISH) :	WEIGHTED	NORMALIZED	ABSOLUTE
1	4.01709E-04	4.01831E-04	5.06551E-04
2	-5.20295E-04	-5.20251E-04	-6.50421E-04
3	6.52402E-04	6.52450E-04	7.71356E-04
4	-9.12693E-04	-9.12641E-04	-1.03653E-03
5	1.05460E-03	1.05465E-03	1.17601E-03
6	-1.46788E-04	-1.46827E-04	8.07946E-06
7	-5.71258E-04	-5.71302E-04	4.08351E-05
8	-9.26865E-05	-9.27270E-05	4.30019E-06
9	-3.29078E-05	-6.55250E-06	-8.00256E-06
10	7.37687E-05	1.48015E-05	1.75257E-05
11	2.95796E-04	5.92096E-05	6.80722E-05
12	1.77824E-04	3.55225E-05	-1.27045E-06
13	-2.40058E-04	-2.40381E-05	-2.84706E-05
14	-1.17890E-05	-1.17531E-05	-2.51645E+06

NORM OF GRADIENT : 3.9922E-05
FUNCTION EVALUATIONS : 90.
ESTIMATED SIGNIFICANT DIGITS : 3.
FINAL MARQUARDT SCALING PARAMETER : 1.5145E-06
ITERATIONS : 24.

Table B-1

If one attempts to get a larger well by decreasing the VFC current still further, the magnetic axis comes in contact with the outside edge of the separatrix, and the flux surfaces are destroyed.

I now present a brief outline of the procedure used to calculate the magnetic fields produced by the VFC.

Following Jackson,[2] consider a circular loop of radius a, centered at the origin of a cylindrical coordinate system, carrying a current I (MKS units). The current density has only a θ component:

$$J_\theta = I\ \delta(Z)\ \delta(\rho - a) \quad . \qquad [B-2]$$

The vector potential is

$$\underline{A} = \frac{\mu_o}{4\pi} \int_{\tau'} \frac{\underline{J}}{r}\ d\tau' \quad . \qquad [B-3]$$

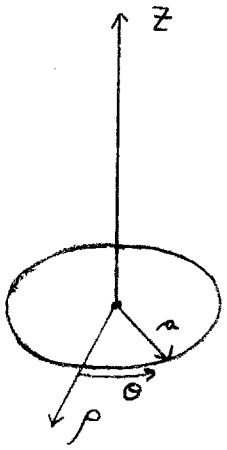

Figure B-2

The azimuthal integration is symmetric about $\Theta = 0$; hence the radial component of $\underline{A}$ is zero. This leaves only the Θ component, which is:

$$A_\theta(\rho, Z) = \frac{\mu_o I}{4\pi} \int_o^{2\pi} \frac{\cos\theta' \, d\theta'}{(a^2 + Z^2 + \rho^2 - 2a\rho\cos\theta')^{1/2}} \qquad [B-4]$$

Expressing this integral in terms of the complete elliptic integrals K and E:

$$A_\theta(\rho, Z) = \frac{\mu_o I a}{\pi(a^2 + Z^2 + \rho^2 + 2a\rho)^{1/2}} \frac{(2-m)K(m) - 2E(m)}{m} \qquad [B-5]$$

where $m = \sqrt{\frac{4a\rho}{Z^2 + (a+\rho)^2}}$ [B-6]

$$\underline{B} = \underline{\nabla} \times \underline{A} = -\frac{\partial A_\theta}{\partial Z}\hat{\rho} + \frac{1}{\rho}\frac{\partial}{\partial\rho}(\rho A_\theta)\hat{Z} \; . \qquad [B-7]$$

Evaluation of these derivatives is straightforward, noting that

$$\frac{\partial K(m)}{\partial Z} = \frac{\partial m}{\partial Z}\frac{dK(m)}{dm} \text{ , etc.} \qquad [B-8]$$

and that

$$\frac{dK(m)}{dm} = \frac{1}{2m}\left(\frac{E}{1-m} - K\right) \qquad [B-9]$$

$$\frac{d\,E(m)}{d\,m} = \left(\frac{1}{2m}(E - K)\right). \qquad [B-10]$$

The results are:

$$B_\theta = 0 \qquad \text{[B-11]}$$

$$B_\rho = I \frac{\mu_o}{2\pi} \frac{Z}{\rho[(a+\rho)^2 + Z^2]^{1/2}} \left[\frac{E(a^2+\rho^2+Z^2)}{(a-\rho)^2+Z^2} - K\right] \qquad \text{[B-12]}$$

$$B_Z = I \frac{\mu_o}{2\pi} \frac{1}{\rho[(a+\rho)^2 + Z^2]^{1/2}} \left[\frac{E(a^2-\rho^2-Z^2)}{(a-\rho)^2+Z^2} + K\right]. \qquad \text{[B-13]}$$

The following polynomial approximations were used for the values of K and E,[3, 4]

$$K(m) = \sum_{i=o}^{4} X^i (a_i + b_i \log_e(1/X)) + \varepsilon(m)$$

$$|\varepsilon(m)| < 2 \cdot 10^{-8} \qquad \text{[B-14]}$$

$$X = 1 - m$$

$a_o = 1.38629\ 436112$ $\qquad$ $b_o = .5$

$a_1 = .09666\ 344259$ $\qquad$ $b_1 = .12498\ 593597$

$a_2 = .03590\ 092383$ $\qquad$ $b_2 = .06880\ 248576$

$a_3 = .03742\ 563713$ $\qquad$ $b_3 = .03328\ 355346$

$a_4 = .01451\ 196212$ $\qquad$ $b_4 = .00441\ 787012$

$$E(m) = 1 + \sum_{i=1}^{4} X^i (e_i + d_i \log_e(1/X)) + \varepsilon(m)$$

$$|\varepsilon(m)| < 2 \cdot 10^{-8} \qquad \text{[B-15]}$$

$e_1 = .44325\ 141463$ $\qquad$ $d_1 = .24998\ 368310$

$e_2 = .06260\ 601220$ $\qquad$ $d_2 = .09200\ 180037$

$e_3 = .04757\ 383546$ $\qquad$ $d_3 = .04069\ 697526$

$e_4 = .01736\ 506451$ $\qquad$ $d_4 = .00526\ 449639$

References, Appendix B

1) J. G. Aspinall, The SOLVE Computer Code, M.I.T. Dept. of Nuclear Engineering (1979).

2) J. D. Jackson, Classical Electrodynamics, John Wiley and Sons, Inc., New York (1975), pp. 177-178.

3) M. Abramowitz and I. Segun, Handbook of Mathematical Functions, Dover Publications, Inc., New York (1968), pp. 591-592.

4) C. Hastings, Jr., Approximations for Digital Computers, Princeton University Press, Princeton, N.J. (1955).

Appendix C

This appendix describes how cubic spline interpolation was implemented in this study. In particular, it contains:

1) the motivation for using spline interpolation

2) an outline of spline theory

3) a description of the use of spline interpolation, covering the extension to multi-dimensional interpolation and the inclusion of boundary conditions

4) a description of the calculation of $\underline{B}$, $\underline{\nabla B}$, $\psi_{toroidal}$, and $\underline{\nabla}\psi_{toroidal}$ within a torsatron from a series of two-dimensional spline grids

5) a description of the differentiation formula used to calculate the second derivatives of $\underline{B}$ needed in the construction of the spline grids.

A common problem in numerical computation is that of interpolating the value of a function f whose value is known only at discrete points. One solution involves constructing a curve through the points by expanding a set of linearly independent eigenfunctions (hereafter called basis functions) and then defining the curve G as:

$$G(X) = \sum_i \alpha_i B_i(X) \qquad [C\text{-}1]$$

where B(X) represents the basis functions, and α represents a set of basis coefficients, which are determined by the function f. If f were a continuous function, an infinite series of basis functions (such as an infinite Fourier series) would be needed in order to construct a curve through the continuum of data. Since f is known only at a finite number

of data points, however, only a finite number of basis functions (e.g., a finite Fourier series) is needed. As another example, if f(X) is known at n data points, one could define $B_i(X) \equiv X^i$ and define G(X) as:

$$G(X) = \sum_{i=0}^{n-1} \alpha_i B_i(X) = \sum_{i=0}^{n-1} \alpha_i X^i \qquad [C-2]$$

By requiring G(X) = f(X) at the n distinct data points, the basis coefficients are determined. This approach also has the desirable feature that G(X) and all-order derivatives of G(X) are continuous. As the number of data points becomes large, this method suffers from the large amount of computation needed to calculate both the basis coefficients, and also G(X) by computing n basis functions each time a value for G(X) is desired.

It is desirable to retain control of the continuity of the derivatives of G(X), but also to define $B_i(X)$ such that it is non-zero over only a small range of values. The summation of $\alpha_i B_i(X)$ can then be done with only those values of i for which $B_i(X)$ is known to be non-zero. A set of basis functions called B-splines meets these requirements. The spline method of interpolation was developed by Schönberg,[1] and extended to multi-dimensional problems by C. deBoor.[2]

A spline is defined to be a polynomial function which is piecewise continuous to degree m - 1, where m is the order of the polynomials. Schönberg defines the spline basis function as:

$$B_\ell(X) = \sum_{i=0}^{m} \frac{(-1)^i \, m!}{i! \, (m-i)!} \, (X - X_{\ell+i+2-m})_+^{m-1} \qquad [C-3]$$

where $(X - X_k)_+ = X - X_k$ for $X > X_k$ [C-4]

$(X - X_k)_+ = 0$ for $X \leq X_k$ [C-5]

In the case of cubics ($m = 4$),

$$\begin{aligned} B_\ell(X) = {} & (X - X_{\ell+2})_+^3 \\ & - 4\,(X - X_{\ell+1})_+^3 \\ & + 6\,(X - X_\ell)_+^3 \\ & - 4\,(X - X_{\ell-1})_+^3 \\ & + (X - X_{\ell-2})_+^3 \end{aligned} \qquad [C-6]$$

which is non-zero on the interval $(X_{\ell-2}, X_{\ell+2})$ and defined as zero elsewhere.

The continuity of B_ℓ and its derivatives $B_\ell^k(X)$ is guaranteed for $k < m - 1$. Thus, for $m = 4$ (cubic splines):

$B_\ell(X)$, $\frac{\partial B_\ell(X)}{\partial X}$, and $\frac{\partial^2 B_\ell(X)}{\partial X^2}$ are continuous

$\frac{\partial^3 B_\ell(X)}{\partial X^3}$ is discontinuous only at the original data points in f (also called knot points), and constant in between

$\frac{\partial^k B_\ell(X)}{\partial X^k} = 0$ for all X, for $k \geq 4$.

I will now step through the solution procedure for

cubic spline interpolation (m = 4) for a one-dimensional case.

Given n data points,

$$\overset{\cdot}{1} \quad \overset{\cdot}{2} \quad \cdots \quad \overset{\cdot}{n-1} \quad \overset{\cdot}{n}$$

$\frac{1}{2}(m-2)$ extra data points are needed on each end of the array as boundary conditions, in order to uniquely determine the α coefficients. Here I will choose second derivative boundary conditions, so my expanded set of data points looks like this:

f:

$$\overset{\cdot}{0} \quad \overset{\cdot}{1} \quad \overset{\cdot}{2} \quad \cdots \quad \overset{\cdot}{n-1} \quad \overset{\cdot}{n} \quad \overset{\cdot}{n+1}$$

[knot points]

where $f_0 = \left.\frac{\partial^2}{\partial X^2} f(X)\right|_{f_1}$

$$f_{n+1} = \left.\frac{\partial^2 f(X)}{\partial X^2}\right|_{f_n}$$

Now, write f as:

$$f(X_i) = \sum_{\ell=0}^{n+1} \alpha_\ell \; B_\ell(X_i) \equiv \sum_{\ell=0}^{n+1} \alpha_\ell \; B_{\ell i} \qquad [C\text{-}7]$$

Operate on both sides of the equations with $\sum_i B^{-1}_{i\ell'}$

$$\sum_{i=0}^{n+1} B^{-1}_{i\ell'} \; f(X_i) = \sum_{i=0}^{n+1} B^{-1}_{i\ell'} \sum_{\ell=0}^{n+1} \alpha_\ell \; B_{\ell i}$$

(continued...)

$$= \sum_{\ell=0}^{n+1} \alpha_\ell \left(\sum_{i=0}^{n+1} B^{-1}_{i\ell'} B_{\ell i} \right)$$

$$= \sum_{\ell=0}^{n+1} \alpha_\ell \, \delta_{\ell\ell'}$$

$$= \alpha_{\ell'} \qquad [C-8]$$

To construct the B matrix, I must calculate $\frac{\partial^2}{\partial X^2} B_\ell(X)$, second derivative boundary conditions are used.

$$\frac{\partial^2}{\partial X^2} B_\ell(X) = +6 \, (X - X_{\ell+2})_+ - 24 \, (X - X_{\ell+1})_+ + 36 \, (X - X_\ell)_+ - 24 \, (X - X_{\ell-1})_+ + 6 \, (X - X_{\ell-2})_+ \qquad [C-9]$$

ℓ#	0	1			j			
	.	.	.	.	.	.	.	.
$B(X_j)$	.	. ← all zero	.	.	1	4	1	0 . → all zero
$\frac{\partial^2 B(X)}{\partial X^2}\Big\vert_{X_j}$	.	. ← all zero	.	.	6	-12	6	0 . → all zero

Thus the i'th column of $\underline{\underline{B}}$ will be:

	column #0	#1	#2	#i
row #0				0
#1				0
				0
				0
				1
#i				4
				1
				0

Thus, for $n = 3$, columns 1 to 3 of $\underline{\underline{B}}$ would look like this:

$$\begin{bmatrix} 6 & 1 & 0 & 0 & 0 \\ -12 & 4 & 1 & 0 & 0 \\ 6 & 1 & 4 & 1 & 6 \\ 0 & 0 & 1 & 4 & -12 \\ 0 & 0 & 0 & 1 & 6 \end{bmatrix}$$

column #	0	1	2	3	4

Columns 0 and $n+1$ are determined by the fact that $f_0 = \left.\frac{\partial^2 f}{\partial X^2}\right|_{f_1}$ and $f_4 = \left.\frac{\partial^2 f}{\partial X^2}\right|_{f_3}$, so the appropriate $\frac{\partial^2 B_\ell(X)}{\partial X^2}$ $(\ell = 0 \text{ to } n+1)$ vector is placed in these columns.

Finally, $\underline{\underline{B}}^{-1}$ is computed, and

$$G(X) = \sum_{\ell=0}^{n+1} \alpha_\ell \; B_\ell(X), \quad X_1 \leq X \leq X_n \qquad [C\text{-}10]$$

$$\alpha_\ell = \sum_{i=0}^{n+1} B^{-1}_{i\ell} \; f(X_i) \qquad [C\text{-}11]$$

For spline interpolation of a multi-dimensional problem, one-dimensional basis fuctions must be calculated for each dimension of the data. In three dimensions, for example,

$$G(X, Y, Z) = \sum_{\ell} \sum_{m} \sum_{n} \alpha_{\ell mn} \; B^{(x)}_\ell(X) \; B^{(y)}_m \; B^{(z)}_n \; (Z) \qquad [C\text{-}12]$$

At a data point:

$$f(x_i, y_j, z_k) = \sum_{\ell} \sum_{m} \sum_{n} \alpha_{\ell mn} \; B^{(x)}_\ell(X_i) \; B^{(y)}_m(y_j) \; B^{(z)}_n(z_k) \qquad [C\text{-}13]$$

$$f_{ijk} = \sum_{\ell} \sum_{m} \sum_{n} \alpha_{\ell mn} \; B^{(x)}_{\ell i} \; B^{(y)}_{mj} \; B^{(z)}_{nk} \;, \qquad [C\text{-}14]$$

with i, j, and k having the same dimensions as ℓ, m, and n, respectively. The spline coefficients are now computed, as in the one-dimensional case, only now an additional summation is required for each extra dimension.

$$\alpha_{\ell'm'n'} = \sum_{k} \sum_{j} \sum_{i} B^{(z)^{-1}}_{kn'} \; B^{(y)^{-1}}_{jm'} \; B^{(x)^{-1}}_{i\ell'} \; f_{ijk} \qquad [C\text{-}15]$$

I will now step through a very simple two-dimensional problem to illustrate the inclusion of boundary conditions and the limits of the summation operators.

Suppose the initial data is a 2 by 3 rectangular grid.

XMAX = 3
YMAX = 2

$$\begin{array}{ccc} \cdot & \cdot & \cdot \\ f_{12} & f_{22} & f_{32} \\ \cdot & \cdot & \cdot \\ f_{11} & f_{21} & f_{31} \end{array}$$

Using cubic spline basis functions, I require one extra data point at each limit of the grid in both the X and Y directions. This gives:

$$\begin{array}{ccccc} & \cdot & \cdot & \cdot & \\ & f_{13} & f_{23} & f_{33} & \\ \cdot & \cdot & \cdot & \cdot & \cdot \\ f_{02} & f_{12} & f_{22} & f_{32} & f_{42} \\ \cdot & \cdot & \cdot & \cdot & \cdot \\ f_{01} & f_{11} & f_{21} & f_{31} & f_{41} \\ & \cdot & \cdot & \cdot & \\ & f_{10} & f_{20} & f_{30} & \end{array}$$

where

$$f_{j0} = \frac{\partial^2}{\partial y^2} f \Big|_{f_{j1}} \qquad j = 1, 2, 3$$

$$f_{j3} = \frac{\partial^2}{\partial y^2} f \Big|_{f_{j2}} \qquad j = 1, 2, 3$$

$$f_{0j} = \frac{\partial^2}{\partial x^2} f \Big|_{f_{1j}} \qquad j = 1, 2$$

(continued...)

$$f_{4j} = \frac{\partial^2}{\partial x^2} f \Big|_{f_{3j}} \qquad j = 1, 2$$

Notice that the extra dimensionality of the problem creates the need for four more boundary conditions, in particular the four corners of the expanded f grid. The values of f at these four corners form the boundary conditions of the boundary conditions of f. The four corner values of f are determined by the same method used to calculate the other edge values of f. In this case, since second derivative boundaries were used, consistency requires that the corner values of f be the second derivative of the edge values of f. In particular,

$$f_{00} = \frac{\partial^2}{\partial y} f \Big|_{f_{01}} = \frac{\partial^2}{\partial x^2} f \Big|_{f_{10}} = \frac{\partial^2}{\partial y} \frac{\partial^2}{\partial x} f \Big|_{f_{11}}$$

$$f_{03} = \frac{\partial^2}{\partial y} f \Big|_{f_{02}} = \frac{\partial^2}{\partial x^2} f \Big|_{f_{13}} = \frac{\partial^2}{\partial y^2} \frac{\partial^2}{\partial x^2} f \Big|_{f_{12}}$$

$$f_{43} = \frac{\partial^2}{\partial y^2} f \Big|_{f_{42}} = \frac{\partial^2}{\partial x^2} f \Big|_{f_{33}} = \frac{\partial^2}{\partial y^2} \frac{\partial^2}{\partial x^2} f \Big|_{f_{32}}$$

$$f_{40} = \frac{\partial^2}{\partial y^2} f \Big|_{f_{41}} = \frac{\partial^2}{\partial x^2} f \Big|_{f_{30}} = \frac{\partial^2}{\partial y^2} \frac{\partial^2}{\partial x^2} f \Big|_{f_{31}}$$

This rule also applies to higher-dimensional problems. If a three-dimensional f grid had second-derivative boundary

conditions, then the face locations on the f grid would have $\frac{\partial^2}{\partial x_i^2}$ f values, the edge locations would have $\frac{\partial^2}{\partial x_i^2}\frac{\partial^2}{\partial x_j^2}$ f values, and the eight corners would have $\frac{\partial^2}{\partial x_i^2}\frac{\partial^2}{\partial x_j^2}\frac{\partial^2}{\partial x_k^2}$ f values. Boundary conditions in the different directions need not be of the same order. For example, if I keep the second derivative condition in the x direction $f_{01} = \frac{\partial^2}{\partial x^2} f \Big|_{f_{11}}$, etc. but have first order derivative boundary conditions in the y direction $f_{10} = \frac{\partial}{\partial y} f \Big|_{f_{11}}$, etc. , the corner cells reflect this change:

$$f_{00} = \frac{\partial}{\partial y} f \Big|_{f_{01}} = \frac{\partial^2}{\partial x^2} f \Big|_{f_{10}} = \frac{\partial}{\partial y}\frac{\partial^2}{\partial x^2} f \Big|_{f_{11}}, \text{ etc.}$$

Returning to the main problem: I have now constructed the expanded f grid. The next step is to construct the $B^{(x)}$ and the $B^{(y)}$ matrices. This is done in a manner identical to the one-dimensional case, since each direction is treated separately. The basis matrices become:

$B^{(x)}$ =

	6	1	0	0	0
	-12	4	1	0	0
XMAX = 3	6	1	4	1	6
	0	0	1	4	-12
	0	0	0	1	6

$$B^{(y)} = \begin{matrix} 6 & 1 & 0 & 0 \\ -12 & 4 & 1 & 6 \\ 6 & 1 & 4 & -12 \\ 0 & 0 & 1 & 6 \end{matrix} \qquad \text{YMAX} = 2$$

I am now ready to calculate the α matrix.

$$\alpha_{\ell m} = \sum_{i=0}^{\text{XMAX}+1} \sum_{j=0}^{\text{YMAX}+1} (x)^{-1}_{i\ell} \; B_{jm} \; f_{ij} \qquad \text{[C-16]}$$

(in matrix notation, this is equivalent to:

$$\alpha = \left(\left(f \; B^{(y)^{-1}} \right)^T \; B^{(x)^{-1}} \right)^T \qquad \text{[C-17]}$$

Finally:

$$G(x,y) = \sum_{\ell} \sum_{m} \alpha_{\ell m} \; B_{\ell}^{(x)}(x) \; B_{m}^{(y)}(y) \qquad \text{[C-18]}$$

I will now give a relatively simple set of equations that calculate the spline basis function values. I will work in one dimension, since any other basis functions in other possible dimensions are evaluated independently and in exactly the same manner.

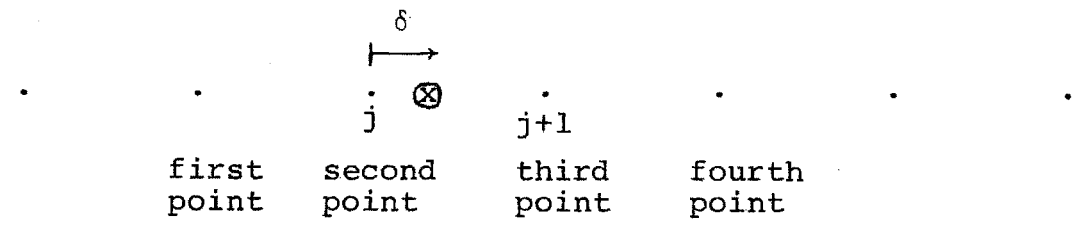

Assume G(x) is desired to be known, and $x_j \leq x < x_{j+1}$. We

are guaranteed that $B_\ell(x) = 0$ for $\ell < j-1$ or $\ell > j+2$.

Thus:

$$G(x) = \sum_{i=j-1}^{j+2} B_i(x)\ \alpha_i \qquad [C\text{-}19]$$

By simple algebra, I find the values of B(x) at the four points of interest to be the following:

first point:

$$B_\ell = -\delta^3 + 3\delta^2 - 3\delta + 1 \qquad [C\text{-}20]$$

second point:

$$B_\ell = 3\delta^3 - 6\delta^2 + 4 \qquad [C\text{-}21]$$

third point:

$$B_\ell = 1 + 3 * (\delta^2 + \delta - \delta^3) \qquad [C\text{-}22]$$

fourth point:

$$B_\ell = \delta^3 \qquad [C\text{-}23]$$

where δ is the percentage distance of x from x_j to x_{j+1} (hence $0 \leq \delta < 1$).

As a final point, note that derivatives of G can be found by directly differentiating the basis functions.

$$\frac{\partial}{\partial x} G(x) = \sum_{i=j-1}^{j+2} \alpha_i\ \nabla B_i(x) \qquad [C\text{-}24]$$

where the four non-zero values of ∇B_i are:

first point:

$$\nabla B_i = -3\delta^2 + 6\delta - 3 \qquad \text{[C-25]}$$

second point:

$$\nabla B_i = 9\delta^2 - 12\delta \qquad \text{[C-26]}$$

third point:

$$\nabla B_i = 6\delta - 9\delta^2 + 3 \qquad \text{[C-27]}$$

fourth point:

$$\nabla B_i = 3\delta^2 \qquad \text{[C-28]}$$

$\frac{\delta^2}{\delta x^2} G(x) = \sum_{i=j-1}^{j+2} \alpha_i \nabla^2 B_i(x)$, if the second derivative is desired. $\frac{\partial^3 G(x)}{\partial x^3}$ is discontinuous at the knot points, and $\frac{\partial^4 G(x)}{\partial x^4}$ and higher-order derivatives are identically equal to zero everywhere.

The accuracy of these derivative calculations depends on the order of the spline fit. Obviously, the original f function, whose value is known at the original grid locations, might have non-zero fourth-order derivatives, but these could never be found by cubic spline interpolation. A higher-order spline fit would have to be used. The exact order needed would depend both on the accuracy needed and values of the original data.

Torsatron Field Calculations

In this thesis, the magnetic field within a torsatron was approximated by a series of two-dimensional spline grids, equally spaced in the toroidal directions ϕ. This approach was motivated by the fact that two-dimensional spline interpolation is over four times as fast as three-dimensional spline interpolation. The two-dimensional method does impose the constraint that field quantities can now only be accurately calculated on the discrete ϕ-planes of the spline grids. The particle pushing algorithm was therefore constructed so that the particle's position always lies on one of these spline grids, and the pushing algorithm moves the particle from one plane to the next (for a detailed description, see Chapter II). The pushing algorithm requires the following field quantities: $\underline{B}$, $\underline{\nabla}\underline{B}$, $\psi_{toroidal}$, and $\underline{\nabla}\psi_{toroidal}$ (the need for the $\psi_{toroidal}$ values arises from the fact that voltage profiles were mapped onto the toroidal flux profiles; hence $\underline{\nabla}\psi_{toroidal}$ is needed to calculate the electric field quantity that appears in the guiding-center equations). As a data base, four different spline grids are kept for each plane, one for B_x, a second for B_y, and a third for B_z, and a fourth for $\psi_{toroidal}$.

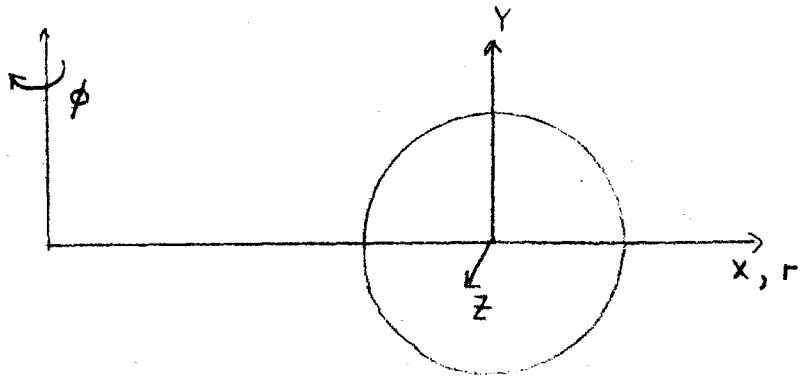

Thus $\underline{B}$ and $\Psi_{toroidal}$ are found by standard spline interpolation. In calculating the quantities

$$\frac{\partial B_x}{\partial x}\ ,\ \frac{\partial B_y}{\partial x}\ ,\ \frac{\partial B_z}{\partial x}\ ,\ \frac{\partial B_x}{\partial y}\ ,\ \frac{\partial B_y}{\partial y}\ ,\ \frac{\partial B_z}{\partial y}\ ,\ \frac{\partial \psi_T}{\partial x}\ ,\ \frac{\partial \psi_T}{\partial y}$$

the derivatives of the spline basis functions multiply the α coefficients, rather than the basis functions themselves. Unfortunately, this method could not be used in calculating the Z (toroidal) derivatives, since the two-dimensional basis functions do not extend in that direction. To complete the $\underline{\nabla B}$ tensor, note that:

$$\underline{\nabla} \cdot \underline{B} = 0 = \frac{\partial B_x}{\partial x} + \frac{\partial B_y}{\partial y} + \frac{\partial B_z}{\partial z} \qquad [C\text{-}29]$$

$$\underline{\nabla} \cdot \underline{B} = 0 \Rightarrow \left(\frac{\partial B_x}{\partial z} = \frac{\partial B_z}{\partial x}\right)\ ,\quad \left(\frac{\partial B_y}{\partial z} = \frac{\partial B_z}{\partial y}\right) \qquad [C\text{-}30]$$

Thus $\frac{\partial \underline{B}}{\partial z}$ is known. The fact that $\underline{\nabla} \cdot \underline{B} = 0$ allows a check on accurach of the ∇B calculation, since $\frac{\partial B_x}{\partial y} = \frac{\partial B_y}{\partial x}$. Calculated independently, these two values matched each other to 4 to 8 significant figures, the lowest accuracy occurring nearer the

outside edge of the spline grids.

To calculate $\frac{\partial \psi_T}{\partial z}$, ψ_t is evaluated in an adjacent ϕ-plane (with the same X-Y coordinates) and $\frac{\partial \psi_t}{\partial z}$ is approximated by

$$\frac{\partial \psi_t}{\partial z} = \frac{\psi_t - \psi_t(\text{adjacent plane})}{\delta z} \qquad \text{[C-31]}$$

In order to have the particle pushing algorithm accurate to second order in Δt, a forward finite difference for $\frac{\partial \psi_t}{\partial z}$ is done in the predictor phase, and a backward finite difference for $\frac{\partial \psi_t}{\partial z}$ is done in the corrector phase.

In the computer code, the spline grids only extended half a module length, since the fields in the second half are a mirror image of the first half (see discussion in Appendix A). Here are the field relationships between points in the first half of a module, and their associated mirror points:

$$\psi_{\text{toroidal}}(r, y, \phi) = \psi_{\text{toroidal}}(r, -y, \phi_{\text{mirror}} - \phi) \qquad \text{[C-32]}$$

$$\left(\frac{\partial \psi_t}{\partial r}, \frac{\partial \psi_t}{\partial y}, \frac{\partial \psi_t}{\partial z}\right)_{(r,y,\phi)} = \left(\frac{\partial \psi_t}{\partial r}, -\frac{\partial \psi_t}{\partial y}, -\frac{\partial \psi_t}{\partial z}\right)_{(r,-y,\phi_{\text{mirror}}-\phi)} \qquad \text{[C-33]}$$

$$(B_r, B_y, B_z)_{(r,y,\phi)} = (-B_r, B_y, B_z)_{(r,-y,\phi_{\text{mirror}}-\phi)} \qquad \text{[C-34]}$$

$$\begin{bmatrix} \frac{\partial B_r}{\partial r} & \frac{\partial B_y}{\partial r} & \frac{\partial B_z}{\partial r} \\ \frac{\partial B_r}{\partial y} & \frac{\partial B_y}{\partial y} & \frac{\partial B_z}{\partial y} \\ \frac{\partial B_r}{\partial z} & \frac{\partial B_y}{\partial z} & \frac{\partial B_z}{\partial z} \end{bmatrix} \quad (r, Y, \phi)$$

$$= \begin{bmatrix} -\frac{\partial B_r}{\partial r} & \frac{\partial B_y}{\partial r} & \frac{\partial B_z}{\partial r} \\ \frac{\partial B_r}{\partial y} & -\frac{\partial B_y}{\partial y} & -\frac{\partial B_z}{\partial y} \\ \frac{\partial B_r}{\partial z} & -\frac{\partial B_y}{\partial z} & -\frac{\partial B_z}{\partial z} \end{bmatrix} \quad (r, -Y, \phi_{mirror} - \phi)$$

[C-35]

In calculating the B spline grids, second-derivative boundary conditions were used. These second derivatives were found with a six-point differentiation formula. In grid units (Δh = 1 grid distance), this formula is:[4]

$$\left.\frac{d^2 B}{d x_i^2}\right|_0 = \frac{2!}{5!} \sum_{i=0}^{5} A_i \; B_i$$

[C-36]

data grid

$$\left.\frac{\partial^2 B}{\partial x^2}\right|_0 \quad \begin{matrix} \cdot & \cdot & \cdot & \cdot & \cdot & \cdot & \cdot & \cdot \\ \cdot & \cdot & \cdot & \cdot & \cdot & \cdot & \cdot & \cdot \\ \cdot & \dot{B}_{(0)} & \dot{B}_{(1)} & \dot{B}_{(2)} & \dot{B}_{(3)} & \dot{B}_{(4)} & \dot{B}_{(5)} & \dot{B}_{(6)} \\ \cdot & \cdot & \cdot & \cdot & \cdot & \cdot & \cdot & \cdot \\ \cdot & \cdot & \cdot & \cdot & \cdot & \cdot & \cdot & \cdot \end{matrix}$$

i	A_i
0	225
1	-770
2	1070
3	-780
4	305
5	-50

References, Appendix C

1) I. J. Schönberg, Quart. Appl. Math, 4 (1946), pp. 45-99, 112-141.

2) C. deBoor, J. Approximation Theory, 6 (1972), pp. 50-62.

3) D. V. Anderson, "The Three-Dimensional Tensor-Product, Spline Interpolation Code (TPSIC)," UCRL - 51958 (1976).

4) M. Abramowitz and I. Segun, Handbook of Mathematical Functions, Dover Publications, Inc., New York (1968), p. 914.

Appendix D

This appendix describes the procedures used in analyzing the vacuum magnetic field of a torsatron. In particular, it describes:

1) the predictor-corrector method used to track a field line

2) the algorithm that determined when closed flux surfaces were found

3) the calculations of ι, $\int \underline{B} \cdot d\underline{\ell}$, $\langle B^2 \rangle$, and helical and toroidal field ripple for the magnetic surfaces

4) the creation of a spline grid that allowed calculation of toroidal flux anywhere within the separatrix

5) the calculation of poloidal flux within the separatrix.

As described in Appendix C, the magnetic field within a torsatron module is approximated by a series of two-dimensional spline grids, equally spaced in the toroidal direction ϕ. Tracking a field line requires "pushing" the line position from one ϕ-plane to the next. In order to make the field line following code upgradable to a particle following code, the field line was followed by tracking a "particle" (launched on the field line) whose equation of motion was $V = V_o \hat{b}$, V_o being a unit velocity in MKS units. The tracking of the "particle" was done with a time-centered, predictor-corrector algorithm, which I'll now describe.

Starting with the position of the field line on the phi plane $\phi = \phi_o$ at $t = 0$, the magnetic field vector is calculated at this point, and the "particle's" unit velocity

vector is given its direction. Assuming constant toroidal and radial velocity, the time Δt required for the "particle" to intersect the adjacent ϕ-plane is calculated, as is the intersect position. The magnetic field at this point (the predictor point) is computed, and a new unit velocity vector is calculated, with its direction being the average of the directions of the magnetic fields at the original point and the predictor point. This new velocity vector is now used to move the "particle" to the adjacent phi-plane intersection point (the corrector point) in the same manner the predictor point was found. The "push" is now complete.

Here is a detailed description of how the intersection time Δt is computed. Given that toroidal velocity is assumed constant, the equation for the toroidal angular velocity is:

$$V_\phi(t) = V_\phi(t=0) \quad \frac{R(t=0)}{R(t)} \qquad [D\text{-}1]$$

$$R(t) = R(t=0) + V_{R_o}\, t \qquad [D\text{-}2]$$

$$\phi(\Delta t) = \phi_o + \int_0^{\Delta t} V_\phi(t')\, dt' \qquad [D\text{-}3]$$

$$\Delta\phi = \int_0^{\Delta t} V_{\phi_o} \quad \frac{d\,t'}{1 + (V_{R_o}/R_o)\; t'}$$

$$= -\frac{V_{\phi_o}\, R_o}{V_{R_o}} \quad \log_e \quad \frac{1}{1 + (V_{R_o}/R_o)\; \Delta t} \qquad [D\text{-}4]$$

$$\Delta t = \frac{R_o}{V_{R_o}} \left[\exp\left(\frac{\Delta\phi \; V_{R_o}}{R_o \; V_{\phi_o}} \right) - 1 \right] \qquad [D\text{-}5]$$

As the "particle" enters each module segment of the torsatron, its radial and vertical positions are recorded in a list, $(R, Z)_i$ being the "particle's" position after traveling i modules. The "particle" is considered to have completed one poloidal orbit after having traveled n modules when the following three conditions are met:

1) $| (R,Z)_{n-1} - (R,Z)_0 | < | (R,Z)_{n-2} - (R,Z)_0 |$

(i.e., the "particle" has recently been approaching its original starting location)

2) $| (R,Z)_n - (R,Z)_0 | > | (R,Z)_{n-1} - (R,Z)_0 |$

(i.e., the "particle" is now moving away from its original starting location)

3) $$\frac{((R,Z)_n - (R,Z)_{n-1}) \cdot ((R,Z)_1 - (R,Z)_0)}{|(R,Z)_n - (R,Z)_{n-1}| \quad |(R,Z)_1 - (R,Z)_0|} > .8$$

(i.e., the "particle's" current poloidal velocity direction closely matches the original one).

The integrals $\int \underline{B} \cdot d\underline{L}$ and $\int \frac{\underline{B} \cdot d\underline{L}}{B^2}$ are computed as the "particle" is tracked. Since $d\underline{L}$ is in the direction of $\underline{B}$, these integrals are simply the summation of $(\Delta r \; B)_j$ and $(\Delta r/B)_j$, respectively, summing j over all the pushes done by the tracking routine. The average rotational transform ι for each flux surface is found from the equation:

$$\iota = \frac{\Delta\theta}{\Delta\phi} , \qquad [D-6]$$

with $\Delta\Theta$ = 1 cycle for each closed surface. As a check on the accuracy of these calculations, $\iota \int_{1 \text{ poloidal orbit}} \underline{B}\cdot d\underline{L}$ is computed, and compared with a theoretical value derived from Ampere's law:

$$\iota \int_{1 \text{ poloidal orbit}} \underline{B}\cdot d\underline{L} = \mu_o \ell N_t I \qquad [D-7]$$

where

ℓ = "ℓ" number of the torsatron

N_t = number of poloidal turns of helical windings per toroidal turn

I = current per helical winding

Since, in the calculation of ι, $\Delta\phi$ is found as an integer number of modules traversed, there is a small round-off error in ι on the order of .3 percent (with 300 to 400 modules traversed on a typical surface not near the separatrix). It was found that the computed value of $\frac{1}{\iota}\int \underline{B}\cdot d\underline{L}$ matched the theoretical value in all cases, within the limits of the round-off error in ι. This test, plus the high degree of closure of the computed surfaces, allowed me to conclude that the tracking algorithm used was accurately following the field lines.

Once the integrals $\int \underline{B}\cdot d\underline{L}$ and $\int \frac{\underline{B}\cdot d\underline{L}}{B^2}$ are calculated, $\langle B^2 \rangle$, averaged over the flux surface, can be found through the equation:

$$\langle B^2 \rangle = \int \underline{B}\cdot d\underline{L} \Big/ \int \frac{\underline{B}\cdot d\underline{L}}{B^2} \qquad [D\text{-}8]$$

Knowing $\langle B^2 \rangle$ as a function of flux surface, I can map out the position and depth of the magnetic well formed by the torsatron vacuum fields. The well and shear characteristics of the magnetic field are related to the plasma's stability against resistive interchange modes. The well depth is very sensitive to the placement of the vertical field coils (see discussion in Appendix B).

The helical and toroidal ripple of the torsatron fields were measured in order to calculate the theoretical axisymmetric and ripple transport coefficients, which were compared to the numerical measurements of the ion thermal conductivity χ_i. The peak-to-average helical ripple was found by:

$$\text{ripple}_h = \frac{B_{max} - B_{min}}{B_{max} + B_{min}} \quad \text{along field line traversing one module} \qquad [D\text{-}9]$$

The peak-to-average toroidal ripple was found by:

$$\text{ripple}_t = \frac{\langle B \rangle_{180°} - \langle B \rangle_{0°}}{\langle B \rangle_{180°} + \langle B \rangle_{0°}} \qquad [D\text{-}10]$$

where

$\langle B \rangle_{X°}$ is the average field along a field line traversing one module at the flux surface position where the poloidal angle is X°.

These geometric measurements were compared with the Fourier components of the field modulation. The function

$B(\ell)$ along a field line for half a flux surface distance L (from poloidal angle = 0° to poloidal angle = 180°) was expanded into a Fourier cosine series:

$$B(\ell) = \frac{a_0}{2} + \sum_{n=1}^{N} a_n \cos\left(\frac{n \pi \ell}{L}\right) \qquad [D\text{-}11]$$

$$\text{with } a_n = \frac{2}{L} \int_0^L B(\ell) \cos\left(\frac{n \pi \ell}{L}\right) d\ell \qquad [D\text{-}12]$$

"a_1" represents the toroidal ripple, and the set of a_n (with wavelength $2\pi/n$ near a module length), when added in quadrature, represents the helical ripple. Except near the separatrix, where the rotational transform is large and the geometric measurements become inaccurate, the Fourier toroidal ripple matched the geometric toroidal ripple to within a few percent, and the Fourier helical ripple matched the average of the geometric helical ripples at θ = 0° and θ = 180° on the flux surface.

In the particle-following codes of this study, background plasma profiles of density, voltage, and electron temperature were assumed to be functions only of the flux surfaces. It was therefore necessary to develop a fast method of computing the toroidal flux at arbitrary points within the separatrix. This was done as follows:

First, a series of flux surface positions are found with the with the field line tracking code, and the toroidal flux enclosed by each surface is found by numerically integrating $B_{toroidal}$ over the cross-sectional area of

the surface.

Next, a three-dimensional toroidal flux grid is created. The horizontal positions where each flux surface intersects the grid (for each value of ϕ and Y in the grid) are first recorded. Then, for each grid location, the horizontal positions of the two nearest flux surfaces are found, and a linearly interpolated value of toroidal flux is assigned to the grid location.

After all the grid points are assigned their initial values, numerical smoothing of the grid is done in the

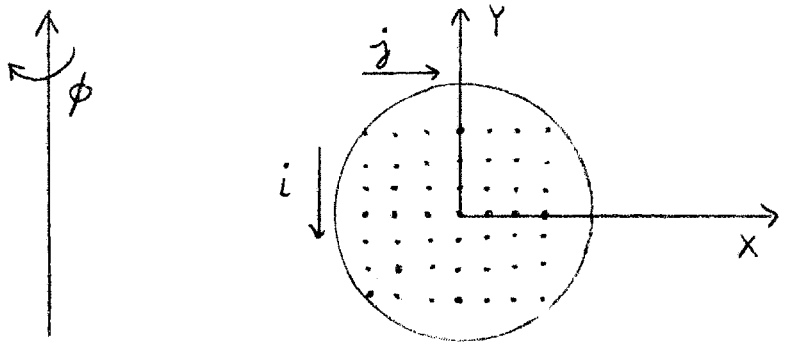

Figure D-1

vertical direction. This is done by the following formula:

$$P_{i,j\ new} = \frac{P_{i+1,j\ old} + 2P_{i,j\ old} + P_{i-1,j\ old}}{4} \qquad [D\text{-}13]$$

Finally, the three-dimensional grid is converted into a series of two-dimensional spline grids. This insures that the resulting approximation for the toroidal flux will have

continuous first and second derivatives in the radial and vertical directions. This is desirable, since the background plasma's electric field profile is a function of the gradients of the toroidal flux (see discussion in Appendix C).

In Chapter III, I showed that the torsatrons of different aspect ratios used in the α-particle confinement study were closely matched in their rotational transform per module and their poloidal flux per module. The poloidal flux functions were found through the equation:

$$\iota = \frac{d\,\psi_P}{d\,\psi_t} \qquad \text{[D-14]}$$

Since $\iota(\psi)$ and $\psi_t(\psi)$ were previously found by the line-following routines, the poloidal flux function could be calculated by numerical integration of the equation:

$$\psi_P(\psi) = \int_0^{\psi} \iota(\psi')\ \psi_T(\psi')\ d\psi' \qquad \text{[D-15]}$$

When this function was compared with a direct numerical integration of $B_{poloidal}$ over surfaces in the torsatron's horizontal midplane, a deviation of less than 2 percent was found, which was within the error of the $B_{poloidal}$ integration routine.